Induced Photon Emission from Quark Jets in Ultrarelativistic Heavy-Ion Collisions[¶]

B. G. Zakharov

Landau Institute for Theoretical Physics, Russian Academy of Sciences, Moscow, 117334 Russia
Received May 12, 2004

We study the induced photon bremsstrahlung from a fast quark produced in *AA* collisions due to multiple scattering in quark–gluon plasma. For RHIC and LHC conditions, the induced photon spectrum is sharply peaked at a photon energy close to the initial quark energy. In this region, the contribution of the induced radiation to the photon fragmentation function exceeds the ordinary vacuum radiation. Contrary to previous analyses [4–7], our results show that, at RHIC and LHC energies, the final-state interaction effects in quark–gluon plasma do not suppress the direct photon production and may even enhance it at $p_T \sim$ 5–15 GeV. © *2004 MAIK "Nauka/Interperiodica".*

PACS numbers: 25.75.Nq; 24.85.+p

1. In recent years, much attention has been attracted to the direct photon production in *AA* collisions at RHIC and LHC energies (see, for example, [1–3] and references therein). It is expected that, for sufficiently small transverse momenta ($p_T \lesssim$ 3–4 GeV), the dominating source of direct photons at RHIC and LHC is radiation from quark–gluon plasma (QGP), and at higher p_T, it is hard partonic mechanisms (Compton process, quark–antiquark annihilation, and bremsstrahlung from fast quarks (antiquarks) produced in hard reactions) [1, 2]. Nuclear effects should modify the pQCD partonic contribution to the direct photons in *AA* collisions as compared to that in *pp* interaction. For the Compton and annihilation processes, which occur at small distances, this modification, related to the initial-state interaction (ISI) effects (nuclear shadowing and Cronin effect), is relatively small. However, one can expect strong final-state interaction (FSI) effects in the QGP for the bremsstrahlung, which occurs at large distances. Investigation of the influence of the FSI on photon bremsstrahlung is of great interest from the point of view using the direct photons as a probe for the QGP at RHIC and LHC. It is especially important for LHC energies at which the bremsstrahlung component is the dominating partonic mechanism [1, 4, 5].

It was suggested [4–7] that, during RHIC and LHC, the quark energy loss in the QGP phase due to the induced gluon radiation related to the multiple scattering should strongly suppress the bremsstrahlung contribution. At LHC energies, it is equivalent to strong suppression of the total contribution of the pQCD mechanisms. In [4–7], it was assumed that the only effect of QGP on photon bremsstrahlung comes from the shift of the quark energy to a smaller value due to gluon emis-

sion before photon radiation. However, the analyses [4–7] missed two essential points. First of all, multiple scattering, which fast quarks undergo in the QGP, must enhance photon radiation due to the induced photon emission. Also, the assumption that all gluons are radiated before photon emission is not justified, since the formation lengths for gluon and photon radiation are of the same order. In this case, the gluons radiated after the photon do not suppress photon emission. For this reason, one can expect that analyses [4–7] overestimate suppression of photon bremsstrahlung. In the present paper, we address the photon bremsstrahlung at RHIC and LHC energies, accounting for the induced photon radiation and the effect of finite gluon formation length.

2. The contribution of the bremsstrahlung mechanism to the cross section of photon production can be written as [8, 9]

$$\frac{d\sigma_\gamma^{AA}(p_T)}{dy\,dp_T^2} = \int_0^1 \frac{dx}{x^2} D_{q \to \gamma}(x, p_T/x) \frac{d\sigma_q^{AA}(p_T/x)}{dy\,dp_T^2}, \quad (1)$$

where $d\sigma_q^{AA}(p_T)/dy\,dp_T^2$ is the cross section of the processes $A + A \longrightarrow q + X$ (hereafter, we suppress the argument y and mean the central rapidity region $y \approx 0$), $D_{q \to \gamma}(x, E)$ is the fragmentation function for the $q \longrightarrow \gamma q$ transition which accounts for all the FSI effects ($x = E_\gamma/E$, E_γ and E is the photon and initial quark energies, respectively). Summation over quark (antiquark) states is implicit on the right-hand side of (1). We write $D_{q \to \gamma}(x, E)$ in the form

$$D_{q \to \gamma}(x, E) = \frac{dP_{\text{vac}}(x, E)}{dx} + \frac{dP_{\text{ind}}(x, E)}{dx}. \quad (2)$$

The first term on the right-hand side of (2) is the probability distribution of the ordinary vacuum $q \longrightarrow \gamma q$

[¶] This article was submitted by the author in English.

splitting, and the second one corresponds to the induced transition due to quark multiple scattering.

An accurate evaluation of the induced photon emission from a fast quark requires treatment of photon and multiple gluon radiation on an even footing. We begin with discussion of the induced $q \longrightarrow \gamma q$ transition, ignoring gluon radiation. A qualitative method for accounting for the gluon effects will be discussed later. To evaluate the induced spectrum, we use the light-cone path integral approach [10] (see also [11–14]), which allows one to account for the Landau–Pomeranchuk–Migdal (LPM) effect [15, 16] and finite-size effects, which play an important role in the problem of interest. The induced photon spectrum for a fast quark produced at $z = 0$ can be written in a form similar to that for gluon emission given in [17] (we take the z axis along the quark momentum):

$$\frac{dP_{\mathrm{ind}}}{dx} = \int_0^\infty dz\, n(z)\frac{d\sigma_{\mathrm{eff}}^{BH}(x, z)}{dx}, \tag{3}$$

where $n(z)$ is the number density of the medium and

$$\frac{d\sigma_{\mathrm{eff}}^{BH}(x, z)}{dx} = \mathrm{Re}\int d\boldsymbol{\rho}\,\Psi^*(\boldsymbol{\rho}, x)\sigma(\rho x)\Psi_m(\boldsymbol{\rho}, x, z) \tag{4}$$

is the in-medium (z-dependent) Bethe–Heitler cross section. Here, $\sigma(\rho)$ is the dipole cross section of a quark–antiquark pair of size ρ with a particle in the medium, $\Psi(\boldsymbol{\rho}, x)$ is the light-cone wave function for the $q \longrightarrow \gamma q$ transition in vacuum, and $\Psi_m(\boldsymbol{\rho}, x, z)$ is the in-medium light-cone wave function at the longitudinal coordinate z (we omit spin indices). The no-spin flip wave functions, dominating the spectrum, read

$$\Psi(\boldsymbol{\rho}, x) = P(x)\left(\frac{\partial}{\partial \rho'_x} - is_g\frac{\partial}{\partial \rho'_y}\right)$$
$$\times \int_0^\infty d\xi \exp\left(-\frac{i\xi}{L_f^\gamma}\right)\mathcal{K}_0(\boldsymbol{\rho}, \xi|\boldsymbol{\rho}', 0)\Big|_{\boldsymbol{\rho}' = 0}, \tag{5}$$

$$\Psi_m(\boldsymbol{\rho}, x, z) = P(x)\left(\frac{\partial}{\partial \rho'_x} - is_g\frac{\partial}{\partial \rho'_y}\right)$$
$$\times \int_0^z d\xi \exp\left(-\frac{i\xi}{L_f^\gamma}\right)\mathcal{K}(\boldsymbol{\rho}, z|\boldsymbol{\rho}', z - \xi)\Big|_{\boldsymbol{\rho}' = 0}, \tag{6}$$

where $P(x) = ie_q\sqrt{\alpha_{em}/2x}\,[s_\gamma(2 - x) + 2s_q x]/2M(x)$ ($s_{q, \gamma}$ denote quark and photon helicities); $L_f^\gamma = 2E(1 - x)/m_q^2 x$ is the photon formation length; $\mathcal{K}$ is the Green's function for the two-dimensional Hamiltonian

$$\hat{H}(z) = -\frac{1}{2M(x)}\left(\frac{\partial}{\partial \boldsymbol{\rho}}\right)^2 - i\frac{n(z)\sigma(\rho x)}{2}, \tag{7}$$

with $M(x) = Ex(1 - x)$; and

$$\mathcal{K}_0(\boldsymbol{\rho}_2, z_2|\boldsymbol{\rho}_1, z_1)$$
$$= \frac{M(x)}{2\pi i(z_2 - z_1)}\exp\left[\frac{iM(x)(\boldsymbol{\rho}_2 - \boldsymbol{\rho}_1)^2}{2(z_2 - z_1)}\right] \tag{8}$$

is the Green's function for Hamiltonian (7) with $n(z) = 0$.

The dipole cross section reads

$$\sigma(\rho) = C(\rho)\rho^2, \tag{9}$$

where

$$C(\rho) = \frac{C_T C_F}{\rho^2}\int d\mathbf{q}\,\alpha_s^2(q^2)\frac{[1 - \exp(i\mathbf{q}\boldsymbol{\rho})]}{(q^2 + \mu_D^2)^2}. \tag{10}$$

Here, $C_{T, F}$ is the color Casimir for the medium constituents (quarks and gluons) and quark and μ_D is the Debye screening mass.

Effective Bethe–Heitler cross section (4) differs from that for a quark incident from infinity on an isolated scattering center due to the LPM effect and finite-size effects originating from the in-medium light-cone wave function entering (4). In the high-energy limit, when $L \ll L_f^\gamma$, where L is the thickness of the medium, the typical values of ρ become small ($\sim\sqrt{2L/Ex(1 - x)}$) and the LPM effect can be neglected. In this case, the spectrum is dominated by the $N = 1$ scattering. In this regime, the most important effect is modification of the in-medium light-cone wave function due to the finite-size effects. Let us first discuss the $N = 1$ term to illustrate qualitatively the role of the finite-size effects. Neglecting the Q^2 dependence of α_s from (4)–(10), one can obtain

$$\frac{d\sigma_{\mathrm{eff}}^{BH}(x, z)}{dx} = \frac{\pi\alpha_{em}\alpha_s C_T C_F(1 - x + x^2/2)z}{4E(1 - x)} \tag{11}$$

(hereafter, for simplicity, it is implied that $e_q = 1$). The derivation of (11) is similar to that for gluon emission given in [18]. After substitution of (11) into (3), one obtains (for $n(z) = \mathrm{const}$) the spectrum $\propto L^2$:

$$\frac{dP_{\mathrm{ind}}(x, E)}{dx} = \frac{\pi\alpha_{em}\alpha_s C_T C_F n L^2(1 - x + x^2/2)}{8E(1 - x)}. \tag{12}$$

One sees from (12) that, in the high-energy limit, contrary to the ordinary Bethe–Heitler spectrum $\propto 1/x$, the bremsstrahlung is $\propto 1/(1 - x)$. Of course, formulas (11) and (12) become invalid at $(1 - x) \ll Lm_q^2/E$ when $L_f^\gamma \ll L$ and the spectrum reduces to the ordinary Bethe–Heitler one. It is worth noting that, in the diagrammatic language, the above formula for $N = 1$ term corresponds to the set of diagrams shown in Fig. 1. We would like to emphasize that spectrum (12), similarly to the gluon spectrum of [18], cannot be obtained if one ignores the logarithmic ρ dependence of the function

$C(\rho)$ (10) at small ρ. One can see that, similarly to the gluon case, formulas (11) and (12) do not contain any large logarithmic factor $\log(\mu_D\rho_{\mathrm{eff}})$ (here, ρ_{eff} is the typical transverse scale) which one could expect there if one would neglect the ρ dependence of $C(\rho)$.

Analytical formula (12) for the $N = 1$ spectrum demonstrates that, due to the finite-size effects at large energies, when $L_f^\gamma \gtrsim L$, the induced spectrum is strongly peaked at $x \approx 1$. As will be seen below, the $N = 1$ dominates for RHIC and LHC conditions and the spectrum with the $N \geq 2$ scatterings included remains sharply peaked at x close to unity. Since the x integral on the right-hand side of (1) is also dominated by large x, one may expect that the induced photon emission is an important source of direct photons. It should be emphasized that our $1/(1 - x)$ spectrum does not mean enhancement of radiation at large x. It originates simply from the suppression of photon emission at small x due to the finite-size effects.

Now, let us discuss the influence of the induced gluon emission on the photon bremsstrahlung ignored in the above derivation. The gluon emission, i.e., processes like $q \longrightarrow \gamma g q$ and multigluon radiation, leads to quark energy loss and should reduce the radiation of hard photons. It is important that, for soft gluons, dominating the quark energy loss, the gluon formation length, $L_f^g \sim \dfrac{2Ex(1-x)}{m_q^2 x^2 + m_g^2(1-x)}$, turns out to be of the same order as that for photons. For this reason, as was already noted, photon and gluon emission should be treated on an even footing. An accurate analysis with gluon emission is a complicated task which is far beyond the scope of the present paper. We account for the influence of the induced gluon emission at a qualitative level. In line with the prescription suggested in [19] for hadron spectra, we replace in (1) the cross section of quark production by an effective cross section

$$\frac{d\sigma_{q,\,\mathrm{eff}}^{AA}(p_T)}{dy\,dp_T^2} = N_{\mathrm{bin}}\int \frac{dx}{(1-x)^2}$$
$$\times \frac{dI(x, p_T/(1-x))}{dx}\frac{d\sigma_q^{pp}(p_T/(1-x))}{dy\,dp_T^2}, \qquad (13)$$

where $dI(x, E)/dx$ is the probability distribution in the quark energy loss and N_{bin} is the number of the binary nucleon–nucleon collisions. In the p_T region of interest, the cross section of quark production in pp collisions can be parametrized as [20]

$$\frac{d\sigma_q^{pp}(p_T)}{dy\,dp_T^2} \approx \frac{A}{(p_T + p_0)^n} \qquad (14)$$

with $p_0 \approx 1.6$ GeV, $n \approx 8$ for RHIC, and $p_0 \approx 0.6$ GeV, $n \approx 5.3$ for LHC; the normalization constant A will not be important to us. For such a p_T dependence to good
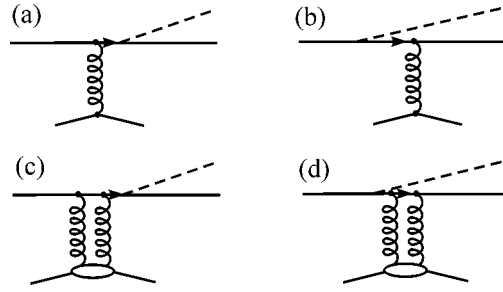
Fig. 1. The set of Feynman diagrams corresponding to the $N = 1$ scattering induced spectrum.

accuracy, one can write the effective cross section of quark production as

$$\frac{d\sigma(p_T)_{q,\,\mathrm{eff}}^{AA}}{dy\,dp_T^2}$$
$$\approx N_{\mathrm{bin}}\frac{d\sigma_q^{pp}(p_T)}{dy\,dp_T^2}\int dx(1-x)^{n(p_T)-2}\frac{dI(x, p_T)}{dx}, \qquad (15)$$

where

$$n(p_T) = -\frac{d}{d\ln p_T}\ln\frac{d\sigma_q^{pp}(p_T)}{dy\,dp_T^2} = \frac{np_T}{(p_T + p_0)}.$$

Then, the effective fragmentation function for photon radiation accounting for gluon emission can be written in the form

$$D_{q\to\gamma}^{\mathrm{eff}}(x, E) = S_g(E)\left[\frac{dP_{\mathrm{vac}}(x, E)}{dx} + \frac{dP_{\mathrm{ind}}(x, E)}{dx}\right], \qquad (16)$$

where $S_g(E)$ is the gluon suppression factor given by

$$S_g(E) \approx P_0(E) + \int_{x_{\min}}^{1} dx(1-x)^{n(E)-2}\frac{dI(x, E)}{dx}.$$

Here, we separated the probability of photon emission without gluons, P_0. In terms of the gluon spectrum, dP_g/dx, it reads

$$P_0(E) = \exp\left(-\int_{x_{\min}}^{1} dx\frac{dP_g(x, E)}{dx}\right)$$

with $x_{\min} \sim m_g/E$. In numerical calculations, we take $x_{\min} = 2m_g/E$.

We take the spectrum in the radiated energy entering (13) in the form

$$\frac{dI(x, E)}{dx} = \exp\left(-\int_{x}^{1} dy\frac{dP_g(y, E)}{dy}\right)\frac{dP_g(x, E)}{dx}. \qquad (17)$$

Formula (17) is similar to the electron energy loss spectrum derived in [21]. It works well for small energy loss $\Delta E \ll E$. For RHIC and LHC, parametrization (17) reproduces the energy loss spectrum evaluated assuming independent gluon radiation with an accuracy of ~10–40%. It is enough to make a qualitative estimate of the effect of gluon emission on the photon spectrum. An accurate calculation of the gluon suppression factor in the approximation of independent gluon emission [19, 22] does not make sense, because this approximation itself does not have any serious theoretical justification. It should be noted that the suppression of hadron spectra evaluated using energy loss spectrum (17) agrees well with that observed during RHIC. Thus, our approximation in some sense is justified by the experimental data.

Neglecting the ISI effects, the nuclear modification factor defined as

$$R_{AA}(p_T) = \frac{1}{N_{\text{bin}}} \frac{d\sigma_\gamma^{AA}(p_T)/dy dp_T^2}{d\sigma_\gamma^{pp}(p_T)/dy dp_T^2} \tag{18}$$

can be approximately written as

$$R_{AA}(p_T) \approx S_g(p_T)$$

$$\times \frac{\int\limits_0^1 dx \, x^{n(p_T)-2}[dP_{\text{vac}}(x, p_T)/dx + dP_{\text{ind}}(x, p_T)/dx]}{\int\limits_0^1 dx \, x^{n(p_T)-2} dP_{\text{vac}}(x, p_T)/dx}. \tag{19}$$

We take the vacuum distribution in the form

$$\frac{dP_{\text{vac}}(x, E)}{dx} = \frac{\alpha}{4\pi x}(4 - 4x + 2x^2) \int\limits_0^{k_{\text{max}}^2} dk^2 \frac{k^2}{(k^2 + \epsilon^2)^2}, \tag{20}$$

where $\epsilon = m_q x$ and $k_{\text{max}} \approx E \max(x, (1-x))$.

To evaluate the gluon suppression factor S_g, we use a formula for gluon spectrum similar to (3). However, we set the thickness equal to $L/2$. It seems to be a reasonable choice to account for the fact that, for $L_f^g \sim L_f^\gamma$, about half of gluons are radiated after photon emission and cannot affect the photon bremsstrahlung. Note that this reduces the suppression effect of gluon emission as compared with the analyses [4–7].

One remark is in order in connection with the above treatment of the gluon effects. Our gluon suppression factor includes only the induced gluon radiation. As far as the ordinary vacuum hard gluon radiation is concerned, we assume that, due to small formation length, the corresponding suppression factors are approximately the same for *AA* and *pp* collisions. For this reason, one may ignore the vacuum gluon radiation in evaluating the nuclear modification factor (if one uses leading-order vacuum spectrum (20)).

3. For numerical calculations, we use the one-loop running coupling constant with $\Lambda_{QCD} = 0.3$ GeV frozen at the value $\alpha_s = 0.7$. This parametrization is motivated by the desire to satisfy the relation

$$\int\limits_0^{2\,\text{GeV}} dk \frac{\alpha_s(k)}{\pi} \approx 0.36 \text{ GeV} \tag{21}$$

obtained from the analysis of the heavy quark energy loss [23]. To fix the quark and Debye screening mass, we use the results of the analysis within the quasiparticle model [24] of the lattice results. For the relevant range of temperature of the plasma $T \sim (1–3)T_c$ ($T_c \approx 170$ MeV is the temperature of the deconfinement phase transition), the analysis [24] gives for the quark and gluon quasiparticle masses $m_q \approx 0.3$ and $m_g \approx 0.4$ GeV. With the above value of m_g from the perturbative relation $\mu_D = \sqrt{2} m_g$, one obtains $\mu_D \approx 0.57$ GeV. We assume the Bjorken [25] longitudinal expansion of the QGP with $T\tau^3 = T_0\tau_0^3$. For the initial conditions, we use the values suggested in [20]: $T_0 = 446$ MeV and $\tau_0 = 0.147$ fm for RHIC and $T_0 = 897$ MeV and $\tau_0 = 0.073$ fm for LHC. For RHIC, the above conditions were obtained from the charged particle pseudorapidity density $dN/dy \approx 1260$ measured by the PHOBOS experiment [26], assuming an isentropic expansion and rapid thermolization at $\tau_0 \sim 1/3T_0$. The LHC parameters correspond to $dN/dy \approx 5625$ estimated in [27]. Note that, since the dominating ρ scale in (3) $\propto \sqrt{z}$ for $z \ll L_f^\gamma$, our results are not very sensitive to τ_0. For the upper limit of the z integration in (21), we take[1] $L = R_A \approx 6$ fm. This seems to be a reasonable value for central heavy-ion collisions since, due to the transverse expansion, the hot QCD matter should cool quickly at $\tau \gtrsim R_A$ [25].

In Figs. 2 and 3, we show the x dependence of the probability distribution of the induced $q \longrightarrow \gamma q$ transition (solid line) for several quark energies for RHIC and LHC. For comparison, the vacuum spectrum (dashed line) is also shown. One sees that, in the region of large x, which dominates the x integrals on the right-hand side of Eq. (19), the induced radiation exceeds the vacuum one (especially for the LHC case). To illustrate the influence of the LPM effect on the induced photon emission, we also show the contribution of the $N = 1$ scattering (long-dashed line). It is seen that, for $x \sim 0.6$–0.8, the LPM effect reduces the induced bremsstrahlung by a factor of ~0.8 for RHIC and ~0.5 for LHC. Note that the LPM effect and finite-size effects diminish in strength as $x \longrightarrow 1$ since L_f^γ becomes small and the spectrum should be close to the Bethe–Heitler one in this limit. To demonstrate the role of the finite kine-

---

[1] For our choice of the initial conditions, the lifetime of QGP is ~3 fm for RHIC. However, in the interval $\tau \sim 3$–6 fm, the density of the mixed phase is practically the same as that for the pure QGP phase.
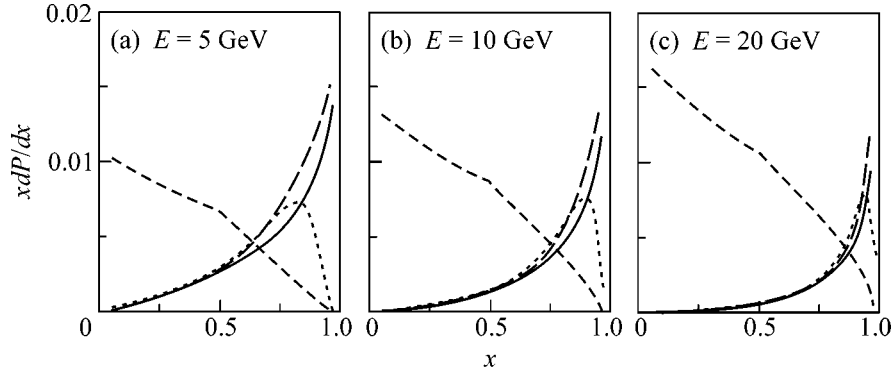
Fig. 2. The photon spectrum of the $q \longrightarrow \gamma q$ transition for RHIC conditions. The solid line shows the contribution from the induced photon emission calculated using formula (3). The dashed line shows vacuum spectrum (20). The $N = 1$ scattering contribution to the induced spectrum is shown by the long-dashed curves for infinite kinematic boundaries and by the dotted curves for finite kinematic boundaries.
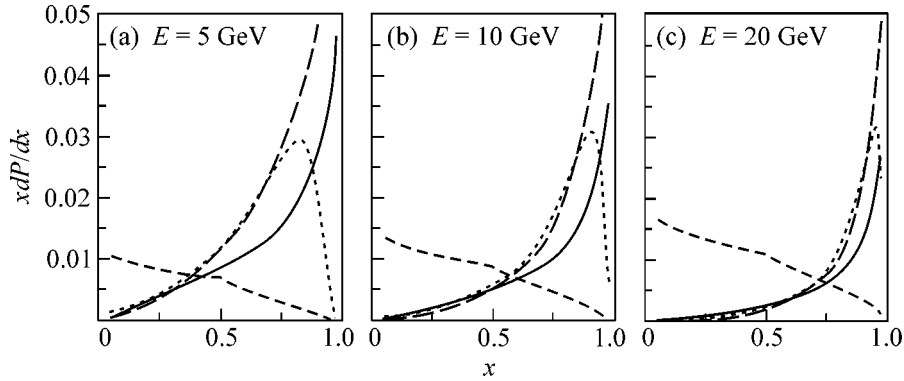

Fig. 3. The same as in Fig. 2 but for LHC.

matic limits (neglected in (3)) in Figs. 2 and 3, we also show the $N = 1$ scattering contribution evaluated using the set of diagrams shown in Fig. 1 with finite kinematic limits (dotted line). One can see that the kinematic effects become important at x close to unity. Numerical calculations show that they reduce the integral over x in the numerator in (19) by ~20–30%. However, this suppression to a good accuracy is compensated by the increase in the gluon suppression factor due to similar kinematic effects for gluon emission. For this reason, we neglect the kinematic effects in calculation of nuclear modification factor (19).

In Fig. 4, we plot results for the p_T dependence of nuclear modification factor (19). We also show the results without the gluon suppression factor (dashed line), i.e., for $S_g = 1$. One sees that, despite strong suppression due to gluon emission, we obtain $R_{AA} \gtrsim 1$ at $p_T \sim 5$–15 GeV. This means that the FSI effects can enhance the direct photon production (especially for LHC energies, where bremsstrahlung is the dominating partonic mechanism). Of course, one should bear in

mind that uncertainties in our theoretical predictions can be about 30–50%. Nevertheless, one can say that it is practically excluded that, in central AA collisions, the direct photon production is strongly suppressed due to quark energy loss, as was predicted in [4–7].
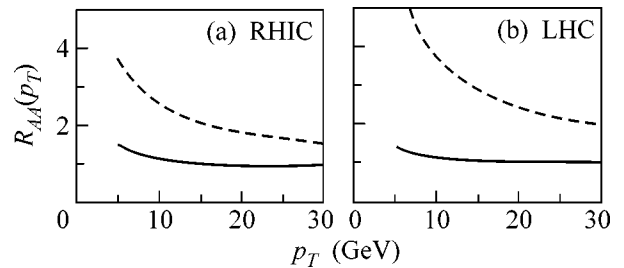

Fig. 4. The p_T dependence of nuclear modification factor (19) (solid line) for RHIC (a) and LHC (b) conditions. The dashed line shows the results without gluon suppression factor S_g on the right-hand side of (19).

REFERENCES

1. P. Aurenche, LAPTH-CONF-893-2001 (2002), *Talk Given at International Workshop on the Physics of the Quark Gluon Plasma* (Palaiseau, France, 2001); hep-ph/0201011.

2. T. Peitzmann and M. H. Thoma, Phys. Rep. **364**, 175 (2002).

3. F. Arleo, P. Aurenche, F. Bopp, *et al.*, *The CERN Yellow Report on Hard Probes in Heavy Ion Collisions at the LHC*; hep-ph/0311131.

4. A. Dumitru and N. Hammon, hep-ph/9807260 (1998).

5. J. Jalilian-Marian, K. Orginos, and I. Sarcevic, Nucl. Phys. **700**, 523 (2002).

6. J. Jalilian-Marian, K. Orginos, and I. Sarcevic, Phys. Rev. C **63**, 041901 (2001).

7. S. Jeon, J. Jalilian-Marian, and I. Sarcevic, Phys. Lett. B **562**, 45 (2003).

8. J. F. Owens, Rev. Mod. Phys. **59**, 465 (1987).

9. P. Aurenche, R. Baier, M. Fontannaz, and D. Schiff, Nucl. Phys. B **297**, 661 (1988).

10. B. G. Zakharov, JETP Lett. **63**, 952 (1996).

11. B. G. Zakharov, JETP Lett. **65**, 615 (1997).

12. B. G. Zakharov, Phys. At. Nucl. **61**, 838 (1998).

13. B. G. Zakharov, JETP Lett. **70**, 176 (1999).

14. R. Baier, D. Schiff, and B. G. Zakharov, Annu. Rev. Nucl. Part. Sci. **50**, 37 (2000).

15. L. D. Landau and I. Ya. Pomeranchuk, Dokl. Akad. Nauk SSSR **92**, 535 (1953); Dokl. Akad. Nauk SSSR **92**, 735 (1953).

16. A. B. Migdal, Phys. Rev. **103**, 1811 (1956).

17. B. G. Zakharov, in *Proceedings of the 33rd Rencontres de Moriond: QCD and High Energy Hadronic Interactions*, Ed. by J. Tran Thanh Van (Les Arcs, France, 1998), p. 533; hep-ph/9807396.

18. B. G. Zakharov, JETP Lett. **73**, 49 (2001).

19. R. Baier, Yu. L. Dokshitzer, A. H. Mueller, and D. Schiff, J. High Energy Phys. **0109**, 033 (2001); hep-ph/0106347 (2001).

20. R. J. Fries, B. Müller, and D. K. Srivastava, nucl-th/0208001 (2003).

21. B. G. Zakharov, Phys. At. Nucl. **62**, 1008 (1999); JETP Lett. **78**, 759 (2003).

22. M. Gyulassy, P. Levai, and I. Vitev, Phys. Lett. B **538**, 282 (2002).

23. Yu. L. Dokshitzer, V. A. Khoze, and S. I. Troyan, Phys. Rev. D **53**, 89 (1996).

24. P. Levai and U. Heinz, Phys. Rev. C **57**, 1879 (1998).

25. J. D. Bjorken, Phys. Rev. D **27**, 140 (1983).

26. B. B. Back *et al.* (PHOBOS Collab.), Phys. Rev. C **65**, 061901 (2002).

27. J. Kapusta, L. D. McLerran, and D. K. Srivastava, Phys. Lett. B **283**, 145 (1992).

Laser Pulse Amplification upon Raman Backscattering in Plasma Produced in Dielectric Capillaries

A. A. Balakin, D. V. Kartashov*, A. M. Kiselev, S. A. Skobelev, A. N. Stepanov, and G. M. Fraĭman

Institute of Applied Physics, Russian Academy of Sciences, ul. Ul'yanova 46, Nizhni Novgorod, 603950 Russia
*e-mail: dekart@ufp.appl.sci-nnov.ru
Received May 5, 2004

Femtosecond-pulse amplification upon stimulated Raman scattering is experimentally demonstrated for the case of a counter-propagating femtosecond laser pulse and a frequency-modulated broadband pump pulse with the same carrier frequency in a dielectric capillary filled with gas plasma. A value of $\sim 10^3$ obtained for the spectral intensity amplification and $\sim 10^2$ for the output energy are the highest ever achieved for these quantities to date. Numerical simulation demonstrates good agreement with the experimental results. Based on the experimental data and the results of theoretical calculations, we propose a hydrodynamic mechanism for plasma-wave breaking as the mechanism playing an important role in the amplification restriction in the scheme considered. © 2004 MAIK "Nauka/Interperiodica".

PACS numbers: 52.38.Bv; 42.65.Re

1. The development of femtosecond lasers and an amplification technique for frequency-modulated laser pulses [1] has culminated in the fabrication of petawatt laser facilities of ultrahigh electromagnetic-field intensity. Further increase in laser power faces considerable technical problems. These are primarily associated with the stability of optical elements in ultrahigh-power laser systems. This necessitates a considerable increase in the geometrical sizes of used optics, which is a very complex technical problem. For this reason, to achieve hundreds of terawatts and higher, alternative amplification schemes have been proposed for frequency-modulated pulses.

One such approach, whose experimental implementation is described in this work, is based on the parametric amplification of femtosecond laser pulses upon Raman backscattering in plasma [2]. This approach is attractive because it uses plasma as a nonlinear medium that has no limitations on the optical breakdown. As is known [2], the duration of a short amplified pulse increases appreciably at the linear stage of Raman backscattering; hence, the linear stage is unsuitable for the amplification of short laser pulses. Because of this, to amplify femtosecond laser pulses in Raman backscattering, it is necessary to attain its nonlinear stage, where the amplified pulse is compressed practically to the duration of the seed femtosecond pulse and which, according to the calculations, efficiently uses pumping. The first experiments [3] and theoretical estimates [4, 5] showed that the plasma length and spatial homogeneity, the pump-frequency modulation and its magnitude, and the plasma-wave breaking at low plasma concentrations play the key role in the realization of the nonlinear stage [2].

In this work, we present the results of experimental and theoretical study of the femtosecond radiation amplification upon Raman backscattering in plasma formed in gas-filled dielectric waveguides (capillaries). The use of capillaries for producing plasma and channeling the interacting waves allows the interaction length to be greatly increased as compared to the radiation focusing in free space, where diffraction restricts the interaction region to the Rayleigh length. Another fundamental feature of our scheme is that the same terawatt femtosecond laser radiation is used as both pumping and amplified signal. In this case, the spectra of the pump and amplified pulses are identical, and the matching conditions for the plasma-oscillation excitation can, in principle, be fulfilled only at low plasma concentration, so that the frequency of plasma oscillations is smaller than or comparable to the laser radiation width.

2. Femtosecond terawatt Ti:Sa laser system [6] allowing pulse generation with an energy up to 100 mJ, wavelength $\lambda = 0.8$ μm, a pulse duration of 80 fs, and a repetition rate of 10 Hz was used in the experiment. The experimental scheme is shown in Fig. 1. A frequency-modulated laser pulse with a duration of 160 ps at the output of the last amplification stage of the laser system was split into two pulses, one of which was used as a pump pulse (solid line in Fig. 1). In our experiment, the maximal pump energy was 18 mJ. After compression to a duration of 80 fs in a compressor, the second portion of the amplified laser radiation was used for plasma formation (dash-and-dot line) and the formation of the amplified laser pulse (dotted line). The ionizing and amplified pulses had orthogonal polarizations and were introduced into a capillary on the side opposite to the
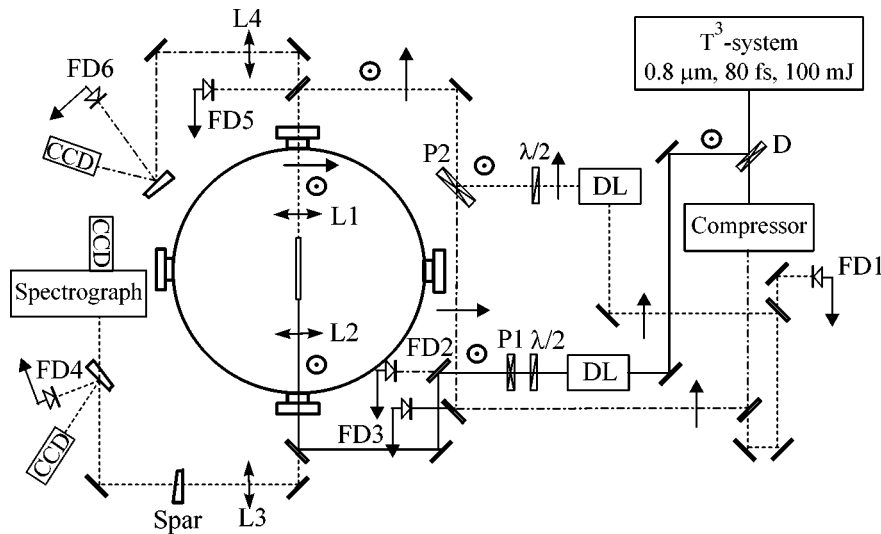
Fig. 1. Scheme of the experiment. Solid line is for the pump channel; dashes are for the amplified pulse channel; dash-and-dot line is the ionizing pulse channel; DL are the delay lines; P1,2 are polarizers; $\lambda/2$ are the half-wave plates; and D is a divider. The arrows denote the horizontal radiation polarization, and the circles denote the vertical polarization.

pump pulse. The energy of the ionizing pulse was 1 mJ, and the maximal energy of the amplified pulse was 1 μJ. The time coincidence of the amplified and pump pulses in the capillary was achieved using delay lines and controlled by the noncollinear second harmonic generation in a LiIO$_3$ crystal. The energies of the pump and amplified pulses were controlled using polarization attenuators. The pulse energies at the capillary input and output were controlled using calibrated FD1–FD6 photodiodes. A glass capillary with an inner diameter of 30 μm and length $L = 1.5$ cm placed on a 5-coordinate translational stage in a vacuum chamber was used in the experiment.

Lenses L1 and L2 were chosen so as to provide the optimal matching of input beam with the capillary fundamental mode $\tilde{E}H_{11}$. The maximal pump and ionizing pulse intensities were 5×10^{13} W/cm^2 and 5×10^{15} W/cm^2, respectively. Lenses L3 and L4 carried images of the capillary output ends to a spectrograph with a CCD chamber placed at its output for recording the amplified-pulse spectrum and to CCD chambers for monitoring the spatial distribution in the beams of all three signals. For the polarization decoupling of the ionizing and amplified pulses, an Iceland spar wedge was used.

A delay of 3 ns between the ionizing pulse and the amplified and pump pulses was used to level off the plasma concentration across the capillary. The Ar pressure used in the experiment varied from 0.3 to 30 torr. The measured efficiency of pulse passage through the capillary was 25%. This value is determined by the excitation efficiency of the capillary mode (estimated at 90%) and by the mode loss upon passing through the capillary (70%). The efficiency of radiation passage through the capillary was the same for a vacuum capil-

lary and a capillary with plasma. This is in accordance with the results obtained in [7, 8] and is evidence of a single-mode radiation-propagation regime in capillary. The experimental results are presented below. For a rather high pump energy, peaks appeared in the spectrum of the amplified pulse (Fig. 2). The peak widths were much smaller than the width of the initial spectrum, and the spectral intensity increased more than by a factor of 10^3 for the maximal amplification. In some pulses, the spectrum of the amplified signal had a more complicated structure and consisted of several peaks, one of which had the maximal intensity, and a number of weaker peaks detuned from the maximum at a frequency on the order of the plasma frequency. The energy amplification ratio (capillary output-to-input energy ratio for the amplified pulse) as a function of the pump energy (Fig. 3) was obtained by processing the
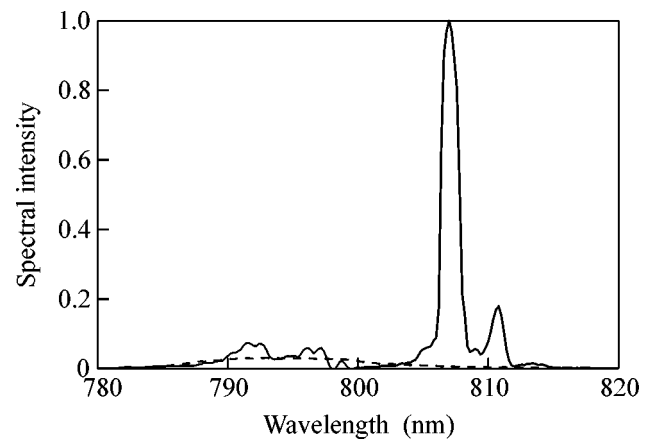

Fig. 2. Spectral intensity of the amplified signal. Dashes show the seed-pulse spectrum.
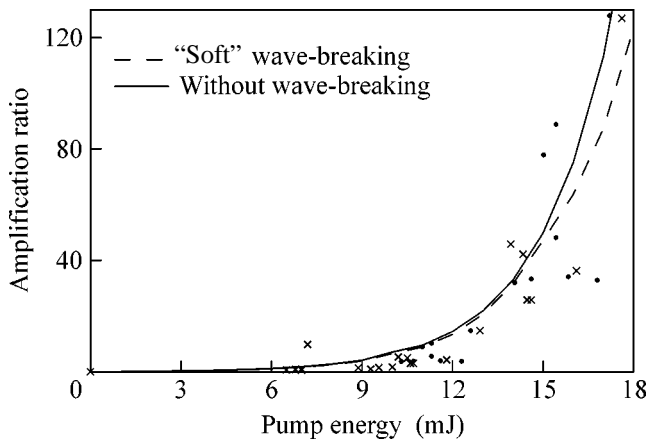
Fig. 3. Amplification ratio as a function of the pump energy. The crosses and dots are the experimental values for two delay times between the pump and amplified pulses; lines are for the theoretical calculations.

Fig. 4. Amplification ratio as a function of the input energy of the amplified pulse. Circles are the experimental values and lines are the theoretical calculations for different wave-breaking models.

amplified pulse spectra. These data correspond to an Ar pressure of 0.3 torr and an energy of ≈ 0.1 μJ (corresponding to the intensity $\approx 10^{12}$ W/cm^2) for the amplified pulse at the capillary input. The results are shown for two (close to optimal) delay times between the amplified and pump pulses. One can see from the figure that the amplification is experimentally detected for the pump energy >6 mJ, then it rapidly increases and reaches a maximal value of 130 for the maximal pumping. The pulse amplification was observed in the pressure range 0.3–1 torr. At higher pressures, the amplification effect was not observed. For an understanding of the role of various processes contributing to the Raman backscattering amplification in plasma, of interest is the amplification ratio as a function of input energy of the amplified pulse (Fig. 4). The corresponding dependence was obtained for the pump energy close to the maximal but without optimizing the time delay between the amplified and pump pulses. The descending character of the obtained curve is evidence of the important role of the nonlinear processes in our experiments (at the linear amplification stage, the amplification ratio should not depend on the energy of the amplified pulse).

3. The theory predicts that, in the case of monochromatic spectra of the amplified and pump pulses, the amplified signal should exponentially increase with the spatial increment $\gamma = 2 \times 10^{-20} \lambda \sqrt{I} \sqrt{\omega_0 \omega_p}$ (in cm^{-1}) at the linear stage of Raman backscattering in homogeneous plasma [2]. Here, λ is the pump wavelength in μm; I is the pump intensity in W/cm^2; and ω_0 and ω_p are the central pump frequency and the plasma frequency, respectively. For a maximal pump intensity of 5×10^{13} W/cm^2 and a typical plasma concentration of $(1.4–4) \times 10^{16}$ cm^{-3}, this gives the amplification by $\exp(\gamma L)$ times along the capillary length, with $\gamma L = 20$. At first sight, this should result in a rapid enhancement
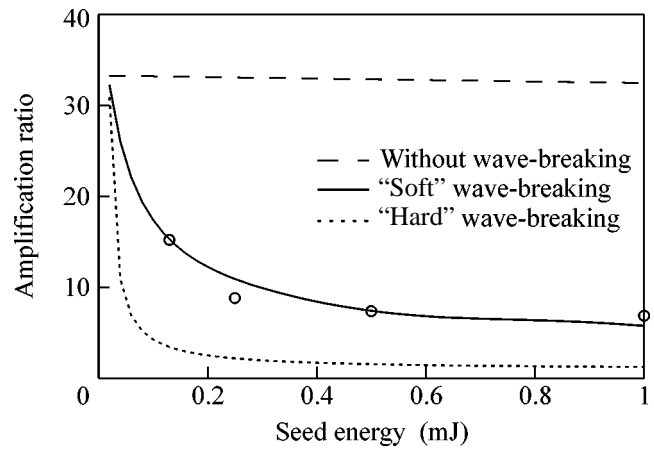
of the amplified signal and attainment of the nonlinear amplification stage.

However, the actual experimental conditions were different from the idealized scheme. The pump-frequency modulation had a considerable effect on the amplification. The dependence of the difference between the instantaneous pump frequency and the central frequency of the amplified pulse is shown in Fig. 5 by the solid line. This dependence is constructed for the case where the pulses met in the middle of capillary. After changing the delay between the pump and amplified pulses, the line shifts in parallel to itself either up or down. Due to the radiation decay in the propagation along the capillary, plasma produced by the ionizing pulse was inhomogeneous along the capil-
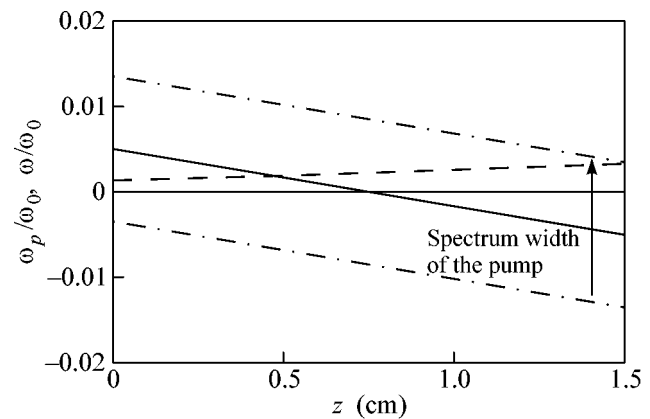

Fig. 5. The plasma-frequency distribution (dashed line) and the distribution of the difference between the instantaneous pump frequency and the central frequency of the amplified signal (solid line) along the capillary. Plasma frequency is calculated for a plasma concentration of 4×10^{16} cm^{-3}, and the pump spectrum width corresponds to the half-maximum of spectral intensity.

lary axis. To take into account this effect, the balance equations were numerically solved for the concentrations of ions with different charges, analogous to [7]. The calculated plasma frequency distribution along the capillary axis is shown by the dashed line in Fig. 5. The difference between this line and the solid line is equal to the detuning of three-wave-mixing resonance. The parameter $q = \dfrac{1}{\gamma^2 c}\dfrac{d(\omega - \omega_p)}{dz} \approx 1$ characterizing the influence of frequency modulation on the amplification process proves to be quite large and leads to an appreciable decrease (by several orders of magnitude) in the amplification ratio.

The aforementioned coincidence of the spectra of amplified and pump pulses is a fundamental feature of our experiment. To satisfy the matching conditions, the plasma frequency should fall within the spectrum width of these pulses (Fig. 5). The ratio of the pump spectrum width to the plasma frequency in a pressure range of 0.3–1 torr, where the amplification was experimentally obtained, was equal to three to four.

The nonlinear plasma-wave breaking is the most probable cause for the experimentally observed decrease in the amplification ratio with increasing seed energy. Estimations show that, even at the stage of excitation by the seed pulse, the plasma-wave potential is only slightly lower than the critical amplitude [9] $f_{wb} = \dfrac{mc^2}{2e}\left(\dfrac{\omega_p}{\omega}\right)^2$, where c is the wave-breaking velocity of light, and becomes of the order of critical amplitude in the course of amplification. For this reason, the distinctions between the aforementioned features of our experiment and the standard Raman-backscattering observation conditions necessitate certain modifications of the well-known theoretical model [4]. First, the question arises of the plasma-wave-breaking effect on the Raman amplification and its description within the framework of hydrodynamic approximation. Another important point is that the spectrum width of the interacting waves is much greater than the plasma frequency, as a result of which plasma wave should be considered using the complete (i.e., not reduced) equation.

On this basis, the equations for Raman backscattering take the form

$$\partial_t a + \partial_z a - i\nabla_\perp^2 a = bf, \tag{1}$$

$$\partial_t b - \partial_z b - i\nabla_\perp^2 b = -af^*, \tag{2}$$

$$\partial_{tt} f + \varpi_p^2 f = -2i\varpi_p \hat{B}(f)[ab^*]. \tag{3}$$

Here, a and b are the complex amplitudes of the pump-wave and amplified-pulse vector potentials normalized to mc^2/e, respectively, and f is the amplitude of the plasma-wave potential normalized to $(mc^2/2e)\sqrt{\omega_p/2\omega_0}$. Time t is normalized to $t_0 =$

$\sqrt{2/\omega_0\omega_p}$, the longitudinal coordinate z is normalized to ct_0, $\varpi_p = \omega_p t_0$ is the normalized plasma frequency, and $\hat{B}(f)$ is the breaking operator.

The form of operator $\hat{B}(f)$ is the most complicated problem in the hydrodynamic description of Raman backscattering. The reason is that the plasma-wave breaking is an essentially kinetic process and cannot be described in detail within the hydrodynamic approach. Nevertheless, the breaking effect on the Raman amplification can be qualitatively taken into account through the introduction of the wave-breaking operator $\hat{B}(f)$ on the following grounds. At small plasma-wave amplitudes $f < f_{wb}$, the breaking effect is negligible; i.e., $\hat{B}(f < f_{wb})[R] \approx R$. At the same time, this operator should preclude an increase in the plasma wave higher than the critical value f_{wb}; i.e., $\mathrm{Re}\,\hat{B}(f \geq f_{wb})[R] \leq 0$. It also seems reasonable that the plasma-wave breaking "impairs" plasma in such a way that plasma wave cannot be repeatedly excited during the Raman backscattering time (of the order of a few picoseconds), provided that the breaking already occurred earlier at this point.

One can propose two extreme scenarios for the behavior of plasma wave after breaking. In a "soft" scenario, the operator $\hat{B}(f)$ only restricts the wave growth and does not destroy the plasma wave. As a result, the pulse can continue to be amplified at a distance from the breaking front. In the "hard" scenario, the breaking completely destroys the plasma wave and precludes its further excitation at this point. With this scenario, the pulse amplification is possible only within a narrow leading front ahead of the plasma-wave breaking point. As a consequence, the energies in this case are low (Fig. 4). The numerical calculations presented in this work were based on the more realistic soft scenario, because its results most closely correspond to the experiments. The PIC results [9] also provide some indirect evidence in favor of the soft scenario. The detailed discussion of the possible scenarios and the comparison of the corresponding results we address to a subsequent publication. We only note the good agreement of the numerical results presented in Figs. 3 and 4 for the soft breaking scenario with the experimental results. The dashed line in Fig. 4 shows the calculated dependence of the amplification ratio on the seed energy without allowance for the wave breaking ($\hat{B}(f) = 1$), the solid line takes the breaking into account in the soft regime, and the dotted line corresponds to the hard breaking regime.

4. In summary, we note that the amplification ratios obtained in this work for laser pulses in plasma Raman backscattering are the highest ever achieved in the works published to date.[1] A high level of pump-fre-

---

[1] When preparing this article, the amplification of ≈400 achieved by the group obtained hitherto the highest amplification ratio of 95 [10] came to our knowledge.

quency modulation and, according to our theoretical positions and calculations, the plasma-wave breaking are the main factors that restricted the amplification in our experiment and did not allow the use of the capillary waveguide advantages and the achievement of the nonlinear amplification regime with a high pump-energy gain. The negative effect of these factors can be appreciably reduced by a decrease in the pump-frequency modulation level and the introduction of a detuning between the seed and pump carrier frequencies, as a result of which the plasma concentration and, correspondingly, the plasma-wave-breaking threshold can be increased.

REFERENCES

1. G. A. Mourou, C. P. J. Barty, and M. D. Perry, Phys. Today **51**, 22 (1998).
2. V. M. Malkin, G. Shvets, and N. J. Fisch, Phys. Rev. Lett. **82**, 4448 (1999).
3. Y. Ping, I. Geltner, N. J. Fisch, *et al.*, Phys. Rev. E **62**, R4532 (2000); Y. Ping, I. Geltner, A. Morozov, *et al.*, Phys. Rev. E **66**, 046401 (2002); Y. Ping, I. Geltner, and S. Suckewer, Phys. Rev. E **67**, 016401 (2003).
4. V. M. Malkin, G. Shvets, and N. J. Fisch, Phys. Plasmas **7**, 2232 (2000).
5. I. Y. Dodin, G. M. Fraiman, V. M. Malkin, and N. J. Fisch, Zh. Éksp. Teor. Fiz. **122**, 723 (2002) [JETP **95**, 625 (2002)].
6. A. A. Babin, A. M. Kiselev, A. M. Sergeev, and A. N. Stepanov, Kvantovaya Élektron. (Moscow) **31**, 623 (2001).
7. A. A. Babin, D. V. Kartashov, A. M. Kiselev, *et al.*, Pis'ma Zh. Éksp. Teor. Fiz. **76**, 645 (2002) [JETP Lett. **76**, 548 (2002)]; Appl. Phys. B **75**, 509 (2002).
8. F. Dorchies, J. R. Marques, B. Cros, *et al.*, Phys. Rev. Lett. **82**, 4655 (1999).
9. D. S. Clark and N. J. Fisch, Phys. Plasmas **10**, 3363 (2003).
10. Y. Ping, W. Cheng, S. Suckewer, *et al.*, Phys. Rev. Lett. (in press).

Translated by V. Sakun

Measurement of the Morphological Forms of Polarization Singularities and Their Statistical Weights in Optical Vector Fields

V. G. Denisenko, R. I. Egorov, and M. S. Soskin*
Institute of Physics, National Academy of Sciences of Ukraine, pr. Nauki 144, Kiev, 03028 Ukraine
*e-mail: marats@vortex.kiev.ua

Using the developed optical method, elliptically polarized fields were taken as examples for the experimental measurement of all three possible morphological forms in the vicinities of the circular polarization points and of their statistical weights in generic speckle fields. © *2004 MAIK "Nauka/Interperiodica".*

PACS numbers: 42.25.Ja; 42.30.Ms

At present, the study of the structures of nonuniformly polarized optical fields is of considerable interest for polarization optics. The polarization nonuniformity of a particular optical field can serve, e.g., as a criterion for the revelation and description of the structural features of the medium responsible for the nonuniformity.

In the general case, the optical field becomes elliptically polarized after passing through a depolarizing medium. However, due to the medium inhomogeneity in the beam cross section, the points with circular (C points) and linear polarizations appear, in addition to the elliptic polarization. The polarization state at any field point can be fully described by the ellipse azimuth and the ellipticity (with allowance for the sense of rotation). In such a description, the C points are azimuthally degenerate (singular [1]).

The detailed theoretical analysis of an optical field containing a system of C points was carried out by Freund *et al.* in [2], and the conclusions of that work were confirmed in [1, 3].

The subject of this work was to study experimentally the influence of C points on the field polarization structure in the near vicinity of these points. This problem was studied theoretically by Dennis in [4].

The simplest visual form of the polarization azimuth distribution in the beam cross section is given by a surface in the Cartesian coordinates. The coordinates X and Y correspond to the point position in the beam cross section, and Z is the azimuthal angle. In this representation, the vicinity of the C point is a spiral turn with the ascending direction determining the sign of the C-point topological index.

The point topological index (I_c) is equal to the rotation angle (in units of 2π) of the azimuth of the major axis of the surrounding ellipses upon the com-

plete round trip this point. For the "ordinary" field points, $I_c = 0$, and $I_c(C^+) = +1/2$ and $I_c(C^-) = -1/2$ only for the C points for which the polarization azimuth changes by π upon round trip the singularity in the counterclockwise or clockwise direction, respectively.

Dennis in his work presented the analytic expressions for the form of singularity vicinity, from which it follows that the azimuth changes irregularly upon round trip the singular point (the dependence of the azimuth on the polar angle has extremes). Only three tendencies are possible for its behavior [4, 5]. They determine the field morphology around the C points: star (S), lemon (L), and monstar (M), with the indices

$$I_c(C^-, \text{star}) = -1/2,$$

$$I_c(C^+, \text{lemon}) = I_c(C^+, \text{monstar}) = 1/2.$$

These morphological forms differ from each other by the number and position of the straight lines where the azimuthal angle φ is equal to the polar angle θ around the C point (see columns 1 and 2 in the table):

$$\theta = \varphi \pm n\pi, \qquad (1)$$

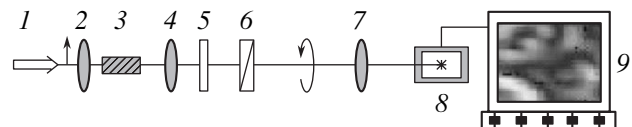where $n = 0, 1, \ldots$. The tangents to the solid contours (column 2 in the table) determine the orientation of the

Fig. 1. Scheme of a singular Stokes polarimeter: (*1*) He–Ne laser ($\lambda = 633$ nm); (*2*) lens focusing the beam onto the medium under study (*3*); (*4*) collimating lenses; (*5*) phase (λ/4) plate; (*6*) polarizer; (*7*) scaling lens; (*8*) CCD chamber; and (*9*) PC.

Morphological forms	Theoretical model	Photonic-crystal fiber	Two-sided scattering polymer film	Cut of human skin
1	2	3	4	5
S $I_C = -1/2$				
L $I_C = 1/2$				
M $I_C = 1/2$				

Morphological forms in the vicinity of the C points. Column 2 presents the modeling results [14–16] (solid (dotted) lines correspond to the morphological forms for the major (minor) axes of the polarization ellipses). Columns 3–5, present the measurement results processed for three morphological forms obtained for a photonic-crystal fiber, scattering polymer film, and a cut of human skin. Panels S2–S5 show the experimentally obtained angular scatter for the S form ("Stars" for different C points are brought into coincidence on one of the straight lines). In panels L2–L5 the obtained L forms are shown (the solid black line is the axis for "Lemon"). The dashes show the orientation of the major axis of polarization ellipses in the vicinity of the C point. In panels M2–M5 the angular scatter is shown for the M form (different "Monstars" are brought into coincidence on the central line). If the three lines merge into a single line, the M ⟶ L transition is possible.

major axis of polarization ellipse at the corresponding field point.

The statistical weights α of these forms depend on the properties of real systems. For the nonuniformly polarized random fields with the Gaussian phase statistics, $\alpha_{star} = 0.5$, $\alpha_{lemon} = 0.45$, and $\alpha_{monstar} = 0.045$, the corresponding expressions were obtained in [6–8].

The same morphological forms occur in fields of any type around the isotropic points [6, 7, 9–11].

To generate the developed vector speckle fields, three types of media were used [1, 2]. A speckle field with the developed substructure was produced after the scattering from a two-sided dulled polymer film ($d = 200$ μm) with the independent roughness ensembles or from the optical inhomogeneities of a thin ($d = 20$ μm) cut of human skin. A smooth speckle field was formed at the output of a multimode photonic-crystal fiber with the core $d = 50$ μm as a result of the interference of the frequency-degenerate ensemble of the polarized transverse modes.

The far zone of the speckle field was measured on a Stokes polarimeter (Fig. 1). The parameters and position of collimating lens 7 allowed obtaining 20–35 C points at the receiving screen of the CCD chamber (640×539 pixels with a spatial step of 8 μm). Com-
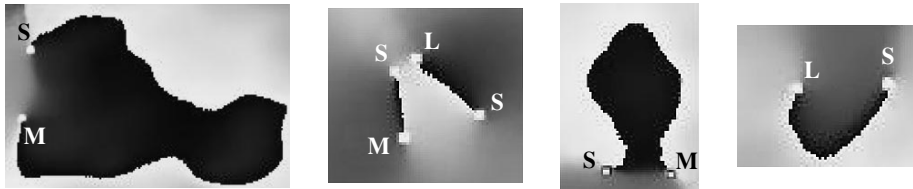
Fig. 2. Typical fragments of the measured vector speckle fields for the closely spaced pairs of C points of the S–M and S–L types. The gray shading codes the polarization azimuth in the range 0–π.

puter processing of the measurement results using our program allowed us to determine the azimuth distribution pattern with an accuracy up to 42′ for each pixel. For all three media, ten measurement runs were conducted.

The shape of each C point in the visual field was determined in two steps on the matrix of azimuths of the surrounding ellipses at a distance of 5–20 pixels. First, the pixel coordinates satisfying Eq. (1) were found at a circular contour of a certain radius. Then, this radius was varied within certain limits. The resulting straight lines were found as a set of these intersection points.

In accordance with the theory, all C^- point had S form. The numbers of the C^- and C^+ points were approximately the same, in accordance with the pair singularity-generation law [12, 13]. The measured azimuthal structures are presented in a compact form in the table (panels S3-S5, L3-L5, and M3-M5). The qualitative correspondence between the measured and predicted forms is clearly seen. All C^- points had the S form for $\alpha_{C,star} = 0.5$ because of the field topological index conservation law. A considerable scatter of the angles between the "form-generating" straight lines is caused by the fact that the real-field statistics differs from the Gaussian statistics that is assumed in the existing theories. The found morphological form of L agrees with the modeling results obtained for the random orientation of the zero azimuthal equiline [2, 14]. According to the theory, the statistical weight of the M form is low (0.05), it is unstable, and transforms into the L form in the course of further evolution through the mutual approach of the side lines and their merging [14]. Indeed, the M form was observed rather rarely only for the closely spaced pairs of C points (Fig. 2).

$\alpha_{C,monstar}$ was equal to ~0.2 for fiber, 0.05–0.07 for the cut of human skin, and about 0.13 for film. The fact that the ratios M : S : L are quantitatively different from those calculated for the fields with Gaussian statistics [2, 14] indicates that the latter is slightly broken.

It is worth noting that the form-generating lines are straight only in the vicinity of the C point considered. At larger distances, they are bent due to the influence of other topological field elements.

Note in conclusion that the random vector speckle fields generated by the polarizationally inhomogeneous media have been taken as example in this work to iden-

tify experimentally all three morphologically allowed S, L, and M distribution forms of polarization ellipses around the isotropic points with circular polarization, and their statistical weights are measured. The form-generating straight lines are asymmetric and show appreciable angular scatter for the S and M structures, as compared to their canonical forms. The statistical weight of the most unstable and rare M form varies from the theoretical value 0.05 to 0.2 for different media. The results obtained are one more demonstration of the universality of the topological and morphological laws.

REFERENCES

1. M. Soskin, V. Denisenko, and R. Egorov, J. Opt. A: Pure Appl. Opt. **6**, S281 (2004).
2. I. Freund, M. Soskin, and A. Mokhun, Opt. Commun. **208**, 223 (2002).
3. M. Soskin, V. Denisenko, and I. Freund, Opt. Lett. **28**, 1475 (2003).
4. M. Dennis, Opt. Commun. **213**, 201 (2002).
5. M. V. Berry and J. H. Hannay, J. Phys. A: Math. Gen. **10**, 1809 (1977).
6. A. S. Thorndike, C. R. Cooley, and J. F. Nye, J. Phys. A: Math. Gen. **11**, 1455 (1978).
7. J. F. Nye, J. Glaciol. **29**, 70 (1983).
8. S. S. Rozhkov, Usp. Fiz. Nauk **149**, 259 (1986) [Sov. Phys. Usp. **29**, 530 (1986)].
9. J. F. Nye, J. Glaciol. **32**, 363 (1986).
10. H. J. Hutchinson, J. F. Nye, and P. S. Salmon, J. Struct. Mech. **11**, 371 (1983).
11. E. Umezaki and S. Terauchi, Opt. Lasers Eng. **38**, 71 (2002).
12. J. F. Nye and M. V. Berry, Proc. R. Soc. London, Ser. A **336**, 90 (1974).
13. M. S. Soskin and M. V. Vasnetsov, Prog. Opt. **42**, 219 (2001).
14. J. Nye, *Natural Focusing and the Fine Structure of Light* (IOP, Bristol, 1999).
15. J. V. Hajnal, Proc. R. Soc. London, Ser. A **414**, 447 (1987).
16. M. V. Berry, Proc. SPIE **4403**, 4 (2001).

Translated by V. Sakun

New Universality Type in Chaotic Synchronization of Dynamic Systems

A. A. Koronovskii, O. I. Moskalenko, and A. E. Hramov*

Saratov State University, ul. Universitetskaya 42, Saratov, 410012 Russia
*e-mail: aeh@cas.ssu.runnet.ru
Received April 5, 2004

A quite universal mechanism of establishing chaotic synchronization regime in coupled dynamic systems is found. It is shown that the synchronous regime arises due to the phase coupling between the Fourier-spectrum components of the interacting chaotic oscillators. © 2004 MAIK "Nauka/Interperiodica".

PACS numbers: 05.45.Xt

Chaotic synchronization is one of the fundamental phenomena that have been actively studied in recent years [1] because of their theoretical and applied importance (e.g., in data transmission using the determinate chaotic oscillations [2], in biological systems [3], etc.). One can distinguish several different types of chaotic synchronization, such as generalized [4], phase [1], lag [5], and complete synchronization [6]. It was shown in [7] that the phase, lag, and complete synchronizations are closely related processes and, in essence, belong to the same type of synchronous vibrations of coupled chaotic oscillators. The character of the synchronous regime (phase, lag, or complete synchronization) is determined by the number of synchronized time scales introduced by the continuous wavelet transform [8]. Since the time scale s is associated with frequency, the synchronization of chaotic oscillations is associated with the phase coupling between the frequency components ω of the corresponding Fourier spectra $S(\omega)$.

The purpose of this work is to study the mechanism of establishing coupling between the frequency components of the coupled dynamic systems. To begin with, we consider how the close frequency components of two coupled oscillators behave when the coupling between them is strengthened. As a model of oscillators with a nearly single-frequency behavior, we choose two coupled Van-der-Pol oscillators with slightly different parameters:

$$\ddot{x}_{1,2} - (\varepsilon - x_{1,2}^2)\dot{x}_{1,2} + \Omega_{1,2}^2 x_{1,2} = \pm K(x_{2,1} - x_{1,2}), \quad (1)$$

where $\Omega_{1,2} = \Omega \pm \Delta$ are slightly different partial frequencies; $x_{1,2}$ are the variables describing the behavior of the first and second self-excited oscillators, respectively; and K is the coupling parameter. The nonlinearity parameter $\varepsilon = 0.1$ was chosen to be small to provide a nearly single-frequency character of the self-excited oscillators; the asymmetric coupling provides the establishment of synchronous regime in system (1),

analogous to the lag-synchronization regime in chaotic systems, where the oscillators have the same frequency with a small phase difference that decreases with increasing coupling parameter.

Applying the method of slowly varying amplitudes, we seek the solution to Eq. (1) in the form $x_{1,2} = A_{1,2}e^{i\omega t} + A_{1,2}^* e^{-i\omega t}$ with $\dot{A}_{1,2} e^{i\omega t} + \dot{A}_{1,2}^* e^{-i\omega t} = 0$, where * stands for complex conjugation and ω is the oscillation frequency in system (1). After averaging over the rapidly varying variables, we obtain the equations for the complex amplitudes:

$$\dot{A}_{1,2} = \frac{1}{2}(\varepsilon - |A|^2)A$$
$$+ i\frac{1}{2\omega}[(\Omega_{1,2}^2 - \omega^2)A_{1,2} \mp K(A_{2,1} - A_{1,2})]. \quad (2)$$

By choosing the complex amplitude in the form

$$A_{1,2} = r_{1,2}e^{\varphi_{1,2}}, \quad (3)$$

we arrive at the equations for the amplitudes $r_{1,2}$ and phases $\varphi_{1,2}$ of the coupled oscillators:

$$\dot{r}_{1,2} = \frac{1}{2}(\varepsilon - |r_{1,2}|^2)r_{1,2} \pm \frac{Kr_{2,1}}{2\omega}\sin(\varphi_{1,2} - \varphi_{2,1}),$$
$$\dot{\varphi}_{1,2} = \frac{\Omega_{1,2}^2 - \omega^2 \pm K}{2\omega} \pm \frac{Kr_{2,1}}{2\omega r_{1,2}}\cos(\varphi_{1,2} - \varphi_{2,1}). \quad (4)$$

The condition for the synchronous vibrations of oscillators (1) at frequency ω is that the derivatives $\dot{r}_{1,2}$ and $\dot{\varphi}_{1,2}$ be zero. Assuming that the phase difference $\Delta\varphi = \varphi_2 - \varphi_1$ is small and retaining only the terms first order

in $\Delta\varphi$ in Eq. (4), one obtains the following expressions for the phase difference and frequency:

$$\Delta\varphi_{1,2} = \frac{\varepsilon\sqrt{\Omega^2 + \Delta^2 \pm 2\sqrt{\Omega\Delta(K + \Omega\Delta)}}}{2K + 4\Omega\Delta} \qquad (5)$$

$$\omega_{1,2} = \sqrt{\Omega^2 + \Delta^2 \pm 2\sqrt{\Omega\Delta(K + \Omega\Delta)}}, \qquad (6)$$

which correspond to the stable and unstable solutions to the system of Eqs. (4). One can see from Eqs. (5) and (6) that, at small detunings Δ, the phase difference $\Delta\varphi$ between the coupled oscillations at frequency ω is directly proportional to the oscillation frequency ω and inversely proportional to the coupling parameter K:

$$\Delta\varphi = \frac{\varepsilon\omega}{2K}. \qquad (7)$$

One can see from this expression that the close Fourier components of the coupled oscillators with slightly different parameters are locked-in, with the phase difference between them given by Eq. (7). It is significant that the time lag between the spectral components

$$\tau = \frac{\Delta\varphi}{\omega} \sim K^{-1} \qquad (8)$$

is independent of frequency and, hence, is the same for all spectral components. It is this fact that is responsible for the occurrence of the lag-synchronization regime, for which the dynamics of coupled chaotic oscillators have the same time lag for all frequencies. Relationship (8) is valid for many dynamic systems and, in all likelihood, has a universal character. Let us consider the manifestations of this relationship in some typical synchronization processes occurring in coupled chaotic systems.

We first consider the chaotic synchronization of two unidirectionally coupled self-excited oscillators [9, 10]. The driving oscillator is described by the system of dimensionless differential equations

$$\dot{x}_1 = -\nu_1[x_1^3 - \alpha x_1 - y_1],$$
$$\dot{y}_1 = x_1 - y_1 - z_1, \quad \dot{z}_1 = \beta y_1, \qquad (9)$$

and the driven oscillator is described, correspondingly, by

$$\dot{x}_2 = -\nu_2[x_2^3 - \alpha x_2 - y_2] + \nu_2 K(x_1 - x_2),$$
$$\dot{y}_2 = x_2 - y_2 - z_2, \quad \dot{z}_2 = \beta y_2, \qquad (10)$$

where $x_{1,2}$, $y_{1,2}$, and $z_{1,2}$ are the dynamic variables characterizing the states of the driving and driven oscillators, respectively. The controlling parameters were chosen to be $\alpha = 0.35$, $\beta = 300$, $\nu_1 = 100$, and $\nu_2 = 125$. The difference between ν_1 and ν_2 provides a slight nonidentity of the oscillators.

The time lag τ between the time realizations of coupled oscillators is shown in Fig. 1 as a function of the coupling parameter K. In this range of coupling param-
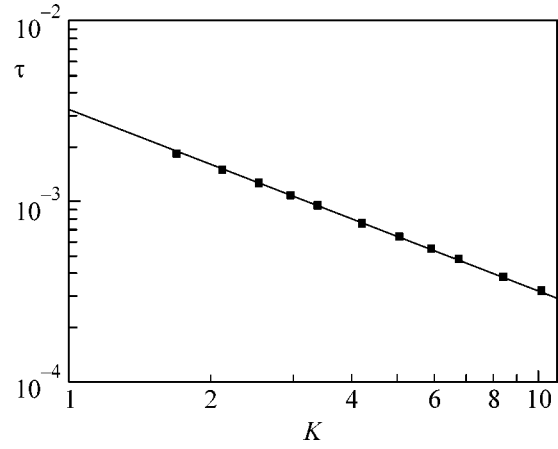

Fig. 1. (■) Time lag τ as a function of the coupling parameter K for two unidirectionally coupled chaotic oscillators (9) and (10) with slightly different parameters. The straight line on the log–log scale corresponds to the power law $\tau \sim K^{-1}$.

eters, the lag-synchronization regime prevails. One can clearly see that the time lag obeys the power law $\tau \sim K^n$ with $n = -1$, in accordance with theoretical expression (8).

As a second example, we consider two coupled Ressler systems in the dynamic chaos regime:

$$\dot{x}_{1,2} = -\omega_{1,2}y_{1,2} - z_{1,2} + K(x_{2,1} - x_{1,2}),$$
$$\dot{y}_{1,2} = \omega_{1,2}x_{1,2} + ay_{1,2} + K(y_{2,1} - y_{1,2}), \qquad (11)$$
$$\dot{z}_{1,2} = p + z_{1,2}(x_{1,2} - c),$$

where ε is the coupling parameter, $\omega_1 = 0.98$, and $\omega_2 = 1.03$. The controlling parameters were chosen to be $a = 0.22$, $p = 0.1$, and $c = 8.5$. For the coupling parameter $0.04 \lesssim K \lesssim 0.14$, systems (11) are in the phase-synchronization regime, and at $K > 0.14$, they occur in the lag-synchronization regime (see [11]).

The time lag τ between the main Fourier components of the interacting chaotic oscillators is shown in Fig. 2 as a function of the coupling parameter K. The main frequency in the spectrum is close to $\omega = 1$ and slightly changes with an increase in the coupling parameter. After the main spectral components of the interacting oscillators are locked-in (this corresponds to the phase-synchronization regime; see also [7]), the time lag between them obeys universal power law (8).

Thus, chaotic synchronization of the coupled oscillators proceeds as follows. At a certain value of the coupling parameter, the main spectral components are locked-in, which corresponds to the phase-synchronization regime. If this main frequency component dominates the Fourier spectrum, the phase-synchronization regime can easily be tested by the traditional methods using so-called continuous chaotic-signal phase (see [1, 12]); otherwise, different methods should be used (see [7]). As the coupling parameter increases, an increasing number of spectral components become locked-in, with
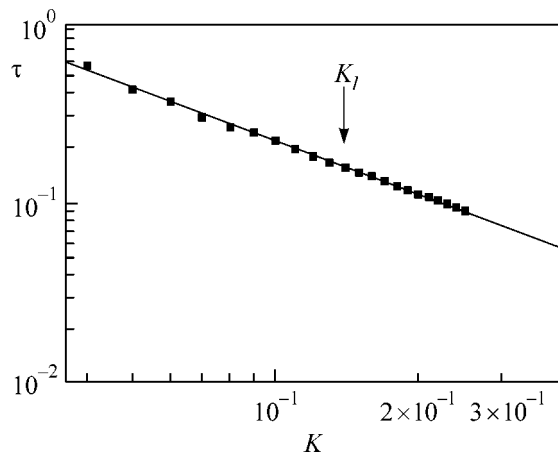
Fig. 2. (■) Time lag τ between the main Fourier components of interacting chaotic oscillators (11) vs. the coupling parameter K. The straight line corresponds to the power law $\tau \sim K^{-1}$. The arrow indicates the value of coupling parameter $K_l \approx 0.14$ corresponding to the onset of the lag-synchronization regime.
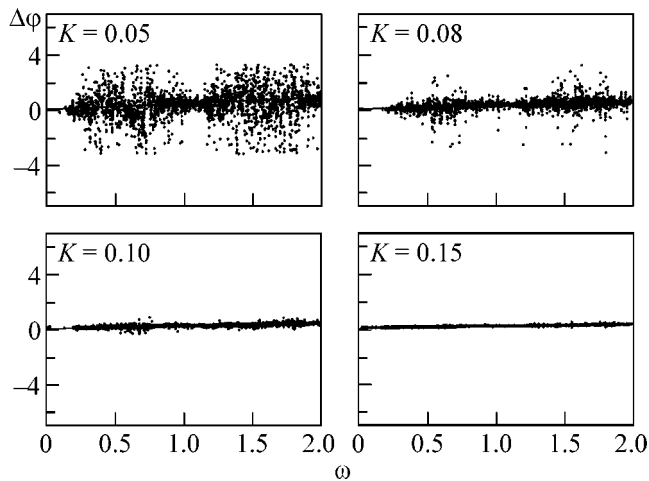

Fig. 3. Phase difference $\Delta\varphi$ for the different Fourier components of the coupled Ressler systems. Since the phase difference between the synchronized spectral components obeys Eq. (7), the value of $\Delta\varphi$ for the locked-in frequencies should fall on a straight line. One can clearly see that, as the coupling parameter increases, more and more spectral components become locked-in.

the time lag obeying universal dependence (8) for all of them. This is shown in Fig. 3, which demonstrates that the number of synchronized spectral components of the coupled systems increases with increasing the coupling parameter K. The synchronization of the individual spectral components is seen from the fact that the corresponding phase difference between these components obeys Eq. (7), while the corresponding point at the $(\Delta\varphi, \omega)$ plane falls on a straight line.

The locking-in of all frequency components corresponds to the lag-synchronization regime. As the coupling strength further increases, the time lag τ tends to zero, according to Eq. (8), and the coupled oscillations tend to the regime of complete synchronization.

Thus, we have revealed a rather universal mechanism for establishing the regime of chaotic synchronization in coupled dynamic systems. The mechanism is based on the appearance of phase coupling between the frequency components of the Fourier spectra of the interacting chaotic oscillators. The obtained results can serve as a criterion for the existence (or nonexistence) of the lag-synchronization regime in the coupled dynamic systems.

REFERENCES

1. A. Pikovsky, M. Rosenblum, and J. Kurths, *Synchronization: A Universal Concept in Nonlinear Sciences* (Cambridge Univ. Press, Cambridge, 2001).

2. A. S. Dmitriev and A. I. Panas, *Dynamical Chaos. New Information Carriers for Communication Systems* (Fizmatlit, Moscow, 2002) [in Russian].

3. R. C. Elson *et al.*, Phys. Rev. Lett. **81**, 5692 (1998).

4. N. F. Rulkov, M. M. Sushchik, L. S. Tsimring, and H. D. I. Abarbanel, Phys. Rev. E **51**, 980 (1995).

5. M. G. Rosenblum, A. S. Pikovsky, and J. Kurths, Phys. Rev. Lett. **78**, 4193 (1997).

6. L. M. Pecora and T. L. Carroll, Phys. Rev. A **44**, 2374 (1991).

7. A. A. Koronovskiĭ and A. E. Hramov, Pis'ma Zh. Éksp. Teor. Fiz. **79**, 391 (2004) [JETP Lett. **79**, 316 (2004)].

8. A. A. Koronovskiĭ and A. E. Khramov, *Continuous Wavelet Analysis and Its Applications* (Fizmatlit, Moscow, 2003) [in Russian].

9. G. P. King and S. T. Gaito, Phys. Rev. A **46**, 3092 (1992).

10. A. A. Koronovskiĭ, A. E. Hramov, and I. A. Khromova, Pis'ma Zh. Tekh. Fiz. **30**, 69 (2004) [Tech. Phys. Lett. **30**, 291 (2004)].

11. M. G. Rosenblum *et al.*, Phys. Rev. Lett. **89**, 264 102 (2002).

12. T. E. Vadivasova and V. S. Anishchenko, Radiotekh. Élektron. (Moscow) **49**, 76 (2004).

Translated by V. Sakun

Induced Emission from Cd$_x$Hg$_{1-x}$Te at a Wavelength of 3400 nm at 77 K

Yu. N. Nozdrin[1], A. V. Okomel'kov[1,*], A. P. Kotkov[2,], A. N. Moiseev[2], and N. D. Grishnova[2]**

[1] *Institute of Physics of Microstructures, Russian Academy of Sciences, Nizhni Novgorod, 603950 Russia*
*e-mail: okom@ipm.sci-nnov.ru
[2] *Institute of Chemistry of High-Purity Substances, Russian Academy of Sciences, Nizhni Novgorod, 603950 Russia*
**e-mail: kotkov@ihps.nnov.ru
Received April 30, 2004

The results are reported on the observation of the induced emission from Cd$_x$Hg$_{1-x}$Te samples optically pumped by a pulsed Nd:YAG laser at temperatures $T < 77$ K. In the wave range $\lambda \sim 3300$–3600 nm, both stimulated and spontaneous emission were observed. The experimentally measured emission spectra are analyzed. The properties of the spectra from the samples are discussed and the possible applications are considered. © 2004 MAIK "Nauka/Interperiodica".

PACS numbers: 78.45.+h

Lasers and photodetectors operating in the mid- and far-IR range (at wavelengths approximately from 3 to 20 μm) attract considerable attention of researchers all over the world. The mastering of this wavelength range is important, e.g., for

(i) communication purposes, since the "transparency windows" in the Earth's atmosphere lie in this range (3.5–4, 4.5–5, 8–14, and 16–23 μm);

(ii) spectroscopy and monitoring of the ambient medium, since this range contains the frequencies of vibrational–rotational transitions in many molecules.

Semiconductor laser diodes and quantum cascade lasers belong to the few active devices operating in this range in actual practice. In accordance with their operation principle, both types of devices are essentially heterogeneous structures. This circumstance makes the fabrication of such structures rather complicated and costly. It is well known that the characteristic frequencies of the radiative interband transitions in narrow-gap semiconducting films such as Cd$_x$Hg$_{1-x}$Te (MCT) may lie in the same range as for quantum cascade lasers. Moreover, the MCT samples synthesized at present most frequently have a stoichiometric composition such that the characteristic frequency of radiative interband transitions (determined by the band gap) precisely "falls" in the mid-IR range.

From this point of view, MCT lasers (provided that such devices could be developed for a broad range of stoichiometric compositions) could probably compete with cascade lasers. A single MCT film has a much simpler structure than the semiconductor quantum superlattice of a cascade laser. Moreover, an MCT film itself is a waveguide because of the high permittivity of this material (15–20); this may facilitate the formation of the laser cavity modes by the use of the total internal reflection at film boundaries. In addition, in contrast to the structures of quantum cascade lasers, there is no need to grow quantum-sized layers using precision technology, since the typical thickness of MCT films usually varies from a few to tens of micrometers. The technology for preparing high-quality epitaxial MCT films has been extensively developed in connection with manufacturing IR detectors. We performed our measurements on the structures grown at the Institute of Chemistry of High-Purity Substances, Russian Academy of Sciences, where the MOCVD method for preparing epitaxial MCT layers with different stoichiometric composition is currently being developed [1, 2].

The earlier studies aimed at designing MCT lasers were scarce; as a result, many fundamental problems remained unsolved. The spontaneous and coherent emission from MCT crystals pumped by a GaAs semiconductor laser were observed in [3] (see also [4, 5]). The induced radiation was observed in a wavelength range of 3.8–4.1 μm at a temperature of about 12 K, while the spontaneous emission was detected up to a wavelength of 15 μm.

Optically pumped lasers emitting in the wavelength range from 1.25 to 2.97 μm at the liquid nitrogen temperature were reported in [6]. CW lasing at a wavelength of 2.79 μm was obtained at a temperature of 12 K. The stimulated emission from MCT films with $x = 0.5$ was observed in [7] at a wavelength of 2.13 μm. The threshold pumping power in this case was about 10 kW/cm^2 at the liquid nitrogen temperature.

The stimulated emission from MCT films with $x = 0.46$, which were grown on a semi-insulating cadmium telluride substrate, was observed in [8]. Lasing at a
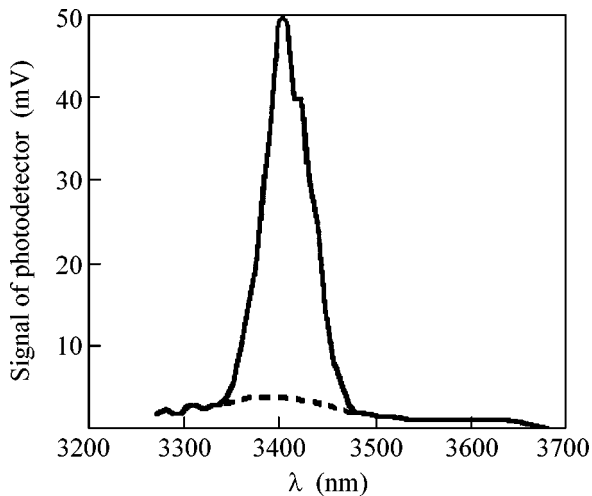
Fig. 1. The spectral composition of radiation emitted from a $Cd_xHg_{1-x}Te$ sample at $T \approx 77$ K (MCT 638/1 sample, $x \approx 0.376$). Photodetector is the MCT 641/1 sample with $x \approx 0.272$. The dashed curve shows the spectrum for the photo-excitation intensity lower than the threshold value ($P < 4$ kW/cm^2). For the photopumping intensities $P \geq 4$ kW/cm^2, a narrow line (solid curve in the figure) appears against the background of this pedestal.

wavelength of 2.42 μm was observed under pumping by an Nd:YAG laser with a power exceeding 2.8 kW/cm^2 at a temperature of 10 K.

These data show that the maximal wavelength of the observed induced emission at liquid nitrogen temperature was 2.97 μm. This is usually explained by the fact that, for the narrower band gaps (i.e., relatively small values of x on the order of 0.2 and smaller), the relative role of the nonradiative Auger-recombination transitions increases (see [9]). However, a constraint on the lasing frequency associated with the nonradiative recombination with the participation of impurities can, probably, exist. In this case, lasing in the longer wavelength range can obviously be expected for the more perfect and "pure" samples. Our experimental results show that electromagnetic radiation at lower frequencies and at higher temperatures can be observed in the studied MCT films.

Experimental data and discussion. In this paper, we report the experimental data obtained on electromagnetic radiation emitted from $Cd_xHg_{1-x}Te$ epitaxial layers at the liquid nitrogen temperature under the pulsed optical pumping by a Nd:YAG laser (operating at a wavelength of 1.064 μm). We used MCT samples with a thickness from a few to tens of micrometers grown on GaAs semi-isolating substrates with a buffer layer of high-resistivity CdTe at the Institute of Chemistry of High-Purity Substances (ICHPS), Russian Academy of Sciences. The samples placed on a copper cold finger were photoexcited from the side of the epitaxial layer. A spherical metallic mirror projected the radiation from the end face of the epitaxial layer onto

the input slit of a standard monochromator that could rotate the signal, in accordance with its frequency spectrum, with the help of diffraction gratings. At the device output, the monochromatic signal was recorded by a photodetector cooled to the liquid nitrogen temperature. The role of the photodetector was played by another $Cd_xHg_{1-x}Te$ sample with the appropriate stoichiometric composition, which was also grown at the ICHPS. If necessary, Ge filters were placed ahead of the photodetector for suppressing the pump-wave scattered radiation. The signal from the photodetector was fed to an oscilloscope which was actuated synchronously by a pump pulse from the Nd:YAG laser.

Figure 1 shows a typical spectrum of electromagnetic radiation emitted by an MCT sample (MCT 638/1) with $x = 0.376$ and thickness $h \approx 8.9$ μm at $T = 77$ K. The sample had the p-type conductivity and was grown on a GaAs substrate with the (111) crystallographic orientation. The sample had the shape of a regular triangle with a side of 5 mm. For the optical pump intensity $P < 4$ kW/cm^2, the spectrum has the shape of a broad pedestal of a moderate amplitude, shown by the dashed curve in Fig. 1. For the pump intensities $P \geq 4$ kW/cm^2, a narrow line appears against the background of the pedestal. The pedestal can be naturally associated with the spontaneous emission, and the narrow line, with the stimulated emission (superluminescence). Thus, we observed the effect of radiation-spectrum narrowing for photoexcitation intensities above the threshold value, which was $P \approx 4$ kW/cm^2 in our case.

The closest result was obtained in [8]. The spectral line of stimulated radiation in [8] corresponds to a wavelength of about 2420 nm, and the linewidth almost coincides with that in Fig. 1. It is worth noting that the measurements in [8] were made at $T = 12$ K, while our measurements were performed at $T \geq 77$ K. The fact that the temperature in our experiment was six to seven times higher and the spectral linewidth was virtually the same ($\Delta\lambda \approx 50$–60 nm) confirms our interpretation of this line as a stimulated-emission line.

In our experiments, the sample surface was illuminated incompletely (only isolated areas were exposed to radiation). Therefore, we, in fact, measured the superluminescence spectra from different illuminated regions. The simplicity of observing the stimulated radiation even in the absence of a cavity in the system indicates that the gain is quite large.

Figure 2 shows the emission spectra from different samples prepared from the same $Cd_xHg_{1-x}Te$ film with $x \approx 0.376$, as well as the spectral lines obtained by illumination of different areas of the same sample. It can be seen that these lines differ in the position of the emission peak λ_{max}, linewidth, and shape. The scatter in the values of λ_{max} corresponding to different film areas is approximately equal to 3.6%, which is likely an indication of the inhomogeneity of the given film. This means that the fluctuations of the composition (deviation from the stoichiometricity) of the samples were approxi-
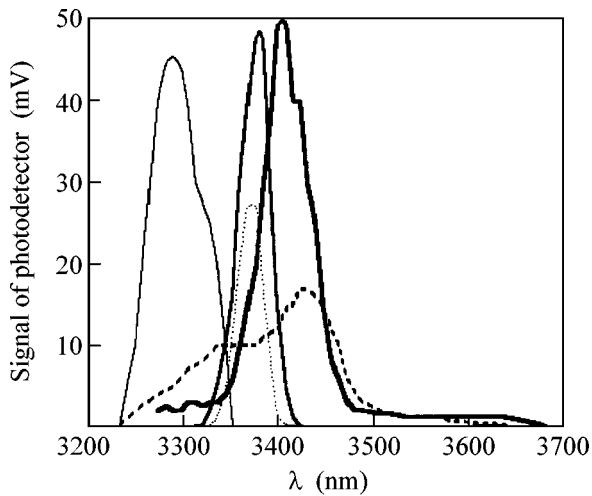
Fig. 2. The spectral composition of the radiation emitted from Cd$_x$Hg$_{1-x}$Te samples (dependence of the radiation intensity on the wavelength). Different curves were obtained from different emitters prepared from the same sample, i.e., Cd$_x$Hg$_{1-x}$Te film (MCT 638/1 sample, $x \approx 0.376$).

mately equal to 3–4%. The "irregular" line shape observed in most samples (e.g., the dotted curve in Fig. 2) is evidence of a spatial inhomogeneity. A certain scatter in the photoexcitation conditions (illumination of the neighboring areas) leads to an inhomogeneously broadened superluminescence line.

The linewidths in the superluminescence spectrum in Fig. 2 almost coincide with the spectral width in [8]; however, in contrast to our results, the experimental data were obtained in [8] at $T = 12$ K at the wavelength $\lambda_{max} \approx 2420$ nm. In [3], the stimulated-emission lines were observed in the range $\lambda \sim 4100$ nm, but also at $T = 12$ K. Thus, we report here the observation of the

stimulated emission from the Cd$_x$Hg$_{1-x}$Te structures at the liquid nitrogen temperatures in the wavelength range $\lambda \sim 3250$–3450 nm. The observation of the stimulated emission at nitrogen temperatures allows one to speak about the real possibilities of its applications. It should specially be noted that the variations of the superluminescence frequency observed from different sample areas may render this effect applicable to the diagnostics of inhomogeneities in the stoichiometric composition. The latter fact is very important for improving the process of preparation of Cd$_x$Hg$_{1-x}$Te-based structures.

REFERENCES

1. A. N. Moiseev, A. P. Kotkov, V. V. Dorofeev, and N. D. Grishnova, Neorg. Mater. **40**, 1 (2004).

2. K. O. Boltar', N. I. Yakovleva, V. P. Golovin, *et al.*, Prikl. Fiz., No. 5, 95 (2003).

3. I. Melngailis and A. J. Strauss, Appl. Phys. Lett. **8**, 179 (1966).

4. R. Dornhaus and G. Nimtz, Solid State Phys. **78**, 1 (1976).

5. N. S. Baryshev, *Properties and Application of Narrow-Band Semiconductors* (UNIPRESS, Kazan, 2000) [in Russian].

6. T. C. Hartman, J. Electron. Mater. **8**, 191 (1979).

7. V. I. Ivanov-Omskiǐ, K. E. Mironov, R. B. Rustamov, and V. A. Smirnov, Pis'ma Zh. Tekh. Fiz. **10**, 1021 (1984) [Sov. Tech. Phys. Lett. **10**, 428 (1984)].

8. K. K. Mahavadi, J. Bleuse, X. Chu, and J. P. Faurie, Appl. Phys. Lett. **55**, 1285 (1989).

9. G. Nimtz, Phys. Rep. **63**, 265 (1980).

Translated by N. Wadhwa

Optical Amplification of Photoinduced Polarizability Gratings in Phosphate Glasses

M. K. Balakirev, L. I. Vostrikova*, V. A. Smirnov, and M. V. Entin

Institute of Semiconductor Physics, Siberian Division, Russian Academy of Sciences, Novosibirsk, 630090 Russia
*e-mail: vostrik@isp.nsc.ru
Received May 11, 2004

It is experimentally demonstrated that second-order polarizability gratings preliminarily recorded using bichromatic light in a phosphate glass can be amplified under the action of monochromatic radiation. The amplification effect takes place irrespective of the polarization and direction of propagation of the amplifying radiation and is achieved at various wavelengths. The phenomenon is related to the asymmetry of optical transitions between local centers in an isotropic medium in the presence of electric field. It is theoretically shown that this system may feature the formation of alternating electric field domains with dimensions depending on the grating amplitude. © 2004 MAIK "Nauka/Interperiodica".

PACS numbers: 42.79.Dj; 42.70.Ce

As is known, prolonged exposure of a glass to mutually coherent bichromatic radiation with ω and 2ω frequencies may decrease the optical symmetry of the material and give rise to even orders in the expansion of polarization with respect to the light field. The induced nonlinear polarizability is usually characterized by inhomogeneous distribution and forms a polarizability grating (PG) [1–5]. It was established that the PGs in some oxide glasses may exhibit amplification under the action of a monochromatic radiation [5–9]. The amplification of photoinduced PGs was observed under phase-matched conditions and could be explained by the second harmonic generation (SHG) of pumping light.[1]

This paper reports on the observation of optical amplification of PGs independent of the polarization and direction of propagation of the amplifying radiation and, hence, not related to nonlinear wave interactions.

It should be noted that induced polarizability of a PG is believed to be caused by the electrostatic field $\mathbf{E}(\mathbf{r})$ appearing due to charge separation and accumulation in a glass as a result of the coherent photogalvanic effect [12–14] or the long-term photopolarization [1, 15, 16]. Two mutually coherent light waves with the frequencies ω and 2ω and wave vectors $\mathbf{k}_\omega$ and $\mathbf{k}_{2\omega}$ determine the characteristic wave vector of modulation of the electrostatic field, $\mathbf{k} = \mathbf{k}_{2\omega} - 2\mathbf{k}_\omega$, while the field

envelope is determined by the distribution of $\mathbf{E}_\omega^2(\mathbf{r})$ and $\mathbf{E}_{2\omega}(\mathbf{r})$ fields. The static field generates spatially periodic gratings of nonlinear polartizabilities for the light field. In the lowest order with respect to the field $\mathbf{E}$, there arises $\hat{\chi}_2 = \hat{\chi}_3 \mathbf{E}(\mathbf{r})$, where $\hat{\chi}_3$ is the third-order polarizability.

The experiments were performed with a bulk ($1 \times 1 \times 1$-cm) sample of alkali metaphosphate glass based on KPO_3 with additives of 20 mol % Sb_2O_3, 14 mol % Nb_2O_3, and 0.2 mol % Er_2O_3. The experimental procedure was as follows.

In the first stage, the initial $\chi^{(2)}$ PG was prepared using the experimental arrangement depicted in Fig. 1. The radiation of a pulsed YAG:Nd^{3+} laser ($\lambda = 1.06$ μm;
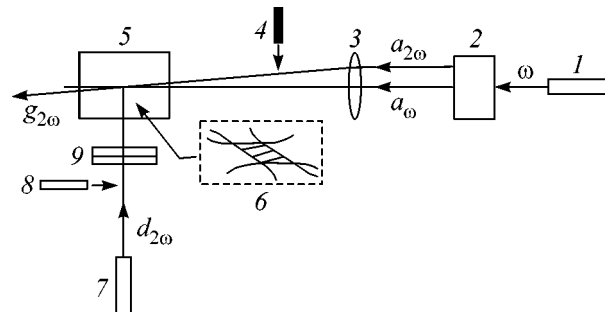
Fig. 1. Schematic diagram of the experimental arrangement: (*1*) YAG:Nd^{3+} laser; (*2*) optical elements for frequency doubling and spatial separation of ω and 2ω beams; (*3*) lens; (*4*) shutter; (*5*) glass sample; (*6*) $\chi^{(2)}$ PG; (*7*) additional YAG:Nd^{3+} laser; (*8*) $\lambda/2$ plate; (*9*) cylindrical lens.

---

[1] The spatial periodicity of the photoinduced PGs is phase-matched for the ω and 2ω waves forming the grating. The conditions of spatial synchronism for the effective three-wave processes (SHG [2, 3] and degenerate parametric amplification [10] in $\chi^{(2)}$ PGs) involving these waves are automatically fulfilled. The equiphase character of PGs leads to effective Bragg self-diffraction of light in the regions of modulated refractive index [4, 11].

pulse duration, ~10 ns; repetition rate, 12.5 Hz; pulse energy, ~46 mJ) and its second harmonic (transformation coefficient, ~0.1) were separated into two channels by a special system of optical elements. The second radiation component in each channel was attenuated by 10^{10}. The fundamental and second harmonic radiation components (a_ω and $a_{2\omega}$ beams in Fig. 1) were linearly polarized in the plane of convergence and focused by a lens to intersect inside the glass sample. The angle of convergence of the beams incident onto the sample was 6.2°, the beam diameters at the focus were ~170 and 120 μm, and the peak intensities at the waist were $I_\omega \sim 10^{10}$ W/cm^2 and $I_{2\omega} \sim 10^9$ W/cm^2.

Exposure to the bichromatic light resulted in the formation of a $\chi^{(2)}$ PG in the glass. The PG amplitude was monitored by measuring the SHG efficiency for the a_ω beam passing through the grating ($g_{2\omega}$ beam in Fig. 1). The SHG signals detected by a photoelectron multiplier were digitized using an analog-to-digital converter and fed to a computed for processing and display. The radiation energy was averaged over 10–40 pulses. The detection threshold of the measuring system was 10^{-11} J per pulse. For the measurement of the $g_{2\omega}$ signal, the $a_{2\omega}$ beam was at the sample entrance was blocked for 5–10 s with a 5–10 min interval.

In the second experimental step (performed after preparation on the initial $\chi^{(2)}$ PG), the PG region was illuminated by the a_ω or $a_{2\omega}$ beam. In the former case, the SHG was monitored simultaneously. If the PG was illuminated by the $a_{2\omega}$ beam, the SHG dynamics was monitored by periodically blocking this beam for several seconds. During this period of time, the a_ω was passed and the $g_{2\omega}$ beam energy was measured as described above. The seeding PGs were measured for a second harmonic conversion efficiency of up to $\eta_g \sim 10^{-8}$, where η_g was determined as the energy ratio of the $g_{2\omega}$ and a_ω beams.

Figure 2 shows the time variation of the conversion efficiency η_g for all experiments. Curve *1* describes the process of PG recording under the action of bichromatic light up to saturation. The maximum second harmonic conversion coefficient in this case was $\eta_g \sim 1.5 \times 10^{-5}$. The characteristic PG lifetime in the sample studied was 7–10 days. Curves *2–7* show the results of experiments on the amplification of photoinduced PGs.

Curves *2* and *3* in Fig. 2 show the amplification of PG in the glass sample under the action of radiation at a fundamental frequency (a_ω beam) with orthogonal polarizations. The η_g increased and exhibited saturation, which was indicative of increased PG amplitude. The effect of polarization on η_g was insignificant.

Curves *4* and *5* show the amplification of the initial PG under the action of the $a_{2\omega}$ beam, which was monitored as described above. As can be seen, the degree of amplification is comparable with that observed in the previous case, despite the tenfold difference in intensi-
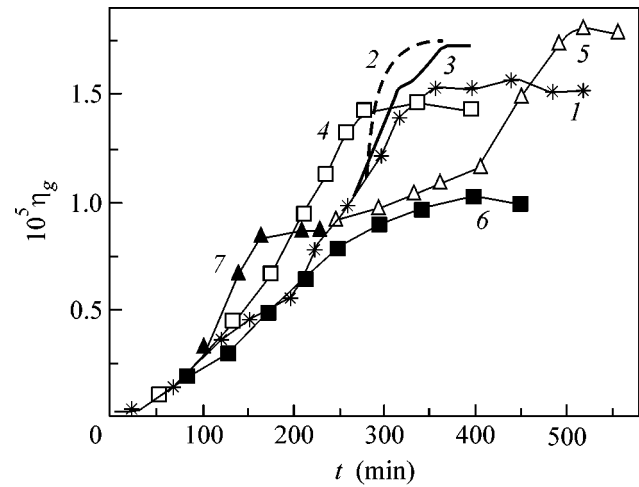

Fig. 2. Kinetics of the SHG efficiency for $\chi^{(2)}$ PG in phosphate glass: (*1*) PG prepared by bichromatic radiation; (*2*, *3*) PG amplified by the a_ω beam; (*4*, *5*) PG amplified by the $a_{2\omega}$ beam; (*6*, *7*) PG amplified by the $d_{2\omega}$ beam. Curves *2*, *4*, *6* correspond to the light polarized parallel to the plane of convergence of the recording beams, and curves *3*, *5*, *7* correspond to the light of orthogonal polarization.

ties of the a_ω and $a_{2\omega}$ beams. Rotation of the polarization plane also rather weakly influenced the efficiency of amplification (cf. curves *4* and *5*).

The whole body of the obtained results showed that the possible contribution of three-wave processes, leading to the SHG equiphase with the grating, is insignificant or absent. In order to exclude the possibility of three-wave processes capable of pumping the grating, we performed a special experiment using an additional YAG:Nd^{3+} laser equipped with a frequency converter ($\lambda = 0.53$ μm; pulse duration, ~5 ns; repetition rate, 12 Hz; pulse energy, ~40 mJ) (Fig. 1). The beam of this laser was focused on the sample from the side face by means of a cylindrical lens ($d_{2\omega}$ beam) so as to cover the whole region of the initial PG with a length of ~5 mm. The intensity of this beam in the focal plane was ~2 × 10^9 W/cm^2. The result of amplification of the initial PG by the $d_{2\omega}$ beam is also shown in Fig. 2 (curves *6*, *7*). As can be seen, the efficiency of amplification is also independent of the polarization and is comparable with the efficiency of "parallel" amplification (curves *4* and *5*).

Let us discuss the results obtained. The experimental data show that amplification of the photoinduced PGs in phosphate glass takes place in the case of monochromatic illumination, irrespective of the radiation frequency, polarization, and direction of propagation. This behavior disagrees with the mechanism of amplification of photoinduced PGs in oxide glasses proposed previously [5, 6, 9, 13] based on the phase-matched wave interaction. Indeed, according to this mechanism, the direction of propagation, polarization, and frequency of amplifying radiation would be matched with
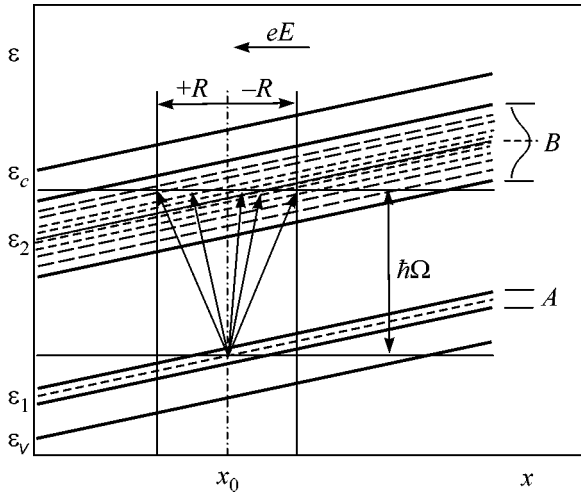
Fig. 3. Schematic diagram of optical transitions (see the text for explanations).

the same characteristics of the radiation used to form the initial PG. In our experiments, the effect of amplification was observed when all these conditions were violated.

We believe that the mechanism of amplification is related to slow variations of the material constants (effective coefficients of quadratic nonlinearity) under the action of light. The symmetry of the initial material forbids quadratic nonlinearity and the action of monochromatic radiation also cannot induce such nonlinearity. Therefore, quadratic nonlinearity does not appear under illumination and the mechanism has to be related to self-enhanced symmetry reduction (the rate of variation of the deviation from isotropic symmetry increases with the magnitude of deviation). The most natural agent mediating in this process can be a quasi-stationary electric field enhanced under the action of light. The possible mechanism of the field amplification is via asymmetric transitions between localized states in the presence of a static electric field. In order to provide for the amplification effect, it is necessary to ensure preferential excitation of electrons and their spatial displacement against the force developed by the electric field. Let us assume that glass contains two groups of localized single-level states A and B (see Fig. 3, where x is the coordinate and ϵ is the energy). Let the density of states in group B be dome-shaped with a maximum at ϵ_2. In the equilibrium state, levels A are filled by electrons, while levels B are empty. Let us introduce the characteristic length R of electron jumps in space, determining the probability of tunneling transitions between levels, and assume the R value to be constant. Upon absorption of a light quantum $\hbar\Omega$, electrons from levels A pass to levels B as indicated by arrows in Fig. 3. As can be seen from this scheme, when the energy of light quantum is sufficiently large, $\hbar\Omega > \epsilon_2 - \epsilon_1$, the electron transitions will be performed predominantly

against the external force, because the density of states for such transitions is higher than that for the transitions along the force (for $\hbar\Omega < \epsilon_2 - \epsilon_1$, the effect changes to the opposite). If the excited electron returns to an unexcited state with isotropic relaxation in the space, the medium will feature a flow of electrons equivalent to the appearance of an absolute negative photoconductivity [17, 18]. On the contrary, if the excited electron relaxes exactly to the initial state (germinate recombination), the medium will feature the negative photopolarization [15, 19].

The above scheme can be applied to our experiments, assuming that the glass contains two groups of active levels of type B separated from level A by ≤ 1.17 and 2.34 eV and, accordingly, providing amplification of the initial PG under the action of radiation of the fundamental and doubled frequencies. In the general case, glasses may feature even more complicated schemes of asymmetric phototransitions involving multilevel centers [20] and combined mechanisms. Available experimental data do not allow us to judge unambiguously in favor of some particular mechanism. However, taking into account the large lifetimes of the photoinduced PGs and the absence of effective photoerasure (photoconductivity) in the phosphate glass studied, we believe that the observed amplification is most likely related to the negative photopolarization.

Now, let us briefly consider the kinetics of the observed phenomenon, proceeding from the mechanism of negative photopolarization. Evidently, the rate of increase of the polarization $\mathbf{P}_s$ is nonlinear with respect to the field and has a domelike shape. The simplest equation describing this behavior is as follows:

$$\frac{d}{dt}\mathbf{P}_s = -\alpha\mathbf{E} - \beta\mathbf{E}^3 + \gamma\mathbf{E}^5, \qquad (1)$$

where the first two terms on the right-hand side describe the amplification of $\mathbf{P}_s$ and the third term accounts for the damping; α, β, and γ are coefficients dependent on the field strength (positive signs at α and β correspond to amplification). Excluding polarization from Eq. (1), we obtain

$$\frac{d}{dt}\mathbf{E} + \mathbf{E}(\Gamma - \beta\mathbf{E}^2 + \gamma\mathbf{E}^4) = 0, \quad \Gamma \equiv \frac{1}{\tau} - \alpha, \quad (2)$$

where Γ is the linear decrement and τ characterizes the time of relaxation of the electric field. The latter quantity may be determined both by the photopolarization lifetime and by the conductivity of the medium. Depending on the incident light intensity, Γ can be either positive or negative. The effect of field amplification takes place, provided that

$$\Gamma - \beta\mathbf{E}^2 + \gamma\mathbf{E}^4 < 0. \qquad (3)$$

For $\Gamma > 0$ and $\beta^2 \geq 4\gamma\Gamma$, the system formally has two stationary states (thresholds):

$$E_a^2 = \frac{1}{2\gamma}(\beta - \sqrt{\beta^2 - 4\gamma\Gamma}),$$

$$E_b^2 = \frac{1}{2\gamma}(\beta + \sqrt{\beta^2 - 4\gamma\Gamma}).$$

The first state is unstable. The fields $E > E_a$ are amplified, while the fields $E < E_a$ decay. In other words, the first threshold (E_a) corresponds to the onset of amplification, and the second (E_b), to saturation. For $\Gamma \longrightarrow 0$, we have $E_a \longrightarrow 0$ and only the saturation threshold exists. Finally, for $\beta^2 < 4\gamma\Gamma$, the amplification effect is absent. The existence of two thresholds for a spatial sine-shaped grating implies the formation of field domains. Indeed, the region with $E(x) > E_a$ increases to saturation, while the region with $E(x) < E_a$ tends to zero. Thus, depending on the initial grating amplitude, the medium contains alternating domains of various dimensions. It should also be noted that a similar pattern of field amplification should also take place in the case of absolute negative photoconductivity.

In conclusion, we experimentally demonstrated the possibility of amplification of a second-order optical nonlinearity in the initially isotropic medium (phosphate glass) under the action of a monochromatic radiation. It was established that this phenomenon is not related to nonlinear wave interactions. The most probable mechanism responsible for the observed effect is negative photopolarization via single-photon transitions between impurity levels in the presence of electric field.

REFERENCES

1. R. H. Stolen and H. W. K. Tom, Opt. Lett. **12**, 585 (1987).
2. Yu. V. Glushchenko and V. B. Smirnov, Opt. Spektrosk. **72**, 990 (1992) [Opt. Spectrosc. **72**, 538 (1992)].
3. D. S. Dianov and E. M. Starodubov, Kvantovaya Élektron. (Moscow) **22**, 419 (1995).
4. M. K. Balakirev and V. A. Smirnov, Pis'ma Zh. Éksp. Teor. Fiz. **61**, 537 (1995) [JETP Lett. **61**, 544 (1995)].
5. M. K. Balakirev, Phys. Vibr. **6**, 233 (1998).
6. M. I. Dyakonov and A. S. Furman, Comments Condens. Matter Phys. **16**, 19 (1992).
7. M. Ya. D'yakonov and A. S. Furman, Opt. Spektrosk. **79**, 871 (1995) [Opt. Spectrosc. **79**, 798 (1995)].
8. M. K. Balakirev, L. I. Vostrikova, and V. A. Smirnov, Pis'ma Zh. Éksp. Teor. Fiz. **63**, 166 (1996) [JETP Lett. **63**, 176 (1996)].
9. M. K. Balakirev, L. I. Vostrikova, and V. A. Smirnov, Pis'ma Zh. Éksp. Teor. Fiz. **66**, 771 (1997) [JETP Lett. **66**, 809 (1997)].
10. M. K. Balakirev, V. A. Smirnov, and L. I. Vostrikova, Opt. Commun. **178**, 181 (2000).
11. M. K. Balakirev, L. I. Vostrikova, and V. A. Smirnov, Kvantovaya Élektron. (Moscow) **32**, 546 (2002).
12. É. M. Baskin and M. V. Éntin, Pis'ma Zh. Éksp. Teor. Fiz. **48**, 554 (1988) [JETP Lett. **48**, 601 (1988)].
13. E. M. Dianov, P. G. Kazanskiǐ, and D. Yu. Stepanov, Kvantovaya Élektron. (Moscow) **17**, 926 (1990).
14. V. B. Sulimov, Zh. Éksp. Teor. Fiz. **101**, 1749 (1992) [Sov. Phys. JETP **74**, 932 (1992)].
15. B. P. Antonyuk, Opt. Commun. **181**, 191 (2000).
16. M. K. Balakirev and V. A. Smirnov, Pis'ma Zh. Éksp. Teor. Fiz. **77**, 264 (2003) [JETP Lett. **77**, 217 (2003)].
17. V. N. Novikov and B. I. Sturman, Zh. Éksp. Teor. Fiz. **94** (7), 226 (1988) [Sov. Phys. JETP **67**, 1423 (1988)].
18. V. K. Malinovskiǐ, V. N. Novikov, and B. I. Sturman, Zh. Éksp. Teor. Fiz. **91**, 594 (1986) [Sov. Phys. JETP **64**, 350 (1986)].
19. B. P. Antonyuk and V. B. Antonyuk, Usp. Fiz. Nauk **171**, 61 (2001) [Phys. Usp. **44**, 53 (2001)].
20. V. K. Malinovskiǐ, V. N. Novikov, and B. I. Sturman, Pis'ma Zh. Éksp. Teor. Fiz. **41**, 285 (1985) [JETP Lett. **41**, 349 (1985)].

Translated by P. Pozdeev

Transition from Strong to Weak Localization in the Split-Off Impurity Band in Two-Dimensional p-GaAs/AlGaAs Structures

N. V. Agrinskaya*, V. I. Kozub, D. V. Poloskin, A. V. Chernyaev, and D. V. Shamshur

Ioffe Physicotechnical Institute, Russian Academy of Sciences, St. Petersburg, 194021 Russia
*e-mail: nina.agrins@mail.ioffe.ru
Received April 8, 2004; in final form, May 19, 2004

A crossover from strongly localized behavior to weak localization (SL–WL) was observed in two-dimensional modulation-doped GaAs/Al$_{0.3}$Ga$_{0.7}$As structures as the impurity concentration increased. In this case, it was observed that the low-temperature dependence of the conductivity changed its character (from exponential to logarithmic) and the magnetoresistance changed its sign (from linear negative to root positive). For 2D structures, it is shown that this transition proceeds in the impurity band separated from the valence band by the mobility gap, whereas the effective mass in the impurity band is larger than in the valence band. © 2004 MAIK "Nauka/Interperiodica".

PACS numbers: 73.21.Fg; 73.20.Fz; 71.30.+h

1. INTRODUCTION

Both effects associated with disorder and effects of electron–electron interaction can play an important role in the vicinity of the metal–insulator (MI) transition in doped (both 3D and 2D) semiconductors. As for disorder effects, it is known that these lead to broadening of the impurity band and its subsequent coalescence with the conduction band. In this connection, it is often suggested that it is in the conduction band tail formed by disorder that the MI transition occurs. However, a number of magnetooptical and transport experiments at $n_c \leq n \leq 5n_c$ (where $n_c = (0.25/a)^3$ is the Mott estimate for the critical concentration for the metal–insulator transition) indicate that the transition to metallic conductivity proceeds in the split-off impurity zone [1, 2].

Strictly speaking, the above consideration relates to 3D. The scaling theory of localization predicts the absence of the metal–insulator transition in 2D, because all the states prove to be localized as the temperature tends to zero. Nevertheless, it is known that, in experiments performed with sufficiently clean structures [3], a transition from a dielectric to metallic behavior was observed as the electron concentration increased. The nature of this behavior has not been quite understood so far. Several mutually contradictory explanations have been proposed, including those associated with electron–electron interactions, with non-Fermi-liquid effects, and with simulations of the metallic behavior by temperature-dependent scattering [3, 4]. We incline to the latter suggestion and previously have proposed a model for the MI transition in 2D in which the observed behavior is explained by the coexistence of weakly localized states (fully described by the scaling theory of localization) and strongly localized states lying lower in energy [5]. It is suggested that the latter

states are not described by the scaling theory of localization and an analogue of the mobility edge can be introduced. In accordance with the scenario [6], the states localized in the vicinity of this mobility edge form a peak in the upper Hubbard band.

A transition from the regime of strong localization (SL) to the regime of weak localization (WL) or a SL–WL crossover was observed in contaminated or doped 2D structures as the carrier concentration increased [7, 8]. In this case, the question of whether the transition occurred in the tail of the allowed band or in the impurity band (separated from the conduction band) remained open.

In this work, we performed a corresponding study with respect to a particular system of a selectively doped structure of quantum wells that allow both single and double occupations of the localized states. Special attention was given to the character of the corresponding localized states. We observed a SL–WL crossover in 2D GaAs/Al$_{0.3}$Ga$_{0.7}$As structures. The series of investigations performed in this work allows the conclusion that this transition occurs in the impurity band separated from the valence band. The available experimental data are indicative not only of the existence of a minimum in the density of states between the impurity and conduction bands but also of the existence of the second mobility edge in the impurity band.

2. EXPERIMENTAL

The procedure of growing multilayer structures by molecular-beam epitaxy was described in our previous work [9]. The structures contained 10–20 GaAs quantum wells 10 or 15 nm thick separated by Al$_{0.3}$Ga$_{0.7}$As barriers 25 nm thick. In the investigated samples, the
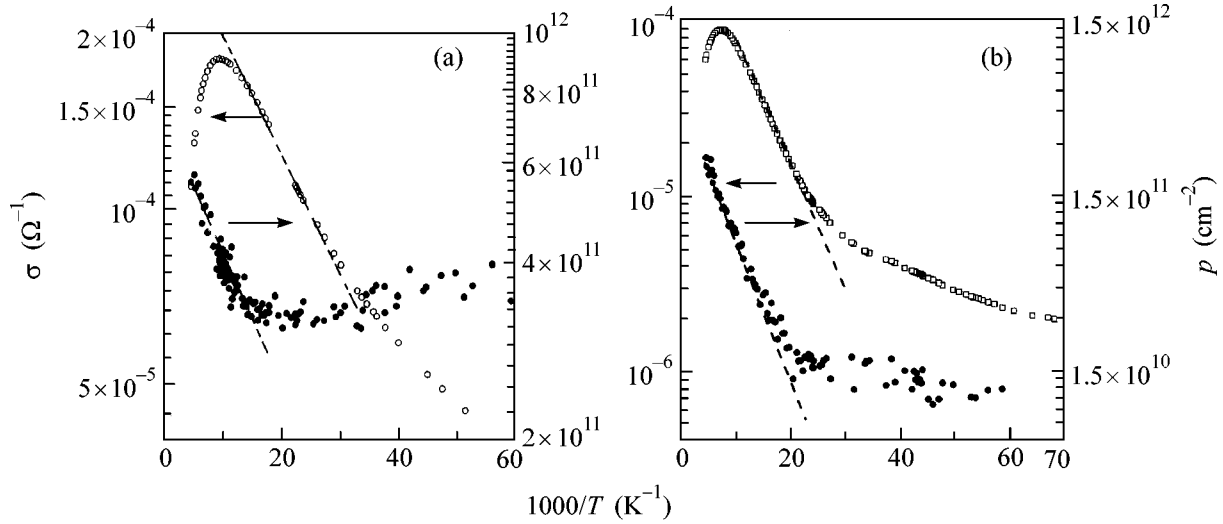
Fig. 1. Temperature dependences of the conductivity and the hole concentration: (a) for sample 1 (20 10-nm wells) with wells and barriers doped (the Be concentration is 6×10^{17} cm^{-3}) and (b) for sample 2 (10 15-nm wells) with only wells doped (the Be concentration is 10^{18} cm^{-3}).

middle area of the quantum wells 5 nm thick was doped, and the Al$_{0.3}$Ga$_{0.7}$As barriers in certain samples were doped as well (so that the middle area of the barriers 5 nm thick was doped). Beryllium was used as a p-type doping impurity. The impurity concentration was the same in both wells and barriers (the bulk concentration was varied from 5×10^{17} to 2×10^{18} at/cm^3). The critical concentration for the bulk p-type GaAs is 2×10^{18} cm^{-3}; that is, the above concentrations are of the same or somewhat lower order ($p_{300 \text{ K}} \leq p_c$). The temperature dependences of the conductivity and the hole concentration for two samples are presented in Fig. 1. Sample 1 contained A^+ centers, both wells (10 nm) and barriers were doped, and the bulk concentration of Be was 6×10^{17} cm^{-3}. Sample 2 contained A^0 centers, only wells (15 nm) were doped, and the bulk concentration of Be was 10^{18} cm^{-3}.

At temperatures higher than 100 K, an activation behavior of the Hall coefficient was observed. The activation energy was 15–13 meV for sample 2 and 5–6 meV for sample 1. A maximum or a plateau in the temperature dependence of the Hall coefficient and a rather weak variation of the conductivity in the impurity band were observed at lower temperatures. The variation of the conductivity with temperature becomes considerably weaker as compared with the exponential dependence of the samples located on the insulating side of the junction, which was observed in our previous investigation [9]. The low-temperature conductivity in sample 1 decreases according to a logarithmic law with decreasing temperature (Fig. 2). The resistivity at a low temperature (0.4 K) is 3×10^4–6×10^4 Ω, which is somewhat higher than the quantum limit $R_0^{-1} = G_0 = e^2/h$. This fact can be associated with the difference of

the sample geometry from a purely square shape. Namely, the measurements were performed with the use of four point contacts at the vertices of the square sample, so that, in measuring the conductivity at the nearest contacts, the shape of the conducting region is not square to an extent of the ratio between the sizes of the contact and the sample.

In this regime of weak localization, the conductivity of a two-dimensional system with regard for quantum corrections can be written as [3]

$$\sigma \simeq \frac{e^2}{h}\left(k_F l - \ln\frac{L_\varphi(T)}{l}\right), \qquad (1)$$

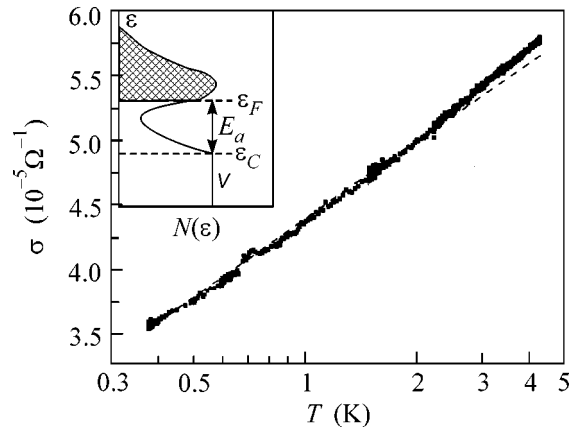**Fig. 2.** Temperature dependences of the low-temperature conductivity for sample 1. The inset shows the density of states for sample 1, where ε_F, ε_C, and E_a are the position of the Fermi level in the impurity band, the mobility edge in the valence band, and the high-temperature activation energy, respectively.
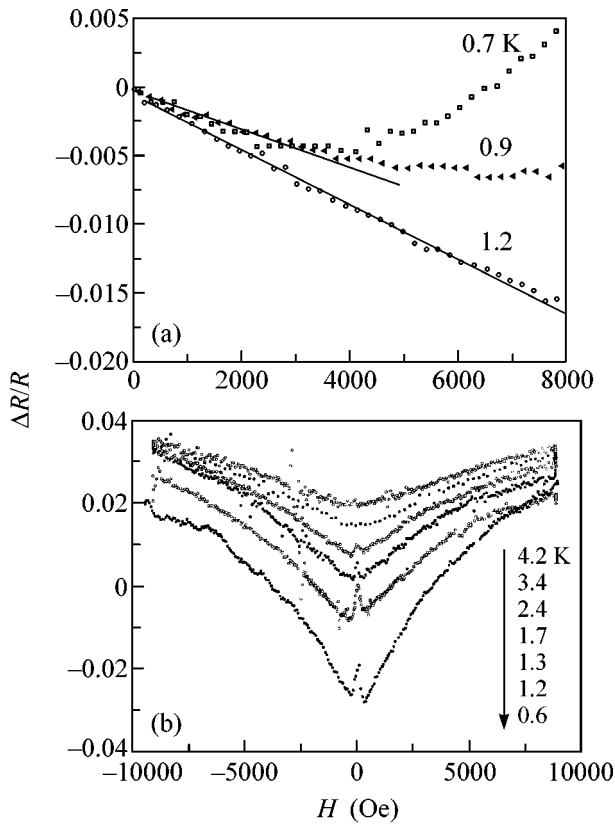
Fig. 3. MR at various temperatures for samples with A^+ centers: (a) for a sample in the regime of strong localization [9], the resistance at $T = 0.6$ K is $R = 3 \times 10^6$ Ω; (b) for sample 1 in the regime of weak localization, the resistance at $T = 0.4$ K is $R = 3 \times 10^4$ Ω.
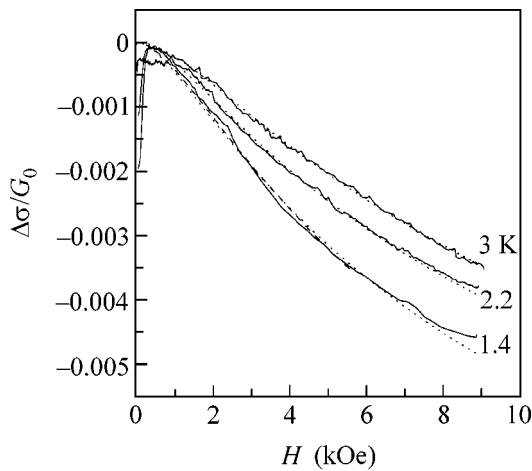

Fig. 4. Comparison of experimental MR curves for sample 1 with the theory [10]. The solid curves correspond to the experiment; the dotted curves correspond to the calculation at the following fitting parameters: $\tau_s = 3.1 \times 10^{-12}$ s (independent of temperature); dephasing time $\tau_\varphi = 4.8 \times 10^{-11}$ s (3 K), 6.3×10^{-11} s (2.2 K), and 7×10^{-11} s (1.4 K).

where L_φ is the dephasing length, which equals $L_\varphi = (D\varepsilon_F\tau/T)^{1/2}$ for the case of diffusion electron–electron collisions; k_F and ε_F are the Fermi vector and energy; and D, l, and τ are the diffusion coefficient, the mean free path length, and the momentum relaxation time, respectively.

In addition to the dependence $\sigma(T)$, differences in the behavior of the magnetoresistance (MR) in the region of low temperatures may be evidence in favor of the manifestation of the SL–WL crossover. We showed previously [9] that insulating samples are characterized by the existence of a linear negative interference MR. As the temperature decreases, this negative MR is suppressed by the quadratic positive MR associated with the fact that the localization radius decreases in a magnetic field (Fig. 3a). In the samples occurring in the regime of weak localization, the MR proves to be positive in the temperature range (0.6–3) K and depends on the magnetic field approximately as $H^{0.5}$ (Fig. 3b). This can be associated with the manifestation of weak antilocalization given spin–orbit interaction. Figure 4 presents a comparison of experimental data and the calculated dependences $\sigma(H)$ obtained from the corresponding theoretical models [10]. It is evident that good agreement with the theory is observed for the entire region of magnetic fields and temperatures at the following fitting parameters: spin relaxation time $\tau_s = 3.1 \times 10^{-12}$ s (independent of temperature) and dephasing time $\tau_\varphi = 4.8 \times 10^{-11}$ s (3 K), 6.3×10^{-11} s (2.2 K), and 7×10^{-11} s (1.4 K). The fact that weak antilocalization is observed up to fields of 1 T is associated with very small values of the parameter k_Fl corresponding to the vicinity of the SL–WL transition. A negative MR peak is evident in the region of very low fields and low temperatures. The temperature at which this peak starts to emerge correlates with the superconducting transition temperature for the indium contact. Note, however, that the suppression of the superconducting state by a magnetic field leads to an increase in the system conductivity (rather than resistivity, as might be expected from the simplest considerations). We hope to investigate this phenomenon more comprehensively in a subsequent work.

3. DISCUSSION

The SL–WL transition in GaAs/AlGaAs structures was observed experimentally in [7]. The transition occurred as the carrier concentration was varied with the use of a gate. It was manifested as a change in the temperature dependence from an activation form to a logarithmic form. An analogous behavior was also observed in ultrathin Cu/Ge, Ag/Ge, and Au/Ge films as the concentration of the noble metals was varied [8]. In the SL–WL transition, the MR sign changed from negative to positive. In this case, the low-temperature conductivity was close to $G_0 = e^2/h$.

Our GaAs/Al$_{0.3}$Ga$_{0.7}$As structures with wells whose center is heavily doped are distinct from clean structures studied previously [3], because the localized states in these structures are determined by the dopant and their parameters are known. In particular, it is known that, as the doping level increases, an impurity band forms. This band determines the specific features of transport phenomena at low temperatures. In the two-dimensional case, the lower and, especially, upper Hubbard bands are located lower in energy than those for bulk materials. As the impurity concentration increases, an SL–WL transition occurs in the split-off impurity band and the concept of the Hubbard energy loses its meaning for delocalized states. Moreover, even for the localized states that are close in energy to the delocalized ones, the Hubbard energy is very small so that these states also prove to be doubly occupied [5, 6]. The logarithmic temperature dependence of the conductivity and the transition from the negative (interference) to positive (associated with weak antilocalization) magnetoresistance serve as evidence for the onset of the WL regime.

The set of studies performed in this work allows the conclusion that the SL–WL crossover indicated above occurs in the impurity band separated from the valence band (see the inset in Fig. 2). Actually, as is evident in Fig. 1, a pronounced exponential growth of the conductivity is observed with increasing temperature at temperatures higher than 30 K (with an activation energy of 6 and 13 meV for samples 1 and 2, respectively). At somewhat higher temperatures, the Hall concentration also exhibits an exponential growth. This behavior can be explained by the contribution from two bands with metallic conduction (namely, the lower one originating from the impurity band, and the upper, from the valence band) in combination with the suggestion that the mobility in the valence band is appreciably higher than the mobility in the impurity band. The minimum in the Hall concentration $n = e/cR$ at temperatures of about 50 K is explained by a combination of contributions from two bands indicated above (see, for example, [11]). Actually, the Hall coefficient R for the two-band model is expressed through partial mobilities μ and concentrations n as

$$R = (e/c)\frac{\mu_1^2 p_1 + \mu_2^2 p_2}{(\mu_1 p_1 + \mu_2)^2}, \qquad (2)$$

so that, when $\mu_1 \gg \mu_2$ in the region of concentrations $(\mu_2/\mu_1)p_2 > p_1 > (\mu_2/\mu_1)^2 p_2$, we have $R \simeq (e/c)(p_1\mu_1^2)(p_2^2\mu_2^2)$. Hence, R reaches a maximum at $p_1 \sim p_2(\mu_2/\mu_1)$.

Thus, the observed behavior, from our point of view, indicates that the delocalized states manifested experimentally are located rather deep in the impurity band, whereas the states in a certain energy band located closer to the conduction band bottom are localized.

Experimental estimates of the activation energy testify that the above band is rather broad.

Because the spectrum of delocalized wave functions in the impurity band can differ from the corresponding spectrum in the valence band, it is of interest to evaluate the effective mass of holes in the impurity band. Note that carriers at low temperatures are entirely concentrated in the impurity band and are degenerate. The relation of the Fermi energy with the concentration can be expressed as

$$\varepsilon_F = p\pi\hbar^2/m. \qquad (3)$$

To estimate m, we will use the circumstance that the transport relaxation time τ at comparatively high temperatures is determined by temperature, whereas it is determined by the Fermi energy in the limit of low temperatures. Assuming that, in both cases, we deal with scattering by charged impurities and $\tau \propto \varepsilon$ (see, for example, [12]), it may be concluded that the ratio of the mobilities at $T = 50$ K in the valence band to the mobility in the impurity band is

$$\frac{\mu_{ib}(T \longrightarrow 0)}{\mu_b(T = 50 \text{ K})} \sim \frac{\varepsilon_F}{50 \text{ K}}\frac{m_b}{m_{ib}}. \qquad (4)$$

Unfortunately, the two-band character of the Hall effect prevents the mobility in the valence band from being estimated directly. Therefore, we will estimate it indirectly using the following estimate for the concentration p_b in the valence band: $p_b(50 \text{ K}) \sim p_{i,b}(T = 0)e^{-E_a/T}(m_b/m_{i,b})$, where E_a is the activation energy. Hence, it follows that

$$\frac{\mu_{ib}(T \longrightarrow 0)}{\mu_b(T = 50 \text{ K})} \sim \frac{\sigma_{ib}(T \longrightarrow 0)e^{-E_a/T}m_b}{\sigma_b(T = 50 \text{ K})m_{ib}}.$$

Using the above estimates and taking into account that the contributions to the conductivities at $T = 50$ K from both bands are approximately equal (which follows from the minimum of the Hall concentration), we finally find that $m_{ib} \sim 10^{-27}$ g. Because $m_b \sim 0.3 \times 10^{-27}$ g, the mass in the impurity band is approximately three times larger than in the valence band. It is evident that the above estimate is rather crude; however, both the activation dependence of the conductivity and the behavior of the Hall concentration point to a notable difference between the mobilities in the conduction and impurity bands, which is indicative of corresponding differences in the effective mass. Note that an electron mass substantially exceeding (by a factor of 5) the mass in the conduction band was observed in 3D GaAs [2] at impurity concentrations close to critical. This mass was assigned to the metallic phase in the impurity band.

Note that, up to this point, we discussed results obtained for samples in which both wells and barriers were doped. Correspondingly, transport in the impurity band and in the hopping regime was conducted through doubly occupied states of the upper Hubbard band. The

localization radius of a state in the upper Hubbard band exceeds the localization radius of an isolated acceptor by a factor of approximately 3 even at low impurity concentrations [9]. It is due to this circumstance that the regime of weak localization is observed at impurity concentrations substantially lower than those corresponding to the Mott criterion for the lower Hubbard band.

The samples in which only wells were doped (in which only the lower Hubbard band is filled in equilibrium) also exhibited a crossover from strong to weak localization, though, at a markedly higher doping level. In this case, a weak logarithmic temperature dependence of the resistivity and a positive magnetoresistance associated with antilocalization were observed at $T < 10$ K. The results for one such sample in the region of high temperatures are presented in Fig. 1b. It is seen that the activation behavior of both the conductivity and the Hall concentration in this sample is even more pronounced than in the sample with the filling of the upper Hubbard band. This is due to a considerably higher ionization energy. However, a quantitative analysis of the results for such samples reveals certain discrepancies with the simple model assuming equal contributions from all quantum wells. In our opinion, this can be attributed either to the nonuniformity of the samples or to the fact that individual wells differ in their doping levels. Then, weak localization in one of the wells occurs under conditions when the other ones still reside in the limit of strong localization. Such a behavior can be caused precisely by the high doping level of the corresponding samples.

In summary, it may be stated that we observed a crossover from strong to weak localization in two-dimensional modulation-doped GaAs/Al$_{0.3}$Ga$_{0.7}$As structures with increasing dopant concentration. The character of the temperature dependences of the conductivity and the Hall concentration of carriers allows the conclusion that the crossover occurs in the impurity band separated from the valence band.

REFERENCES

1. J. B. Choi, S. Liu, and H. D. Drew, Phys. Rev. B **43**, 4046 (1991).

2. I. S. Liu, H. D. Drew, A. Illiades, and S. Hadjipanteli, Phys. Rev. B **45**, 1155 (1992).

3. E. Abrahams, S. V. Kravchenko, and M. P. Sarachik, Rev. Mod. Phys. **73**, 251 (2001).

4. B. L. Altshuler and D. L. Maslov, Phys. Rev. Lett. **82**, 145 (1999).

5. V. I. Kozuba and N. V. Agrinskaya, Phys. Rev. B **64**, 245103 (2001).

6. H. Kamimura, Philos. Mag. **42**, 763 (1980).

7. F. V. Van Keuls, H. Mathur, H. W. Jiang, and A. L. Dahm, Phys. Rev. B **56**, 13263 (1997).

8. Shih-Ying Hsu and J. M. Valles, Phys. Rev. Lett. **74**, 2331 (1995).

9. N. V. Agrinskaya, V. I. Kozub, Yu. L. Ivanov, *et al.*, Zh. Éksp. Teor. Fiz. **120**, 480 (2001) [JETP **93**, 424 (2001)].

10. W. Knap, G. E. Pikus, F. G. Pikus, *et al.*, Phys. Rev. B **53**, 3912 (1996).

11. O. V. Emel'yanenko, T. S. Lagunova, and D. V. Nasledov, Fiz. Tverd. Tela (Leningrad) **7**, 1315 (1965) [Sov. Phys. Solid State **7**, 1063 (1965)].

12. S. Das Sarma and E. H. Hwang, Phys. Rev. Lett. **83**, 164 (1999).

Translated by A. Bagatur'yants

Thermoelectric Properties of the Trigonal and Orthorhombic Modifications of Zinc Telluride

S. V. Ovsyannikov* and V. V. Shchennikov

Institute of Metal Physics, Ural Division, Russian Academy of Sciences, Yekaterinburg, 620219 Russia
*e-mail: sergey_v_o@imp.uran.ru
Received May 20, 2004

Thermoelectric measurements are performed to study the phase transformations occurring in ZnTe under high pressure. It is shown that the thermoelectric power S of the cinnabar trigonal phase corresponds to a semiconductor with a hole-type conduction. In the *Cmcm* orthorhombic phase, the value of $S \approx +10$ µV/K and the sign of the thermoelectric power testify to the metallic hole-type conduction, as in the high-pressure phases of other Group II chalcogenides (HgSe, HgTe, CdTe) with similar crystal lattices. In the transition region between the trigonal and orthorhombic phases, the pressure dependence of the thermoelectric power is found to exhibit an anomaly (a sharp dip), which leads to a change in the sign of S under decreasing pressure. This feature may presumably be related to the formation of the intermediate phase with the NaCl structure, which has an electron-type conduction in other zinc and cadmium chalcogenides.© 2004 MAIK "Nauka/Interperiodica".

PACS numbers: 72.20.Pa; 61.50.Ks; 81.40.Vw

Owing to the technological and scientific significance of Group II and VI semiconductor compounds, studies of their electronic and crystal structures are topical to this day [1–9]. Phenomena of major interest are the pressure-induced polymorphic transformations accompanied by sharp changes in the crystal lattice and electronic structure. In most of the II–VI materials, semiconductor-to-metal transformations are observed [5, 6, 10–25].

With the development of effective methods for studying the crystal lattice under high pressure, including X-ray absorption spectroscopy [12, 13], X-ray diffraction studies, the method of angular diffraction of synchrotron radiation using image-plate area detectors [4, 6], etc., and also with the progress in calculating the electronic structure and the total lattice energy [1–3], it has become possible to refine the structures occurring under pressure in mercury, cadmium, and zinc chalcogenides: HgX, CdX, and ZnX (where X represents Te, Se, S, or O) [4, 6]. It was found that the d states ignored in the previous studies play a significant role in the determination of the structural and electronic properties of II–VI compounds. Therefore, recent calculations [1–3] take into account the Zn $3d$-orbitals and the Te $4d$-orbitals, which drastically increases the number of the basis wave functions and complicates the calculations [1–3].

Thermoelectric studies of different structural modifications of II–VI compounds under ultrahigh pressure [18–21, 25, 26] have made it possible to refine their electronic structure and complement the frequently contradictory data on the optical absorption [5, 24] and electrical resistance [11, 24]. In particular, the measurements of the thermoelectric power [26, 27] showed that, among the "metallic" high-pressure phases, some have charge carrier (hole) concentrations corresponding to the metallic conduction, while the others are actually semiconductor phases, which, despite the positive temperature coefficient of resistance, retain a relatively large energy gap $E_g > 1$ eV [5, 24]. Zinc telluride ZnTe proved to be the least-studied Group II chalcogenide, because its thermoelectric properties have not been investigated under pressures higher than 20 GPa. In the pressure interval below 20 GPa, three structural modifications are realized in ZnTe: (i) cubic modification (sphalerite, $F\bar{4}3m$) below 8.9–9.5 GPa, (ii) trigonal modification (cinnabar, $P3_121$) above 8.9–9.5 GPa, and (iii) orthorhombic modification (*Cmcm*) above 11.5–13 GPa [1–10, 12–15]. The cinnabar structure in ZnTe is completely different from that formed in mercury chalcogenides, where it consists of isolated helical chains [4, 6, 14]: in ZnTe, it retains the coordination number $z = 4$, as in the initial cubic phase [14]. The sequence of crystal-lattice transformations observed in ZnTe under pressure is different from that observed for other zinc chalcogenides, ZnSe and ZnS, in which the $F\bar{4}3m$ cubic phase and the *Cmcm* orthorhombic phase are separated by a stable phase with the *Fm3m* rocksalt structure [4–6, 15]. Recent Raman scattering measurements in ZnTe revealed an unknown intermediate phase in a pressure interval of 12.2–13.7 GPa [7]. This phase was not observed in structural experiments [4, 6], which, according to [7], can be explained by the fact that the stability region of the phase in question is narrower than the pressure step (~0.5–1 GPa) in the pres-
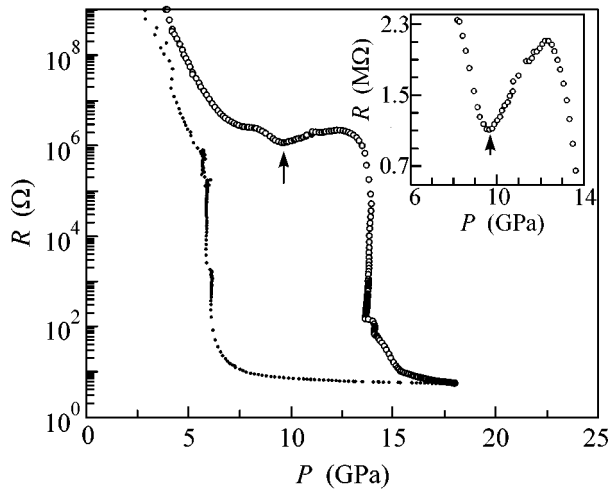
Fig. 1. Resistance R vs. pressure P for a ZnTe single crystal at $T = 295$ K. The smaller dots show the dependence observed under decreasing pressure. The inset shows part of the dependence $R(P)$ in the region of the sphalerite–cinnabar transition (indicated by the arrow) on the linear scale.

sure measurements [4, 6] and also by the difference in the initial samples: powder polycrystals in diffraction experiments [4, 6] and single crystals in optical experiments [7]. The observation of the intermediate phase by the diffraction method is also hindered by the presence of the mixture of phases in the transition region: the initial cubic and trigonal phases within 9.5–11 GPa [14] and the trigonal and orthorhombic phases within 11.5–15.7 GPa [8] and 12–13.7 GPa [7].

The purpose of this study is, first, to investigate the phase transformations in ZnTe by the thermoelectric power measurements, which were found to be rather effective in studying the other II–VI compounds [18–21, 25–27], and, second, to determine the sign and magnitude of the thermoelectric power in the trigonal and orthorhombic high-pressure phases of ZnTe. Unlike other properties, the thermoelectric power is sensitive to the changes in sign of the dominant charge carriers that are often observed at phase transformations [18, 19, 25–30].

The resistance R and the thermoelectric power S of the ZnTe samples pressurized to 20 GPa were measured in a high-pressure cell, which was made from synthetic diamonds characterized by a high electrical conductivity [18, 19, 25–30]. The samples were undoped ZnTe single crystals, red in color, with the dimensions $\sim$0.2 × 0.2 × 0.1 mm. They were placed in a hole 0.25 mm in diameter with a compressible spacer made of lithographic limestone. The diamond anvils served as electric leads. Measurements with a reference sample ("OSCh" lead, whose thermoelectric power is close to zero: $S \approx -1.27$ μV/K [27–31]) were used to take into account the error introduced to the thermoelectric power. To produce a temperature gradient, one of the anvils was heated. The thermoelectric power was mea-

sured in two ways: from the dependence of the thermoelectric signal on the temperature difference at a fixed pressure and by applying a continuously varying pressure at a fixed temperature difference. We used an automated system, which simultaneously recorded all parameters of the experiment: pressure (force), anvil displacements (compression of the spacer and the sample), temperature difference, electric signal from the sample, etc. [27–31]. The pressure was measured with an accuracy of 10% from the calibration dependence plotted according to the known phase transitions in the reference substances: CdTe, ZnSe, ZnS, and others [10, 18, 19]. The errors in the resistance and the thermoelectric power determination did not exceed 5 and 20%, respectively. For comparison with ZnTe, we measured the thermoelectric power in the high-pressure phases of ZnS and ZnSe; the resulting data correspond to the data reported in [18].

The pressure dependence of the ZnTe resistance $R(P)$ (Fig. 1) agrees well with the data reported by other authors, despite the difference in the experimental conditions, namely, in the type of high-pressure cell, the sample geometry, the pressure-transmitting medium, and the method of pressure determination [10, 11, 16]. The steep drop in $R(P)$ at 3–5 GPa, which was also observed in [10], is associated with the formation of point defects [13]. The dependence $R(P)$ exhibits a local minimum near 9 GPa, after which the resistance begins to grow, and above $\sim$ 13 GPa R decreases by $\sim$6 orders of magnitude (Fig. 1). According to the X-ray data [4–6, 10, 12, 13], the first resistance anomaly is associated with the structural transition to the cinnabar trigonal phase, and the second anomaly, with the transition to the *Cmcm* orthorhombic phase. The thermoelectric power S was measured in the pressure interval where the resistance of the samples was below 10^6 Ω, i.e., in the stability region of the trigonal and orthorhombic phases (see Fig. 1). In the $S(P)$ dependence, the phase transition from trigonal to orthorhombic phase shows up as a sharp drop in the magnitude of the thermoelectric power by a factor of $\sim$40–50 (Fig. 2). The thermoelectric power data testify to the hole-type conduction in both the cinnabar trigonal phase and the orthorhombic phase of ZnTe (Fig. 2). The relatively high value of $S \approx 400$ μV/K testifies to the semiconductor nature of conduction in the trigonal phase, in which the energy gap obtained from the optical absorption data is $E_g = 2.5$ eV at 9.5 GPa and weakly decreases with pressure P [17]. In the orthorhombic lattice, S takes on values typical of metals: $\sim$10μV/K, which agrees well with the calculated value ($\sim$1 eV) of the overlap between the conduction and valence bands [2, 3] and with the high charge-carrier concentration (1.5 × 10^2 cm^{-3}) estimated from the optical reflection data [5]. Close positive values of S were obtained for ZnTe under pressures of about 20 GPa in [32], but the authors gave no data for pressures below 20 GPa that confirm the presence of the first and second phase transformations in the sample. The thermoelectric power of the metallic
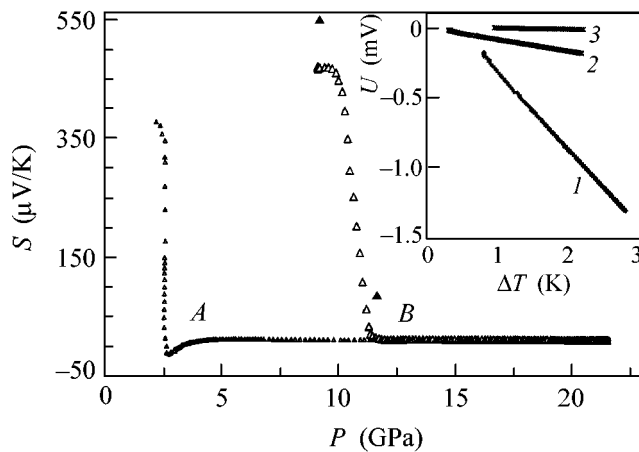
Fig. 2. Thermoelectric power S vs. pressure P for a ZnTe single crystal at $T = 295$ K under increasing and decreasing pressure (shown by dots). The full dots refer to the determination of S with a varying temperature difference, and the empty dots, to the determination at a fixed temperature difference. The inset shows the dependences of the thermoelectric signal on the temperature difference, which were used to determine the values of the thermoelectric power at fixed pressure values: (*1*) 9.2, (*2*) 11.7, and (*3*) 20.5 GPa.
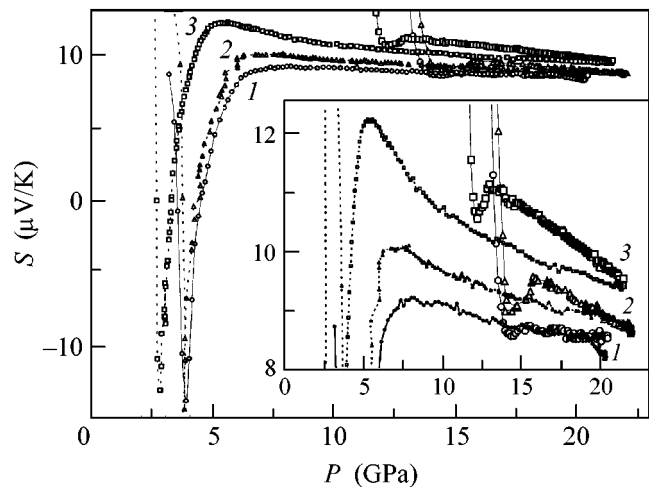

Fig. 3. Dips in the pressure dependences of thermoelectric power S for ZnTe at $T = 295$ K. The curves are obtained in sequential cycles of pressure decrease ((*1–3*) portion of curve A from Fig. 2). The inset shows the same dips in the region of trigonal-to-orthorhombic phase transition in sequential cycles of pressure increase ((*1–3*) portion of curve B from Fig. 2).

high-pressure phase of ZnTe has the same sign and magnitude as observed for the metallic high-pressure phases of CdTe, HgTe, and HgSe [18, 20] with the *Cmcm* orthorhombic structure [4–6, 15], whereas, in the "metallic" high-pressure phases of ZnS and ZnSe with the rocksalt structure, the thermoelectric power is much greater in magnitude and opposite in sign [18].

In the region of transition from the semiconductor to metallic phase, the curve $S(P)$ exhibits a dip (Figs. 2, 3). This feature was reproduced for all samples in several cycles of pressure variations and was found to be more pronounced under decreasing pressure P, in which case even a change in sign of the thermoelectric power was observed (Fig. 3). The latter fact suggests that the charge carriers of opposite sign, i.e., electrons, come into play. This explains the absence of any anomalies in the behavior of conductivity $\sigma = 1/\rho$ [10, 11], where, unlike the thermoelectric power ($S = (\sigma_n/\sigma)S_n + (\sigma_p/\sigma)S_p)$), the partial contributions of electrons σ_n and holes σ_p are of the same sign ($\sigma = \sigma_n + \sigma_p$) [33]. The change in sign of the thermoelectric power indicates that the electron contribution predominates as the pressure decreases (Fig. 3).

The negative contribution to the thermoelectric power can be attributed to the intermediate high-pressure phase that was observed in the experiments with Raman light scattering [7]. In mercury and cadmium chalcogenides, including HgTe, HgSe, and CdTe, and in ZnSe (under decreasing pressure), the *Fm3m* rocksalt lattice is realized between the cinnabar structure and the *Cmcm* orthorhombic phase [4, 6, 15]. In ZnTe, the rocksalt structure was earlier observed only at elevated temperatures [9]. The appearance of the negative

contribution to the thermoelectric power in the phase-transition region (Fig. 3) is an argument in favor of the possible stability of the intermediate phase with the rocksalt structure, which, in other zinc chalcogenides (as well as in cadmium chalcogenides), is known to have negative values of the thermoelectric power [18, 27]. Judging from the behavior of the thermoelectric power (Fig. 3), this phase should be sought under a decreasing pressure.

REFERENCES

1. R. Franco, P. Mori-Sanchez, J. Mi Recio, and R. Pandey, Phys. Rev. **68**, 195208 (2003).
2. G.-D. Lee and J. Ihm, Phys. Rev. **53**, R7622 (1996).
3. M. Cote, O. Zakharov, A. Rubio, and M. L. Cohen, Phys. Rev. **55**, 13025 (1997).
4. R. J. Nelmes and M. I. McMahon, Semicond. Semimet. **54**, 145 (1998).
5. A. R. Goni and K. Syassen, Semicond. Semimet. **54**, 247 (1998).
6. A. Mujica, A. Rubio, A. Munoz, and R. J. Needs, Rev. Mod. Phys. **75**, 863 (2003).
7. J. Camacho, I. Loa, A. Cantarero, and K. Syassen, J. Phys.: Condens. Matter **14**, 739 (2002).
8. R. J. Nelmes, M. I. McMahon, N. G. Wright, and D. R. Allan, Phys. Rev. Lett. **73**, 1805 (1994).
9. O. Shimomura, W. Utsumi, T. Urakawa, *et al.*, Rev. High Pressure Sci. Technol. **6**, 207 (1997).
10. A. Ohtani, M. Motobayashi, and A. Onodera, Phys. Lett. A **75**, 435 (1980).

11. G. A. Samara and H. G. Drickamer, J. Phys. Chem. Solids **23**, 457 (1962).

12. A. San Miguel, A. Polian, J. P. Itie, *et al.*, High Pressure Res. **10**, 412 (1992).

13. A. San Miguel, A. Polian, M. Ganthier, and J. P. Itie, Phys. Rev. **48**, 8683 (1993).

14. A. San Miguel, A. Polian, and J. P. Itie, J. Phys. Chem. Solids **56**, 555 (1995).

15. E. Yu. Tonkov, *Compounds and Alloys under High Pressure* (Gordon and Breach, Amsterdam, 1998).

16. S. Endo, A. Yoneda, M. Ishikawa, *et al.*, J. Phys. Soc. Jpn. **51**, 138 (1982).

17. K. Strossner, S. Ves, C. K. Kim, and M. Cardona, Solid State Commun. **61**, 275 (1987).

18. V. V. Shchennikov, Rasplavy **2**, 33 (1988).

19. I. M. Tsidil'kovskiĭ, V. V. Shchennikov, and N. G. Gluzman, Fiz. Tverd. Tela (Leningrad) **27**, 439 (1985) [Sov. Phys. Solid State **27**, 269 (1985)].

20. I. M. Tsidil'kovskiĭ, V. V. Shchennikov, and N. G. Gluzman, Fiz. Tekh. Poluprovodn. (Leningrad) **19**, 1464 (1985) [Sov. Phys. Semicond. **19**, 901 (1985)].

21. V. V. Shchennikov, Fiz. Tverd. Tela (St. Petersburg) **35**, 783 (1993) [Phys. Solid State **35**, 401 (1993)].

22. N. G. Gluzman and V. V. Shchennikov, Fiz. Tverd. Tela (Leningrad) **21**, 3192 (1979) [Sov. Phys. Solid State **21**, 1844 (1979)].

23. V. V. Shchennikov and N. G. Gluzman, Fiz. Tverd. Tela (Leningrad) **23**, 3091 (1981) [Sov. Phys. Solid State **23**, 1800 (1981)].

24. *Solids Under Pressure*, Ed. by W. Paul and D. Warschauer (McGraw-Hill, New York, 1963; Mir, Moscow, 1966).

25. I. M. Tsidil'kovskiĭ, V. V. Shchennikov, and N. G. Gluzman, Fiz. Tekh. Poluprovodn. (Leningrad) **17**, 958 (1983) [Sov. Phys. Semicond. **17**, 604 (1983)].

26. V. V. Shchennikov, Defect Diffus. Forum **208–209**, 275 (2002).

27. S. V. Ovsyannikov and V. V. Shchennikov, Physica (Amsterdam) **344**, 190 (2004).

28. V. V. Shchennikov and S. V. Ovsyannikov, Pis'ma Zh. Éksp. Teor. Fiz. **74**, 546 (2001) [JETP Lett. **74**, 486 (2001)].

29. V. V. Shchennikov and S. V. Ovsyannikov, Pis'ma Zh. Éksp. Teor. Fiz. **77**, 93 (2003) [JETP Lett. **77**, 88 (2003)].

30. S. V. Ovsyannikov, V. V. Shchennikov, Y. S. Ponosov, *et al.*, J. Phys. D: Appl. Phys. **37**, 1151 (2004).

31. V. V. Shchennikov, S. V. Ovsyannikov, and A. Yu. Derevskov, Fiz. Tverd. Tela (St. Petersburg) **44**, 1762 (2002) [Phys. Solid State **44**, 1845 (2002)].

32. O. A. Ignatchenko and A. N. Babushkin, Fiz. Tverd. Tela (St. Petersburg) **36**, 3587 (1994) [Phys. Solid State **36**, 1909 (1994)].

33. K. Seeger, *Semiconductor Physics* (Springer, Wien, 1973; Mir, Moscow, 1977).

Translated by E. Golyamina

Effective Hamiltonian and Properties of the Normal and Superconducting Phases of *n*-Type Cuprates

M. M. Korshunov[1,*], S. G. Ovchinnikov[1], and A. V. Sherman[2]

[1] *Kirenskiĭ Institute of Physics, Siberian Division, Russian Academy of Sciences, Akademgorodok, Krasnoyarsk, 660036 Russia*
*e-mail: mkor@iph.krasn.ru
[2] *Institute of Physics, University of Tartu, Tartu, 51014 Estonia*
Received March 11, 2004; in final form, May 24, 2004

An effective low-energy Hamiltonian is derived from a microscopic multiband *p–d* model in the regime of strong electron correlations. The parameters of the *p–d* model are determined by comparison with the ARPES data for undoped Nd_2CuO_4. The Hamiltonian is the *t–J** model in which hopping and exchange slowly decay with distance and are taken into account up to the fifth coordination sphere. The quasiparticle band structure is calculated as a function of the doping concentration with regard to short-range magnetic order, and the superconductivity theory with the spin-fluctuation pairing mechanism is constructed. Assuming that the parameters of the model do not depend on the doping level, we obtained quantitative agreement with the properties observed experimentally for the normal and superconducting phases without introducing fitting parameters. © 2004 MAIK "Nauka/Interperiodica".

PACS numbers: 74.20.Mn; 74.72.Jt; 74.25.-q

1. There exist two types of high-T_c superconductors: the *p* type, that is, hole-doped cuprates ($La_{2-x}Sr_xCuO_4$ (LSCO), etc.) and the *n* type, that is, electron-doped cuprates ($Nd_{2-x}Ce_xCuO_4$ (NCCO), $Pr_{2-x}Ce_xCuO_4$ (PCCO), etc.). Though cuprates of these two types contain the base element of high-T_c superconductors, namely, the CuO_2 plane, their properties differ substantially (see, for example, [1, 2]). In this work, a quantitative theory has been constructed to describe the dependence of the properties of the normal phase and the critical temperature $T_c(x)$ on the electron concentration *x* in *n*-type superconductors. The theory contains no fitting parameters. The effective Hamiltonian in the form of the *t–J** model has been derived from the microscopic multiband *p–d* model in the regime of strong electron correlations (SECs). The parameters of the model have been determined from experimental data for undoped Nd_2CuO_4. The spin-fluctuation mechanism of superconductivity in the *t–J* model has long been known. However, details of the effective Hamiltonian such as the slow decrease of interatomic hopings and exchange interaction with distance (five coordination spheres have been taken into account) and the occurrence of weakly correlated hopings (three-center interactions, whose importance for determining T_c was noted in [3]) have proved to be of fundamental importance in obtaining quantitative agreement for $T_c(x)$ and for the properties of the normal phase. Taking into account short-range antiferromagnetic (AFM) order has also been found to be critical for determining the quasiparticle dispersion law, leading to the appearance of additional Van Hove singularities. Agreement with experimental data for the electronic structure of the normal phase and for $T_c(x)$ has been obtained only with allowance made simultaneously for all these details.

As for the symmetry of the order parameter, recent experimental data (phase-sensitive experiments [4] and resistance measurements in magnetic fields [5] in NCCO, measurements of the penetration depth in PCCO [6, 7], and angular-resolved photoemission spectroscopy (ARPES) measurements [8]) point to the *d* type of the order parameter (most likely, $d_{x^2-y^2}$). Therefore, we will further investigate the superconducting state only with the $d_{x^2-y^2}$ symmetry type.

2. The multiband *p–d* model [9] is an adequate model for the description of high-T_c superconductivity in cuprates [9]. The use of this model with strong electron correlations taken into account within the framework of the generalized tight-binding method made it possible to achieve quantitative agreement with the ARPES data for undoped LSCO [10–12], to describe the pinning of $\mu(x)$ in the *p*-type superconductors and its absence in the *n*-type superconductors [13], and to obtain an indirect optical gap in NCCO [14]. To consider the superconducting phase, an effective low-energy Hamiltonian for the multiband *p–d* model was obtained in [15] using operator perturbation theory. The effective Hamiltonian is asymmetric with respect to electron and hole doping: the conventional *t–J* model is appropriate for *p*-type systems, whereas the effective singlet–triplet model is an adequate model for *p*-type

systems with a complex band structure at the valence band top. It was shown in [3] that the inclusion of the three-center terms in the effective Hamiltonian plays a very significant part in the consideration of the super-conducting phase. With regard to the aforesaid, the effective Hamiltonian for *n*-type superconductors including three-center terms can be written using the Hubbard operators as follows:

$$H_{t-J*} = H_{t-J} + H_3,$$

$$H_{t-J} = \sum_{f,\sigma}(\varepsilon_1 - \mu)X_f^{\sigma\sigma} + \sum_{\langle f,g\rangle,\sigma} t_{fg}^{00} X_f^{\sigma 0} X_g^{0\sigma}$$

$$+ \sum_{\langle f,g\rangle} J_{fg}\left(\mathbf{S}_f\mathbf{S}_g - \frac{1}{4}n_f n_g\right), \tag{1}$$

$$H_3 = \sum_{\langle f,g,m\rangle,\sigma} \frac{t_{fm}^{0S} t_{mg}^{0S}}{E_{ct}}(X_f^{\sigma 0} X_m^{\bar\sigma\sigma} X_g^{0\bar\sigma} - X_f^{\sigma 0} X_m^{\bar\sigma\bar\sigma} X_g^{0\bar\sigma}).$$

Here, $J_{fg} = 2(t_{fg}^{0S})^2/E_{ct}$ is the exchange integral, $E_{ct} \approx 2$ eV is the charge-transfer gap (an analogue of the Hubbard term U), and t_{fg}^{NM} are the hopping integrals corresponding to the annihilation of a quasiparticle in the state M and its creation in the state N. The Hamiltonian parameters in Eq. (1) are expressed through microscopic parameters of the *p–d* model (see [16], where a set of microscopic parameters and the corresponding model parameters for *n*-type cuprates are also given). The distance dependence of the exchange and hopping integrals is known, and the subsequent calculations in this work were performed with the inclusion of all the integrals up to the fifth coordination sphere. The parameters were obtained by comparison with the ARPES data for undoped NCCO. Subsequently, they were considered fixed and independent of the doping level.

When the model given by Eq. (1) was applied to the nonmagnetic phase, the equations-of-motion method was used within the generalized Hartree–Fock approximation [17]. In this case, correlators of the $\langle X_f^{\sigma\sigma} X_g^{\sigma'\sigma'}\rangle$ and $\langle X_f^{\sigma\bar\sigma} X_g^{\bar\sigma\sigma}\rangle$ types arise. Decoupling of the Hubbard I type would lead to the following results:

$$\langle X_f^{\sigma\sigma} X_g^{\sigma'\sigma'}\rangle \longrightarrow \langle X_f^{\sigma\sigma}\rangle\langle X_g^{\sigma'\sigma'}\rangle = n_p^2,$$

$$\langle X_f^{\sigma\bar\sigma} X_g^{\bar\sigma\sigma}\rangle \longrightarrow \langle X_f^{\sigma\bar\sigma}\rangle\langle X_g^{\bar\sigma\sigma}\rangle = 0,$$

where n_p are the occupation numbers of the single-particle state. However, spin fluctuations are completely neglected in the case of such decoupling, whereas their consideration crucially affects the calculated properties of both the superconducting and normal phases (see, for example, [18, 19]). Therefore, we will use the fol-

lowing decoupling scheme that takes into account spin fluctuations beyond the Hubbard I approximation:

$$\langle X_f^{\sigma\sigma} X_g^{\sigma'\sigma'}\rangle \longrightarrow n_p^2 + \frac{\sigma}{\sigma'}\frac{1}{2}C_{fg},$$

$$\langle X_f^{\sigma\bar\sigma} X_g^{\bar\sigma\sigma}\rangle \longrightarrow C_{fg}.$$

Here, $C_{fg} = \langle X_f^{\sigma\sigma} X_g^{\bar\sigma\bar\sigma}\rangle = 2\langle S_f^z S_g^z\rangle$ are spin correlation functions.

The spin correlators C_{fg} were calculated using the two-dimensional *t–J* model of the CuO_2 plane. The self-energy equations with Green's functions constructed on Hubbard operators were obtained using the Mori formalism, which allows these functions to be represented as continuous fractions. The elements of the fractions for the electron and spin Green's functions contain correlators for close sites, and residual members of the fractions are many-particle Green's functions. The latter are approximated by decoupling corrected by the introduction of a vertex correction [20, 21]. This correction is determined from the condition that the site magnetization is zero in the paramagnetic state under consideration. This condition, the self-energy equations for the electron and spin Green's functions, and the self-consistency conditions for correlators form a closed system, which was solved by iterations at a fixed chemical potential and a fixed temperature. For small clusters and in the undoped case, the results of calculations [22, 23] are in good agreement with the data of the exact diagonalization and the Monte Carlo method. The spin correlators used in this work were obtained from the spin Green's function calculated within this self-consistent approach on a 20×20 lattice.

It was shown in [23] that the damping of quasiparticles $\Gamma_k = -\mathrm{Im}\Sigma_k(\omega = 0)$, where $\Sigma_k(\omega)$ is the self-energy part, is large in the vicinity of points $(0, 0)$ and (π, π). In the subsequent calculations, we broadened the spectral peaks in the vicinity of these points by artificially introducing Γ_k. The value of Γ_k itself was taken from [24]. It should be noted that, as calculations showed, the damping of quasiparticles introduced in this way weakly affect such integral characteristics as chemical potential $\mu(x)$ and superconducting transition temperature $T_c(x)$.

3. The dispersion curves and corresponding densities of states calculated for the paramagnetic nonsuperconducting phase are shown in Fig. 1 for the *t–J* and *t–J** models with and without regard for spin correlators. It is evident that the inclusion of three-center terms leads to a strong change at the conduction band top, that is, will have an effect at low doping levels *x*. In the AFM phase, there is a symmetry in the spectrum of the *t–J* model in the vicinity of the $(\pi/2, \pi/2)$ and $(\pi, 0)$ points (see Fig. 1). Such a symmetry does not exist in the paramagnetic phase. However, the inclusion of spin
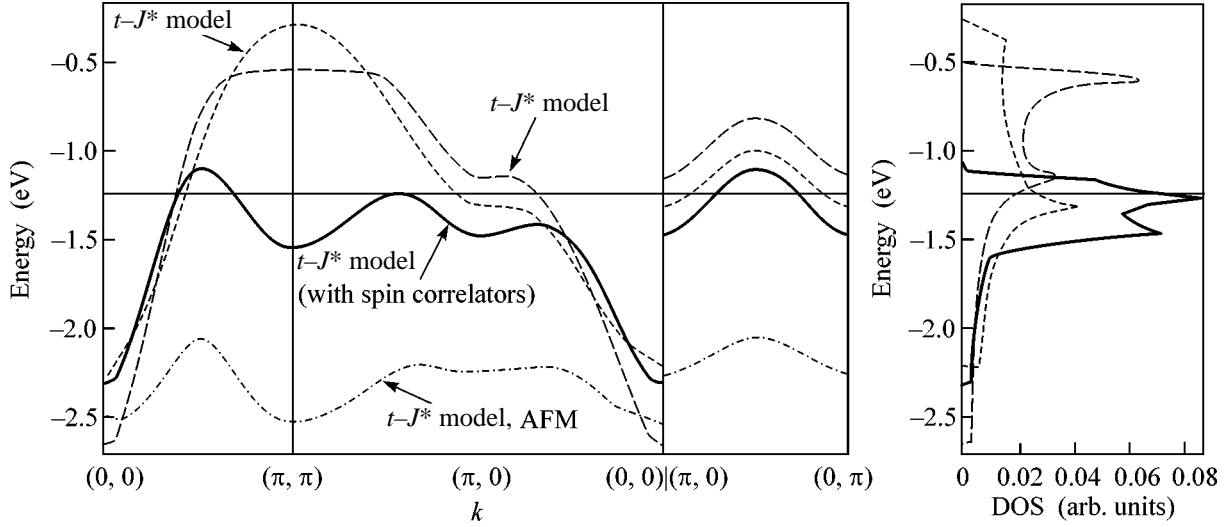
Fig. 1. Dispersion curves along the principal directions of the Brillouin zone and the density of states in the paramagnetic phase in the t–J (dotted line) and t–J^* (dashed line) models in the Hubbard I approximation and in the t–J^* model with the inclusion of spin correlators (heavy solid line). The solid horizontal line indicates the chemical potential calculated self-consistently for the latter model. The spectrum of the t–J model in the AFM phase is also shown (dash–dot line).

correlators C_{fg} results in a tendency toward the restoration of symmetry in the points mentioned above.

The dependence $\mu(x)$ is shown in Fig. 2. It is seen that the theoretical calculation is in perfect agreement with the experimental data [13] shown in the same figure; in particular, the pinning of the chemical potential is absent. The experimental [25] and calculated Fermi surfaces (black heavy shading and light solid line) for optimally doped ($x_{opt} = 0.15$) NCCO are shown in the inset in the same figure. Only one cross section is observed experimentally. Because of the occurrence of a pseudogap, spectral peaks differ in intensity along this section. In the theory considered here, there are two cross sections of the Fermi surface. However, because the damping of quasiparticles strongly depends on the momentum, the second section falls in the region of large Γ_k (this region is shown by a light solid line in the figure). This is why the second section should virtually not be observed experimentally. In light of the above, it may be argued that the calculated and experimental Fermi surfaces are in good agreement.

4. Now, when we see that the t–J^* model with the approximation considered above gives good agreement with the experimental data for the nonsuperconducting phase, we pass to the consideration of the superconducting phase. The equations for the superconducting order parameter Δ_k obtained in this work are completely similar to those given in [3, 26]; therefore, we will not write them here. Note only that, first, the coupling constant of the superconducting phase is substantially renormalized as a result of taking into account three-center terms [3]. Second, because we take into account the hopping and exchange integrals up to the fifth coor-

dination sphere, the order parameter in the case of the $d_{x^2-y^2}$ symmetry type takes the form [26]

$$\Delta_k = \sum_{m=1}^{2} \Delta_m (\cos(mk_x a) - \cos(mk_y a)). \quad (2)$$

The experimental data for NCCO and PCCO [1, 2] and the theoretical dependences of the superconducting
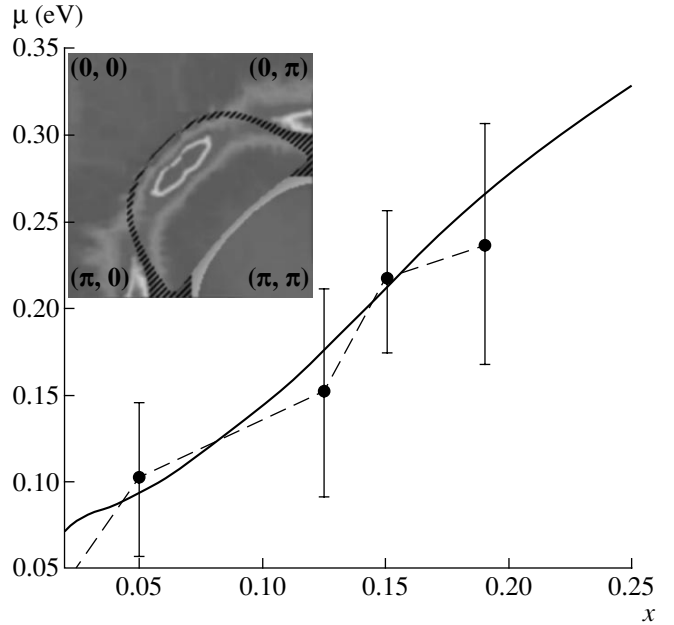

Fig. 2. Chemical potential μ as a function of the doping level x in the t–J^* model with the inclusion of spin correlators (solid line); the dashed line connects experimental points [13]. The inset shows the experimental [25] and calculated Fermi surfaces for $Nd_{1.85}Ce_{0.15}CuO_4$.
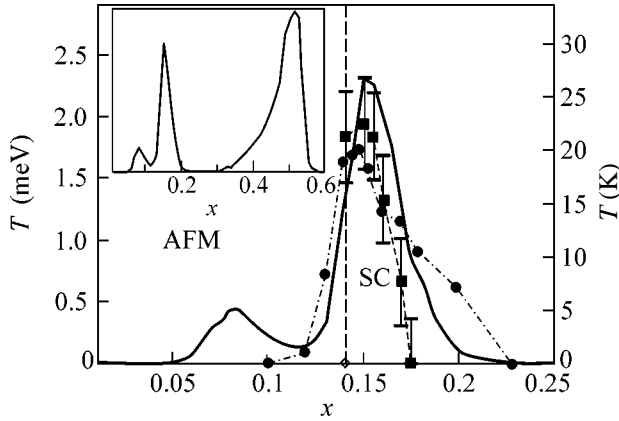
Fig. 3. Phase diagram for *n*-type cuprates: the theoretically calculated dependence $T_c(x)$ (heavy solid line) and experimental dependences $T_N(x)$ for NCCO (dashed line; the AFM and paramagnetic phases are on the left and on the right of this line), $T_c(x)$ for NCCO (dashed line with black squares), and $T_c(x)$ for PCCO (dash–dot line with black circles). The inset shows the theoretically calculated dependence $T_c(x)$ for a wider concentration range.

transition temperature $T_c(x)$ obtained in this work are compared in Fig. 3. Note that the experimental errors shown in the figure are associated with differences in sample quality rather than the accuracy of the determination of the superconducting transition temperature. The inset shows the same theoretical dependence $T_c(x)$ but for a wider concentration range. Two pronounced maxima of T_c at $x = 0.15$ and $x = 0.53$, as well as a weak maximum at $x = 0.08$, are quite evident. The additional maximum at small x in the *t–J** model with self-consistently calculated spin correlators was first obtained in [27].

The observed dependence is easily understood from simple physical considerations. In the superconductivity theory of the BCS type, there exists the relationship $T_c \propto \exp(-1/N(\varepsilon_F)V)$, where $N(\varepsilon_F)$ is the density of states at the Fermi level ε_F and V is the effective attraction. It is evident that a maximum in $T_c(x)$ will be reached when the chemical potential falls on a Van Hove singularity. In the case of neglecting spin correlators in the *t–J* model, only one Van Hove singularity associated with the flat portion of the dispersion curve at the $(\pi, 0)$ point. As is known, in this case in the nearest neighbor approximation, $x_{opt} = 0.33$, and, with regard for more than three coordination spheres, $x_{opt} = 0.53$—a maximum in $T_c(x)$ is also seen at this concentration in the inset in Fig. 3. With the inclusion of three-center terms (*t–J** model), an additional singularity appears because of the flat dispersion in the region of the (π, π) point. However, this point corresponds to the conduction band bottom. Therefore, the chemical potential falls on this singularity only at very small $x \leq 0.07$, that is, in the region where the carrier mobility is low and the short-range AFM order is still high. This

leads to the fact that the superconducting state becomes energetically unfavorable. However, in the *t–J** model with the inclusion of spin correlators, an additional singularity arises at –1.25 eV because of the saddle point at $(\pi, 0.4\pi)$ (see Fig. 1). This singularity is responsible for the maximum in $T_c(x)$ at $x \approx 0.15$. It is on this singularity that the chemical potential falls at the optimal doping level. This is the reason why the distance between the position of μ and the Van Hove singularity corresponding to the plateau in the dispersion curve at the $(\pi, 0)$ point equals $\Delta E_{VH} = 0.27$ eV. This is in good agreement with the experimental value $\propto 0.25$–0.35 eV [14, 28]. In contrast to the *n* type, ΔE_{VH} in all the *p*-type cuprates is small and less than 0.03 eV. Note that the weak maximum in $T_c(x)$ at $x = 0.08$ is associated with the shoulder (kink) in the density of states at –1.2 eV (see Fig. 1). Moreover, because the energy of the AFM phase is lower than the energy of the normal and superconducting phases, this weak maximum and the entire part of $T_c(x)$ lying in the region of $x < 0.14$ below the experimentally observed Neel temperature $T_N(x)$ will not be revealed in the experiment.

5. Thus, in the framework of an effective model for *n*-type high-T_c superconductivity and simple physical approximations based on the inclusion of spin fluctuations beyond the Hubbard I approach, we obtained quantitative agreement with such experimental data as the evolution of the chemical potential with the doping level, the Fermi surface for optimally doped NCCO, and the dependence $T_c(x)$. Though analogous results for the dependence $T_c(x)$ were obtained previously in the framework of the FLEX approximation [29], the approach used in this work is characterized by physical transparency and by the fact that it explicitly takes into account the effects of strong electron correlations, which play a very important role in high-T_c superconductors. It is shown that the physical mechanisms responsible for the concentration dependence $T_c(x)$ in *n*-type cuprates are different from those in the *p*-type cuprates. Namely, because of spin fluctuations, the system tends to restore AFM ordering. In this case, the dispersion curve is transformed in such a way that it forms flat portions in the vicinity of the $(\pi, 0.4\pi)$ point (and points symmetrical with respect to it). This leads to the formation of an additional Van Hove singularity. Because of this transformation of the density of states, an additional superconducting "dome" arises at x of order 0.15 in good agreement with experimental results. Note once again that this study was free of fitting parameters: all the parameters of the effective model are unambiguously connected with the microscopic parameters of the multiband *p–d* model. These microscopic parameters were determined in our previous studies by comparison with the ARPES data for undoped AFM cuprates.

As for the electron–phonon interaction, which was not taken into account in this work, there are indications that this interaction is weak in *n*-type high-T_c

superconductors. The first indication is that the isotope effect is almost completely absent [30]. The second indication is the absence of a kink in the $(0, 0)$–(π, π) direction [31]. This is in sharp contrast with p-type high-T_c superconductors, where the appearance of a kink is considered as the manifestation of strong electron–phonon interaction.

REFERENCES

1. G. M. Luke *et al.*, Phys. Rev. B **42**, 7981 (1990).

2. J. L. Peng *et al.*, Phys. Rev. B **55**, R6145 (1997).

3. V. V. Val'kov, T. A. Val'kova, D. M. Dzebisashvili, and S. G. Ovchinnikov, Pis'ma Zh. Éksp. Teor. Fiz. **75**, 450 (2002) [JETP Lett. **75**, 378 (2002)].

4. C. C. Tsuei and J. R. Kirtley, Phys. Rev. Lett. **85**, 182 (2000).

5. G. Kh. Panova, A. A. Shikov, N. A. Chernoplekov, *et al.*, Pis'ma Zh. Éksp. Teor. Fiz. **75**, 699 (2002) [JETP Lett. **75**, 579 (2002)].

6. J. D. Kokales *et al.*, Phys. Rev. Lett. **85**, 3696 (2000).

7. R. Prozorov *et al.*, Phys. Rev. Lett. **85**, 3700 (2000).

8. N. P. Armitage *et al.*, Phys. Rev. Lett. **86**, 1126 (2001).

9. Yu. B. Gaididei and V. M. Loktev, Phys. Status Solidi B **147**, 307 (1988).

10. V. A. Gavrichkov, S. G. Ovchinnikov, A. A. Borisov, and E. G. Goryachev, Zh. Éksp. Teor. Fiz. **118**, 422 (2000) [JETP **91**, 369 (2000)].

11. A. A. Borisov *et al.*, Zh. Éksp. Teor. Fiz. **124**, 862 (2003) [JETP **97**, 773 (2001)].

12. V. A. Gavrichkov and S. G. Ovchinnikov, Zh. Éksp. Teor. Fiz. **125**, 630 (2004) [JETP **98**, 556 (2004)].

13. N. Harima *et al.*, Phys. Rev. B **64**, 220507(R) (2001).

14. N. P. Armitage *et al.*, Phys. Rev. Lett. **88**, 257001 (2002).

15. M. M. Korshunov and S. G. Ovchinnikov, Fiz. Tverd. Tela (St. Petersburg) **43**, 399 (2001) [Phys. Solid State **43**, 416 (2001)].

16. M. M. Korshunov *et al.*, Physica C (Amsterdam) **402**, 365 (2004).

17. S. V. Tyablikov, *Methods in the Quantum Theory of Magnetism*, 2nd ed. (Nauka, Moscow, 1975; Plenum, New York, 1967).

18. N. M. Plakida and V. S. Oudovenko, Phys. Rev. B **59**, 11 949 (1999).

19. A. Sherman, Phys. Rev. B **55**, 582 (1997).

20. A. F. Barabanov and V. M. Berezovskiĭ, Zh. Éksp. Teor. Fiz. **106**, 1156 (1994) [JETP **79**, 627 (1994)].

21. J. Kondo and K. Jamaji, Prog. Theor. Phys. **47**, 807 (1972).

22. A. Sherman and M. Schreiber, Phys. Rev. B **65**, 134 520 (2002).

23. A. Sherman and M. Schreiber, Eur. Phys. J. B **32**, 203 (2003).

24. J. Schmalian *et al.*, Phys. Rev. B **54**, 4336 (1996).

25. N. P. Armitage *et al.*, Phys. Rev. Lett. **87**, 147003 (2001).

26. V. V. Val'kov and D. M. Dzebisashvili, Pis'ma Zh. Éksp. Teor. Fiz. **77**, 450 (2003) [JETP Lett. **77**, 381 (2003)].

27. V. V. Val'kov and D. M. Dzebisashvili, in *Abstracts of XXX International Winter School of Theoretical Physicists: Kourovka-2004* (Yekaterinburg–Chelyabinsk, 2004), p. 24; submitted to Zh. Éksp. Teor. Fiz.

28. D. M. King *et al.*, Phys. Rev. Lett. **70**, 3159 (1993).

29. D. Manske, I. Eremin, and K.-H. Bennemeann, Phys. Rev. B **62**, 13922 (2000).

30. M. L. Kulić, Phys. Rep. **338**, 1 (2000).

31. N. P. Armitage *et al.*, Phys. Rev. B **68**, 064517 (2003).

Translated by A. Bagatur'yants

The Proximity Effect in an Fe–Cr–V–Cr–Fe System

I. A. Garifullin[1],*, D. A. Tikhonov[1], N. N. Garif'yanov[1], M. Z. Fattakhov[1],
L. R. Tagirov[2], K. Theiz-Bröhl[3], K. Westerholt[2, 3], and H. Zabel[3]

[1]Kazan Physicotechnical Institute, Kazan Scientific Center, Russian Academy of Sciences,
Kazan, Tatarstan, 420029 Russia
*e-mail: ilgiz.garifullin@yahoo.com
[2]Kazan State University, Kazan, Tatarstan, 420008 Russia
[3]Institut für Experimentalphysik/Feskörperphysik, Runr-Universität Bochum, D-44760 Bochum, Germany
Received May 26, 2004

The proximity effect was studied in a thin-film Fe–Cr–V–Cr–Fe layered system. As the chromium layer thickness (d_{Cr}) increases at a fixed thickness of iron layers (d_{Fe}), the dependence of the superconducting transition temperature (T_c) on d_{Cr} exhibits a maximum at $d_{Cr} \simeq 40$ Å followed by a sharp decrease. Investigation of the dependence of T_c on d_{Fe} at a fixed d_{Cr} showed that the depth of penetration of the Cooper pairs into a chromium layer does not exceed 40 Å. Analysis of the results obtained suggests that, at $d_{Cr} \simeq 40$ Å, chromium layers exhibit the transition from a nonmagnetic state to an incommensurate spin density wave state. © *2004 MAIK "Nauka/Interperiodica".*

PACS numbers: 74.45.+c; 74.78.Fk; 75.70.Ak; 75.30.Fv

Below the Néel temperature ($T_N = 311$ K), metallic chromium (Cr) occurs in an antiferromagnetic state with incommensurate spin density waves (SDWs) [1]. In this state, the antiferromagnetically ordered magnetic moments are sine-modulated with a period of about 60 Å in the crystallographic [001] direction. The incommensurate SDW state in Cr is formed due to the delocalized character of electrons responsible for the magnetism.

In thin Cr films, the incommensurate SDW state depends on the magnetic and electronic properties of interfaces [2–4]. For example, iron (Fe) layers adjoining the two surfaces of a Cr interlayer induce incommensurate SDWs in the direction perpendicular to the ferromagnetic layers, so that antinodes occur at the Fe–Cr(001) interfaces [3, 5]. In contrast to this system, the SDW amplitude at the contact of Cr with vanadium (V) is strongly suppressed [5, 6]. According to the Mössbauer spectroscopy data [7, 8], the magnetic moment of Cr vanishes at the V–Cr boundary and is restored on a level comparable with the value in bulk Cr at a distance of about 40 Å from the interface.

The influence of ferromagnetism on superconductivity in thin-film heterostructures comprising superconductor (S) and ferromagnet (F) layers has been thoroughly studied and well understood for Pb–Fe [9], Nb–$Cu_{0.43}Ni_{0.57}$ [10], Nb–Ni [11], and V–Fe [12, 13] systems. However, the nature of the effect of Cr on the superconductivity in thin-film multilayer structures still remains unclear despite extensive investigations, in particular, for Pb–Cr [14], Nb–Cr [15], and V–Cr [16–22] systems. Moreover, even experimental data on the

dependence of the superconducting transition temperature (T_c) on the chromium layer thickness (d_{Cr}) are contradictory. For example, it was clearly demonstrated that an anomaly in the $T_c(d_{Cr})$ curves at $d_{Cr} \sim 40$–60 Å takes place for V–Cr(001) structures grown on single-crystal MgO(001) magnesia substrates, while being absent in V–Cr(110) samples grown on single-crystal $Al_2O_3(11\bar{2}0)$ sapphire substrates [20, 21]. At the same time, weakly pronounced anomalies in $T_c(d_{Cr})$ were reported for V–Cr(110) multilayers studied in [16, 22].

When the proximity effect is studied in systems involving superconductor–chromium interfaces, it is usually assumed that the situation is analogous to that in the superconductor–normal metal system, since the exchange field of the antiferromagnet is averaged virtually to zero over a distance comparable with the coherence length ξ_s (or with the Cooper pair size) of the superconductor. The small penetration depth of Cooper pairs in a Cr layer (as compared to that in the normal metal), is explained by introducing the mechanism of Abrikosov–Gor'kov scattering on magnetic defects [23], which breaks these pairs.

The assumption that antiferromagnetism as such does not contribute to the proximity effect could be valid if the antiferromagnetic state were formed by localized magnetic moments. However, we believe that this is not true in the case of superconductor–chromium systems, because the SDW state in Cr is due to itinerant (band) electrons, which are capable of forming a superconducting state induced by the proximity effect. Theoretical investigations of the problem of coexistence of

SDW and superconductivity (see, e.g., [24]) showed that, in the part of the Fermi surface where nesting favors the SDW order, the possibility of a superconducting gap formation is limited and the superconducting transition temperature is depressed if the temperature of transition to the SDW state is higher than the initial T_c value. Therefore, the appearance of antiferromagnetic order in Cr and the penetration of Cooper pairs from V into Cr can be considered as manifestations of the competition of two antagonistic types of collective electron ordering phenomena.

In this study, we use a combined approach to the proximity effect in the V–Cr system. Thin Cr spacers introduced between V and Fe layers in V–Fe heterostructures produce screening of the influence of a strong exchange field of Fe on Cooper pairs in the superconductor. At the same time, it is expected that possible changes in the magnetic state of Cr layers with variable thickness d_{Cr} will also influence superconductivity. Both these effects, the screening and the magnetic ordering (competing with superconductivity), can be distinguished by systematically studying the behavior of $T_c(d_{Cr})$ and $T_c(d_{Fe})$ in a thin-film Fe–Cr–V–Cr–Fe layered system.

The samples of a thin-film Fe–Cr–V–Cr–Fe structure were grown on single-crystal MgO(001) substrates by molecular beam epitaxy in an ultrahigh vacuum system with a residual pressure of 5×10^{-11} mbar. During deposition of the layer of a given material with a fixed thickness, the substrate holder bearing a series of samples was rotated so as to ensure homogeneous growth over each sample area. The series of samples with variable thicknesses of Fe and Cr layers were obtained by oblique deposition onto substrates with a length of 34 mm and a width of 5 mm. In this case, the substrate holder was not rotated and the substrate was positioned relative to the crucible so as to provide for the maximum natural gradient of deposited-layer thickness along the sample length. In order to obtain epitaxial films with improved structure, the substrates were initially covered with a 40-Å-thick Cr layer; in the final stage, the sample structures were covered by a protective 50-Å-thick Cr layer. After extraction from the vacuum chamber, long plates were cut so as to obtain a series of samples with different thicknesses of iron (d_{Fe}) or chromium (d_{Cr}) layers. We prepared and studied four series of sample structures with the layer thicknesses presented in the table. In series 1, d_{Cr} was varied at a fixed $d_{Fe} = 50$ Å. In series 2–4, d_{Cr} was fixed and d_{Fe} was varied. The thickness of the V layer was 300 Å in all samples. This value was selected upon analysis of the data available on the proximity effect in V–Fe [13] and V–Cr [16–22] systems, which showed that maximum sensitivity of T_c in the multilayer structures with respect to the thickness of Fe and V layers was observed for the samples with $d_V = 300$ Å.

The thicknesses of component layers were evaluated using computer-aided fitting of the small-angle

Layer thicknesses in thin-film Fe–Cr–V–Cr–Fe structures studied

Series	1	2	3	4
Initial layer				
d_{Cr} (Å)	40	40	40	40
d_{Fe} (Å)	50	8–20	9–24	8–22
d_{Cr} (Å)	23–52	15	28	47
d_V (Å)	300	300	300	300
d_{Cr} (Å)	23–53	15	28	47
d_{Fe} (Å)	50	8–20	9–24	8–22
Protective layer				
d_{Cr} (Å)	50	50	50	50

X-ray scattering patterns, which showed that the interfacial roughness did not exceed 3–4 Å. The Bragg diffraction patterns showed that the film plane coincided with the (001) crystallographic plane in the texture of all layers. The magnetic measurements on all samples were performed at $T = 20$ K with the aid of a SQUID magnetometer. Assuming that the saturation magnetization is independent of Fe (which is confirmed by our data for the V–Fe system [13]), we used the results of magnetic measurements to refine the thickness of ferromagnetic layers in the samples studied.

The superconducting transition temperature T_c was determined from the change of the sample dc resistance measured according to the standard four-point-probe trechnique. The ratio of the room-temperature resistance to the residual resistance R_{res} near the superconducting transition temperature (called residual resistivity ratio, RRR) for all samples was on the order of $R(300 \text{ K})/R_{res} \sim 4$. Once the phonon contribution to the resistivity of vanadium was known, $\rho_{phon}(300 \text{ K}) = 18.2\ \mu\Omega$ cm, we estimated the residual resistivity as $\rho_{res} \simeq 6\ \mu\Omega$ cm. Following Lazar et al. [9] and using the Pippard relations [25], we established a relation between the mean free path l of conduction electrons and the residual resistivity of vanadium, $\rho_{res}l = 2.5 \times 10^{-6}\ \mu\Omega$ cm^2. For our samples this relation yields $l = 40$ Å. Using this estimate of l and the known BCS coherence length in vanadium, $\xi_o = 440$ Å, we may calculate the superconducting coherence length as $\xi_s = \sqrt{\xi_o l/3.4} = 75$ Å for V layers in our samples.

Figure 1 shows the $T_c(d_{Cr})$ plot, obtained for the samples of series 1 with an Fe-layer thickness fixed at $d_{Fe} \simeq 50$ Å, the experimental points for maximum Fe-layer thicknesses in series 2–4 ($d_{Fe} \sim 20$ Å), and one experimental point for $d_{Cr} = 0$ taken from our previous study [13]. Since the penetration depth of Cooper pairs into iron is $\xi_I \sim 20$ Å [9], the layer of Fe with a thickness of 10 Å in series 2–4 can be considered as thick and comparable in this respect with the samples of series 1
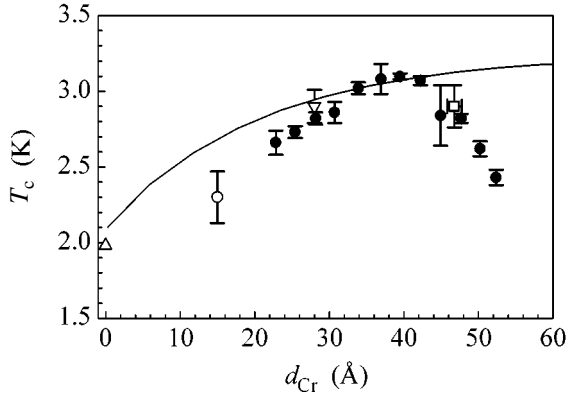
Fig. 1. Plot of the T_c values vs. Cr-layer thickness d_{Cr} for the samples of series 1 with an Fe-layer thickness fixed at $d_{Fe} \simeq 50$ Å, in comparison to the experimental points for maximum Fe-layer thicknesses in series 2–4 (open symbols correspond to data in Fig. 2) and one experimental point for $d_{Cr} = 0$ taken from [13]. Solid curve shows the results of model calculations (see the text).

with $d_{Fe} = 50$ Å. As can be seen, the additional points fit quite well to the $T_c(d_{Cr})$ curve obtained for series 1. In the region of $d_{Cr} \leq 40$ Å, the T_c value increases with d_{Cr}. As the Cr-layer thickness increases further, T_c exhibits a maximum and then decreases at a rate greater than that of the preceding increase.

Another peculiarity revealed by the results of our measurements is illustrated in Figs. 2b–2d, presenting the $T_c(d_{Fe})$ curves for three series of samples with various fixed thicknesses of Cr layers ($d_{Cr} = 15$, 18, and 47 Å, respectively). For comparison, Fig. 2a shows an analogous dependence for the Fe–V–Fe system (i.e., for $d_{Cr} = 0$) taken from [13]. The values of T_c for $d_{Fe} = 0$ are taken from the results of our recent investigation of Cr–V–Cr trilayers [22].

An analysis of the data presented in Fig. 2 reveals the following regularities. The shape of the $T_c(d_{Fe})$ curves is generally analogous to that observed previously for the Fe–V–Fe samples (Fig. 2a). The amplitude of the initial drop in $T_c(d_{Fe})$ decreases with increasing thickness of the Cr spacer separating Fe and V layers. Apparently, this is related to the screening effect of Cr layers. As d_{Cr} increases, the number of Cooper pairs reaching Fe layers decreases and the influence of the exchange field of Fe on the superconductivity of V decreases. For $d_{Cr} = 47$ Å (Fig. 2d), Fe layers exhibit virtually no influence on the superconducting layer, which indicates that the amplitude of the pair wave function in the Fe layer is negligibly small.

Now, let us consider the results of model calculations depicted by solid curves in Figs 1 and 2. The theory of the proximity effect in thin-film multilayer systems of the superconductor–paramagnet–ferromagnet (S–P–F) type was developed by Vodop'yanov *et al.* [26] and originally intended for description of this effect in
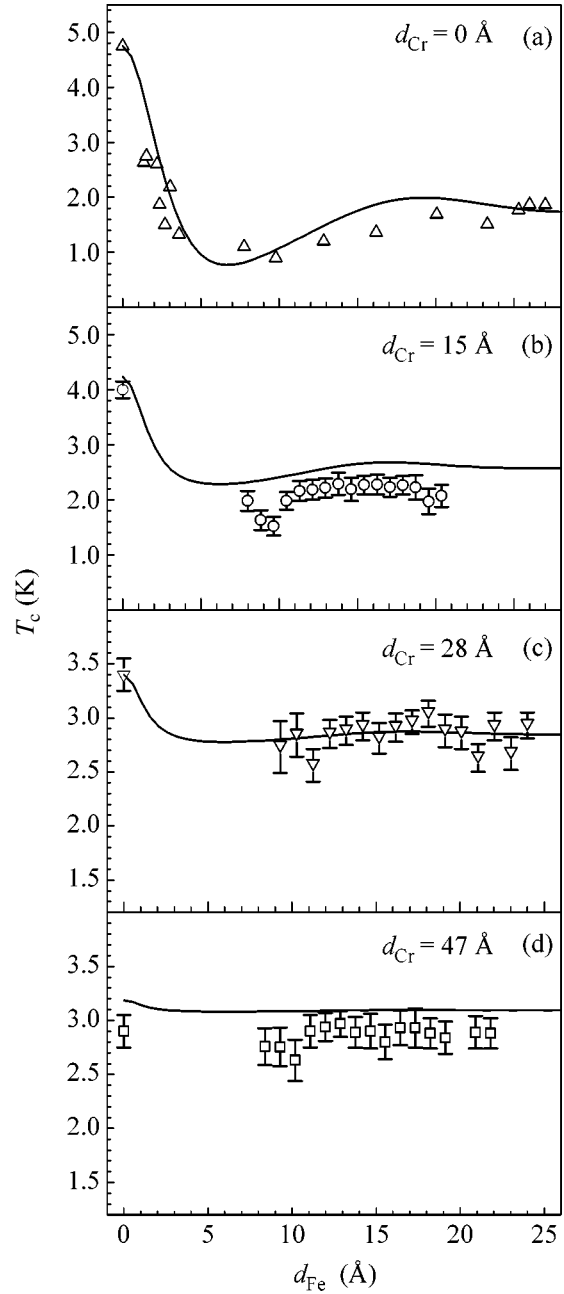
Fig. 2. Plots of the T_c values vs. Fe-layer thickness d_{Fe} for the samples of series 2–4 with fixed $d_{Cr} = 15$ (b), 28 (c), and 47 Å (d), respectively. The values of T_c for $d_{Fe} = 0$ were taken from [22]. For comparison, (a) shows data for the Fe–V–Fe system taken from [13]. Solid curves show the results of model calculations (see the text).

the S–F system with a paramagnetic interlayer formed as a result of mutual diffusion of the S and F layers. We apply this theory to our V–Cr–Fe trilayers, assuming that Cr layer plays the role of a P spacer, as is usually adopted for analysis of the proximity effect in superconductor–chromium system [14].

Prior to analysis, let us refine the parameters of the theory [27] determined previously [13] for description of the $T_c(d_{Fe})$ dependence in Fe–V–Fe trilayers (Fig. 2a). In the S–P–F system, new parameters appear due to the presence of the P layer. Instead of the parameter T_m characterizing transparency of the S–F interface [13], we have to introduce three quantities: $T_{Cr–Fe}$ and $T_{V–Cr}$, characterizing the transparency of Cr–Fe and V–Cr interfaces, respectively, and τ_s representing the characteristic time of the electron spin scattering on the localized magnetic moments in the paramagnetic chromium layer [23]. It is rather difficult to evaluate simultaneously all three parameters from our experimental data. However, we may estimate the $T_{Cr–Fe}$ and $T_{V–Cr}$ values, assuming that (as was demonstrated previously [13]) the transparency of the interface in the S–F system of vanadium and iron is controlled by the difference of the Fermi moments of contacting metals. At the boundary of the ferromagnet, these moments can only be equal for one spin direction. Based on these results, we may set $T_{Cr–Fe}$ approximately equal to the value $T_m = 1.6$ obtained previously for the S–F interface [13] in the V–Fe system, while $T_{V–Cr}$ can be taken very large due to the close electron structures of V and Cr.

Based on these assumptions and using all parameters determined previously for the Fe–V–Fe system [13], we obtained the dependences depicted by solid curves in Figs. 1 and 2; the only fitting parameter was the electron spin scattering time τ_s. We used the same value $\tau_s = 5 \times 10^{-13}$ s in all cases. As can be seen, the general behavior of the data is well reproduced in all cases, including the penetration depth of Cooper pairs in Cr layers, which has proved to be about 40 Å.

However, there is one peculiarity not reflected by the theory even on a qualitative level. This is the sharp drop in $T_c(d_{Fe})$ for $d_{Cr} > 40$ Å (Fig. 1). We may suggest that this peculiarity is related to the transition of Cr layers from a nonmagnetic state to an incommensurate SDW state at $d_{Cr} \simeq 40$ Å. Indeed, the aforementioned Mössbauer measurements [7, 8] showed that Cr at the interface with V occurs in a nonmagnetic state. Of course, Cr layers in our samples contact with V on one side and with Fe on the other side, so that the situation is not identical with that studied in [7, 8]. Generally speaking, we cannot exclude the possibility that a commensurate SDW state might exist at $d_{Cr} < 40$ Å. However, if this were the case, we would have to expect a strong competition between this commensurate state and superconductivity in Cr layers. This would lead to a strong decrease of T_c in vanadium due to the proximity effect, which is not observed in experiment. On the contrary, Cr layers in this region of thicknesses screen the influence of the exchange field of iron (breaking Cooper pairs) on the superconductivity of vanadium. Thus, the whole body of our experimental data shows evidence in favor of the proposed transition from a non-

magnetic state to an incommensurate SDW state in the Cr layer at $d_{Cr} \simeq 40$ Å.

In conclusion, we may ascertain that the results of our investigation of the proximity effect in a thin-film Fe–Cr–V–Cr–Fe layered system clearly demonstrated the screening action of Cr spacers between a superconducting V layer and the Fe layers capable of breaking Cooper pairs. The depth of penetration of Cooper pairs into Cr layers is on the order of 40 Å. In addition, we observed an anomalous decrease in T_c for Cr-layer thicknesses above 40 Å, that is, for spacer thicknesses exceeding the depth of Cooper pair penetration into chromium. We believe that this peculiarity can be explained only by assuming that the transition from a nonmagnetic state to an incommensurate SDW state takes place over the entire thickness of Cr layers. It should be noted that the anomaly observed in $T_c(d_{Cr})$ at $d_{Cr} \simeq 40$ Å in the Fe–Cr–V–Cr–Fe system studied is much more pronounced than analogous features in the data on $T_c(d_{Cr})$ for thin-film V–Cr systems [16–22], where anomalies at $d_{Cr} \sim 40$–60 Å are most likely caused by the aforementioned magnetic transition.

REFERENCES

1. E. Fawcett, Rev. Mod. Phys. **60**, 209 (1988).
2. H. Zabel, J. Phys.: Condens. Matter **11**, 9303 (1999).
3. D. T. Pierce, J. Unguris, R. Celotta, and M. Stiles, J. Magn. Magn. Mater. **200**, 290 (1999).
4. R. S. Fishman, J. Phys.: Condens. Matter **13**, R235 (2001).
5. E. E. Fullerton, S. D. Bader, and J. L. Robertson, Phys. Rev. Lett. **77**, 1382 (1996).
6. H. C. Herper, P. Weinberger, L. Szunyogh, and P. Entel, Phys. Rev. B **68**, 134421 (2003).
7. E. Almokhtar, K. Mibu, A. Nakanishi, *et al.*, J. Phys.: Condens. Matter **12**, 9247 (2000).
8. K. Mibu, M. Almokhtar, A. Nakanishi, *et al.*, J. Magn. Magn. Mater. **226–230**, 1785 (2001).
9. L. Lazar, K. Westerholt, H. Zabel, *et al.*, Phys. Rev. B **61**, 3711 (2000).
10. Ya. V. Fominov, N. M. Chtchelkatchev, and A. A. Golubov, Phys. Rev. B **66**, 014507 (2002).
11. A. S. Sidorenko, V. I. Zdravkov, A. A. Prepelitsa, *et al.*, Ann. Phys. (Leipzig) **12**, 37 (2003).
12. P. Koorevaar, Y. Suzuki, R. Coehoorn, and J. Aarts, Phys. Rev. B **49**, 441 (1994).
13. I. A. Garifullin, D. A. Tikhonov, N. N. Garif'yanov, *et al.*, Phys. Rev. B **66**, 020505(R) (2002).
14. J. J. Hauser, H. C. Theueret, and N. R. Werthamer, Phys. Rev. **142**, 118 (1966).
15. Y. Cheng and M. B. Stearns, J. Appl. Phys. **67**, 5038 (1990).

16. B. M. Davis, J. Q. Zheng, P. R. Auvil, *et al.*, Superlattices Microstruct. **4**, 465 (1988).

17. B. Y. Jin and J. B. Ketterson, Adv. Phys. **38**, 189 (1989).

18. Y. Kuwasawa, Y. Kamata, T. Watanabe, *et al.*, Physica B (Amsterdam) **190**, 333 (1992).

19. Y. Kuwasawa, M. Fukuhara, and T. Nojima, Physica C (Amsterdam) **235–240**, 2559 (1994).

20. Y. Kuwasawa, E. Touma, T. Nojima, and S. Nakano, Physica B (Amsterdam) **194–196**, 2423 (1994).

21. T. Nojima, E. Touma, M. Fukuhara, and Y. Kuwasawa, Physica C (Amsterdam) **226**, 293 (1994).

22. M. Hübener, D. Tikhonov, I. A. Garifullin, *et al.*, J. Phys.: Condens. Matter **14**, 8687 (2002).

23. A. A. Abrikosov and L. P. Gor'kov, Zh. Éksp. Teor. Fiz. **39**, 1781 (1960) [Sov. Phys. JETP **12**, 1243 (1960)].

24. K. Machida, J. Phys. Soc. Jpn. **50**, 2195 (1981).

25. A. B. Pippard, Rep. Prog. Phys. **23**, 176 (1960).

26. B. P. Vodopyanov, L. R. Tagirov, H. Z. Durusoy, and A. V. Berezhnov, Physica C (Amsterdam) **366**, 31 (2001).

27. L. R. Tagirov, Physica C (Amsterdam) **307**, 145 (1998).

Translated by P. Pozdeev

New Method of the Spin-Polarization Detection in Tunnel Junctions Ferromagnet–Insulator–Charge Density Wave Metal[¶]

A. M. Gabovich[1], M. S. Li[2], and A. I. Voitenko[1]

[1] *Institute of Physics, Kiev, 03028 Ukraine*
[2] *Institute of Physics, PL-02-668 Warsaw, Poland*
e-mail: gabovich@iop.kiev.ua; masli@ifpan.edu.pl; voitenko@iop.kiev.ua
Received May 5, 2004; in final form, May 27, 2004

A tunnel junction between a metal partially gapped by charge density waves metal (CDWM) and a ferromagnet (FM) in an external magnetic field is considered. Only the Zeeman paramagnetic effect is taken into account. It is shown that the peaks in the dependence of differential conductance versus voltage, induced by the CDW gap, split, with each peak having a predominant spin polarization. This effect makes it possible to electrically measure the polarization of current carriers in FMs. © *2004 MAIK "Nauka/Interperiodica".*

PACS numbers: 71.45.Lr; 73.40.Gk; 75.20.En; 75.47.Np

Spin electronics (spintronics) has recently become an extremely important area of science as well as a flourishing branch of industry [1–3]. Ferromagnets (FMs) with a metallic character of electrical conductance are an integral part of various magnetoelectronic devices, including, in particular, magnetic tunnel junctions. Spin polarization at the Fermi level is the basic parameter which describes the FM properties relevant for those applications. It is most frequently defined as

$$P = \frac{N_{FM-} - N_{FM+}}{N_{FM-} + N_{FM+}}, \qquad (1)$$

where $N_{FM\mp}$ is the density of states (DOS) of the "majority" ("minority") electrons with spins directed opposite to (along) the quantization axis at the Fermi level. This definition is directly applicable for the interpretation of photoemission or inverse photoemission measurements [4, 5], whereas the account of different interface attributes requires substantial modifications of Eq. (1) during electron transport studies [3, 6, 7]. Anyway, even in strong ferromagnets, P falls short of the saturation value of 100%, which was attained not long ago for the so-called half-metals, e.g., CrO_2 and manganites [6, 8]. Hence, an experimental estimation of P is highly needed both for practical applications and to check electronic band-structure calculations and theories of magnetic tunneling.

The main existing transport methods for the determination of P comprise measurements of (i) tunnel currents between two FMs [2, 3], (ii) tunnel currents between FMs and superconductors (S) in the external

magnetic field H [9], (iii) point-contact conductance in junctions involving two ferromagnetic electrodes [10], and (iv) point-contact conductance with Andreev reflections at an FM/S interface [11]. In this article, we show a new possibility of deducing P from transport studies.

Our approach is an outgrowth of the method suggested by Tedrow and Meservey (see review [9]) for an S–I–FM junction (I stands for an insulator), according to which P may be expressed in terms of the differential tunnel conductivity $G(V) \equiv dJ/dV$ of a quasiparticle tunnel current J taken at definite voltages V in a nonzero external magnetic field H. The main shortcoming of using the S–I–FM tunneling is the dominating role of the orbital (Meissner) depairing over the paramagnetic suppression of superconductivity in most circumstances [12]. Hence, the thin-film geometry of S electrodes is unavoidable and the choice of suitable superconducting covers is troublesome.

Therefore, we analyze a new class of partners for the FMs, namely, metals partially gapped by charge density waves (CDWs), CDWMs [13]. So, the tunneling scheme now has the form CDWM–I–FM. An external magnetic field stimulates a paramagnetic effect in the CDWM analogous to that in superconductors [14, 15]. On the other hand, the giant diamagnetic (Meissner) response does not appear for CDWMs at all, because this state lacks superfluid properties [16]. As for the spin–orbit coupling, which leads to harmful spin flips, its role can be diminished by the adequate choice of the light-atom constituents for CDW materials.

While examining current–voltage characteristics (CVCs), for the sake of definiteness, the bias V is chosen as a voltage difference between the FM and the

[¶] This article was submitted by the authors in English.

CDWM: $V \equiv V_{\mathrm{FM}} - V_{\mathrm{CDWM}}$. It is presumed that, for high enough H, all domains inside the ferromagnet are completely aligned in the field direction. The properties of the partially gapped CDWM are characterized in the framework of the Bilbro–McMillan model [13, 17]. According to this approach, which describes with equal success both the Peierls insulating state in quasi-one-dimensional substances and the excitonic insulating state in semimetals, the Fermi surface (FS) consists of three sections. Two of them ($i = 1, 2$) are nested, with the corresponding fermion quasiparticle spectrum branches obeying the equation

$$\xi_1(\mathbf{p}) = -\xi_2(\mathbf{p} + \mathbf{Q}), \qquad (2)$$

where $\mathbf{Q}$ is the CDW vector. So, the electron spectra here become degenerate (d) and a CDW-related order parameter appears. The rest of the FS ($i = 3$) remains undistorted under the electron–phonon (the Peierls insulator) or Coulomb (excitonic insulator) interaction and is described by the nondegenerate (n) spectrum branch $\xi_3(p)$. A uniform dielectric (CDW) order parameter $\tilde{\Sigma}$ appears only on the nested FS sections. The CDWM phase is described, in the presence of the external magnetic field H and without making allowance for any orbital diamagnetism, by a system of Dyson equations for the normal temperature Green's functions.

For the present purposes, one can disregard the diamagnetic effect while investigating the spin-split peaks of the $G(V)$ for CDWMs. Of course, this does not mean that T_d itself does not depend on H if one goes beyond the approximation adopted in this publication. Nevertheless, the experiment showed that the field-induced CDW suppression $\Delta T_d \propto -H^2$ and is quite small indeed. For example, in the A15 compound V$_3$Si with $T_d(H = 0) = 20.15$ K, even for a very large $H = 156$ kOe, the correction is 0.6 K [18].

Thus, while studying the spin splitting in CDWMs, no restrictions from above appear on the H amplitude other than the natural paramagnetic limit $\mu_B^* H < \Sigma_0 \sqrt{\mu/2}$, where $\mu_B^* = e\hbar/2m^*c$ is the effective Bohr magneton, e is the elementary charge, $\hbar$ is Planck's constant, c is the velocity of light, and m^* is the effective mass of the current carriers. The quantity $\Sigma_0 \equiv \frac{\pi}{\gamma} k_B T_d$ is the amplitude of the CDW order parameter at the temperature $T = 0$; k_B and $\gamma = 1.78\ldots$ are the Boltzmann and Euler constants, respectively; and μ, with $0 \leq \mu \leq 1$, is a relative portion of the FS sections gapped by CDWs. Since we are going to deal with smaller fields, the intriguing problem of the inhomogeneous state [14] analogous to the Larkin–Ovchinnikov–Fulde–Ferrel one in ordinary superconductors for $H \geq H_p$ will be not touched upon. Hence, we assume the function $\tilde{\Sigma}(T)$ to be a BCS-like one.

We calculated $J(V)$ according to expressions which can be straightforwardly obtained by the Green's function method of Larkin and Ovchinnikov [19]. Generally, the current $J(V)$ consists of six components:

$$J(V) = \sum_{\substack{f = n, d, c \\ s = -, +}} J_{f_s}(V), \qquad (3)$$

$$J_{n\mp} = \frac{(1 - \mu)(1 \pm P)V}{2eR}, \qquad (4)$$

$$J_{d\mp} = \frac{\mu(1 \pm P)}{4eR} \qquad (5)$$

$$\times \int_{-\infty}^{\infty} d\omega K(\omega, V, T)|\omega \pm \mu_B^* H| f_{\pm}(\omega, H, \Sigma);$$

$$J_{c\mp} = \frac{\mu(1 \pm P)\tilde{\Sigma}}{4eR} \qquad (6)$$

$$\times \int_{-\infty}^{\infty} d\omega K(\omega, V, T)\,\mathrm{sgn}(\omega \pm \mu_B^* H) f_{\pm}(\omega, H, \Sigma).$$

Here,

$$K(\omega, V, T) = \tanh\frac{\omega}{2T} - \tanh\frac{\omega - eV}{2T}, \qquad (7)$$

$$f_{\pm}(\omega, H, \Sigma) = \frac{\theta(|\omega \pm \mu_B^* H| - \Sigma)}{\sqrt{(\omega \pm \mu_B^* H)^2 - \Sigma^2}}, \qquad (8)$$

the upper (lower) sign corresponds to the majority (minority) spin orientation, respectively; R is the "normal state" (above T_d) resistance of the junction; and $\theta(x)$ denotes the Heaviside theta function. The current components depend on the phase φ of $\tilde{\Sigma} = \Sigma e^{i\varphi}$, whereas the thermodynamic properties of CDW superconductors are degenerate with respect to s. We suggested that quasiparticles from all the FS sections make their contributions to the total current proportional to the DOS of the relevant section. That means an absence of any kind of directional tunneling, which is possible in principle [20].

An important difference between the problem in point and its counterpart appropriate to BCS superconductivity is the emergence of the terms $J_{c\mp}$. They reflect the existence of the electron–hole pairing in CDWMs, which originates from the interband Green's function G_c, and have different behavior than the remaining terms linked to the conventional normal Green's functions. To a large extent, $\mathcal{G}_c$ is analogous to the anomalous Gor'kov Green's function $\mathcal{F}$, which, however, determines the Josephson rather than quasiparticle tunnel current. The appearance of terms (6) leads to the drastic *asymmetry* of the CVC of nonsymmetrical tunnel junctions involving CDWMs. In incom-

mensurate CDWMs, the order parameter phase φ is arbitrary. However, to understand the picture qualitatively, it is enough to restrict the consideration to the particular case of commensurate CDWs, when φ is either 0 or π. Then, relevant equations describe tunneling between, e.g., excitonic insulators.

Conductivities $G_{fs}(V)$ can be obtained by differentiating relevant Eqs. (4)–(6). At $T = 0$, the corresponding analytical expressions become

$$G_{n\mp}(V) = \frac{(1-\mu)(1 \pm P)}{2R}, \qquad (9)$$

$$\begin{aligned} &G_{d\mp}(V) \\ &= \frac{\mu(1 \pm P)}{2R} \mathrm{sgn}(V)(eV \pm \mu_B H) f_\pm(eV, H, \Sigma), \end{aligned} \qquad (10)$$

$$G_{c\mp}(V) = \frac{\mu(1 \pm P)\tilde{\Sigma}}{2R} \mathrm{sgn}(V) f_\pm(eV, H, \Sigma). \qquad (11)$$

Naturally, the sum of the G_n terms gives the constant $(1 - \mu)/R$.

The dependences of the dimensionless conductance RdJ/dV for the CDWM–I–FM junction on the dimensionless bias voltage eV/Σ_0 are shown in Fig. 1 for $\tilde{\Sigma} > 0$. Other dimensionless parameters of the problem are the normalized external magnetic field $h = \mu_B^* H/\Sigma_0$ and temperature $t = k_B T/\Sigma_0$. It is readily seen that $G(V)$ is highly asymmetrical, contrary to the symmetrical patterns appropriate to tunnel junctions involving superconductors regardless of whether those junctions are symmetrical or not [21]. Mathematically, it stems from an almost total compensation between $G_d(V)$ and $G_c(V)$ logarithmic singularities at voltages of one sign and their enhancement at voltages of the other sign (for the adopted choice $\tilde{\Sigma} > 0$, it means negative and positive V, respectively). In the absence of the external magnetic field and spin polarization, such an asymmetrical behavior of $G(V)$ was obtained by us earlier [22–24]. When H is switched on, the electronic DOS peak splits as in the case of superconductors [9, 25]. The spin splitting is noticeable, however, only for one CVC branch ($V > 0$ in the case $\tilde{\Sigma} > 0$, the other branch contains only remnants of the gap-related features). Thus, the simple algebraic procedure of Tedrow and Meservey of finding P from a set of G values measured at certain V's and H, successful for S–I–FM junctions [9, 26], seems to fail for CDWM–I–FM ones, because this method needs the values of conductance on both voltage branches.

Nevertheless, the advantage of the setup proposed here to detect spin-polarization-induced changes consists in a more clear manifestation of the spin-splitting effect for one CVC branch and in a larger scale of Σ for existing CDWMs as compared to the energy gaps Δ in their superconducting counterparts, with the dependences $G(V)$ being very sensitive to the value of P.
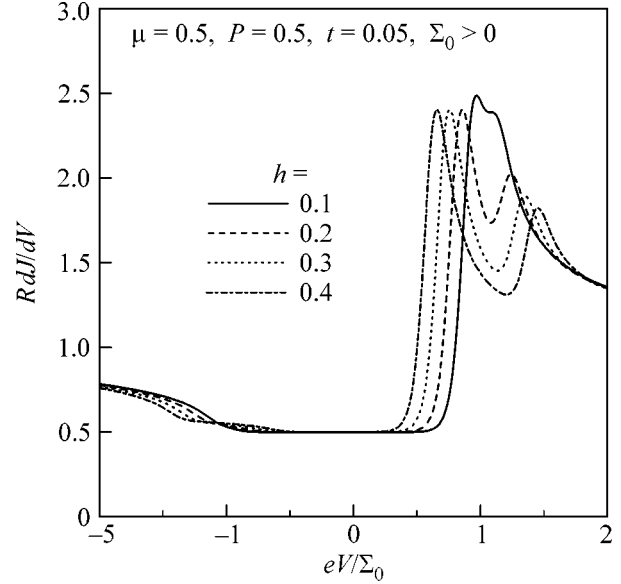
Fig. 1. Dependences of differential conductance on bias voltage V across the tunnel junction made up of charge-density wave metal (CDWM) and ferromagnet (FM) for various external magnetic fields H. See explanations in the text.

Moreover, the CVCs crucially depend on the sign of $\tilde{\Sigma}$ in the CDWM. Let us first consider the case $\tilde{\Sigma} > 0$ (Fig. 2a). One can see how the spin-splitting pattern is distorted for a ferromagnetic counterelectrode ($P \neq 0$) in comparison with the nonpolarized case ($P = 0$). In particular, the minority-spin peak, which is positioned farther from the zero bias than the majority one, is reduced with increasing P, so that, for complete polarization ($P = 1$, this limit is attainable in half-metallic ferromagnets [6, 8, 10]), it disappears and only one (majority) peak survives.

When $\tilde{\Sigma} < 0$ (Fig. 2b), the minority-spin peak disappears with increasing P similarly to the opposite case $\tilde{\Sigma} > 0$, but now it is situated closer to the zero bias than the majority one. Hence, the "modified" symmetry relationship

$$G(-\tilde{\Sigma}, V) = G(\tilde{\Sigma}, -V), \qquad (12)$$

appropriate for junctions involving normal or superconducting CDW electrodes and nonferromagnetic normal metal counterelectrodes (cf. $P = 0$ curves on both panels), is no longer valid, and the CVCs for $H \neq 0$ lack any symmetry properties. Then, different signs of $\tilde{\Sigma}$ can be distinguished by CVC measurements. It is worth noting once more that the actual $\tilde{\Sigma}$ sign for a specific junction might occur at random, induced by unpredictable fluctuations, since the bulk thermodynamic free energy of normal or superconducting CDW metals does not depend on this sign [27–29].
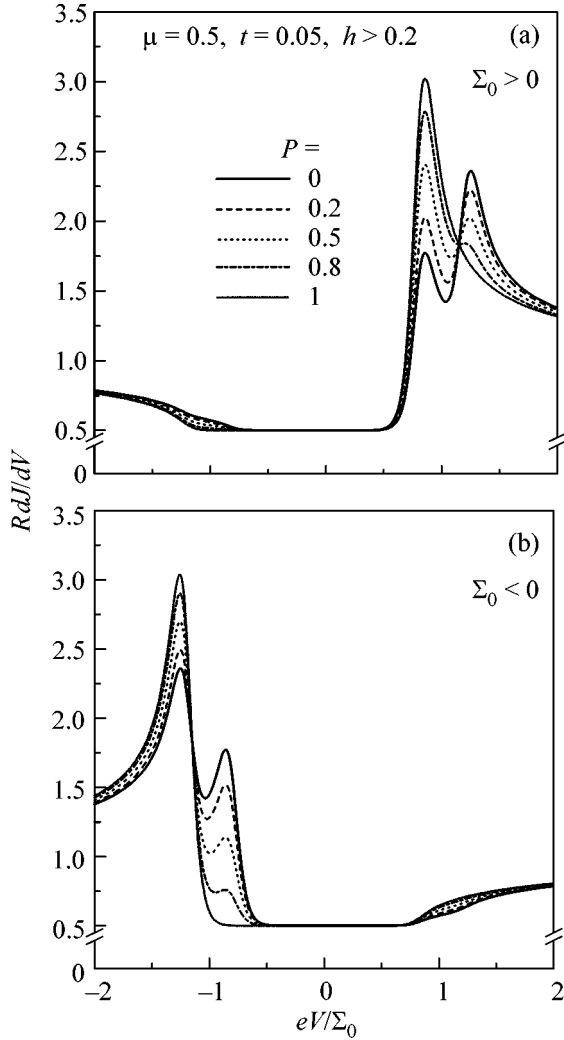
Fig. 2. The same as in Fig. 1 but for various polarizations P of electrons on the FM Fermi level. Panels correspond to different sign of the dielectric order parameter $\tilde{\Sigma}$ in CDWM. See explanations in the text. (a) $\Sigma_0 > 0$, and (b) $\Sigma_0 < 0$.

Fig. 3. The same as in Fig. 1 but for various temperatures T.

At the same time, the predicted effect is highly sensitive to the temperature. The smoothing effect of the latter is shown in Fig. 3. The Zeeman splitting becomes unobservable already at a relatively small value, $t = 0.2$. However, CDW metals with T_d of the order of 10–15 K are now available [30, 31] with the corresponding destructive magnetic fields $H \approx 180$–270 kOe, which are attainable experimentally. Hence, larger magnetic fields may be applied to detect the paramagnetic spin splitting against the background of various smearing factors, temperature included.

To illustrate that the predicted phenomenon can indeed be observed, let us consider the spin–orbit smearing in $2H$-NbSe$_2$ with the superconducting critical temperature $T_c = 7.2$ K and $T_d = 33.5$ K [13] and compare it with that in Al, where the spin-splitting
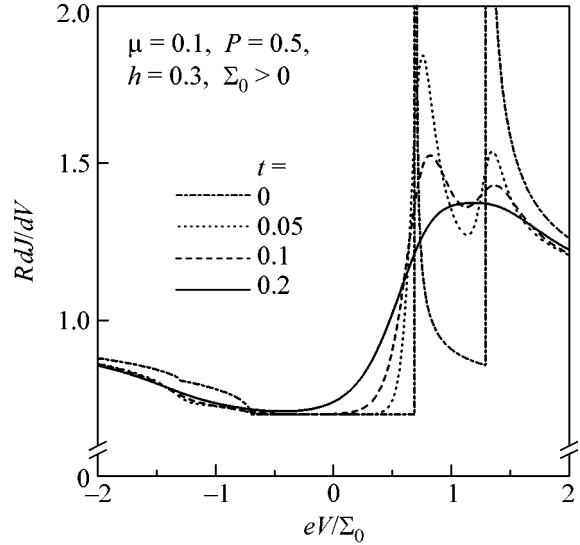
effect was observed [9]. We shall confine the consideration for $2H$-NbSe$_2$ to the CDW-induced peaks only. The spin–orbit scattering in superconductors is governed by a single parameter, $b = \hbar/(3\tau_{so}\Delta) \propto Z^4/\Delta$, where $\hbar/\tau_{so}$ is the spin–orbit scattering rate, Z is the material atomic number, and Δ is the superconducting gap. For Al, $Z_{Al} = 13$, $\Delta_{Al} \approx 0.4$ meV, and $b_{Al} \approx 0.05$, while even the value 0.2 ensures the satisfactory spin splitting of the Δ-driven peaks [9, 25]. On the other hand, using the same ideas, $b_{2H\text{-NbSe}_2} \propto Z_{Nb}^4/\Sigma$ for $2H$-NbSe$_2$, where $\Sigma \approx 34$ meV is the measured dielectric gap [32] and $Z_{Nb} = 41$ ($Z_{Se} = 34$, which may only improve our estimation). Assuming the elastic scattering rates to be of the same order of magnitude in both the materials, we obtain $b_{2H\text{-NbSe}_2} \approx 1.2 b_{Al} \approx 0.06$. Thus, even if the spin splitting of the Δ-induced peaks in $2H$-NbSe$_2$ is smeared, that of the CDW-triggered ones should remain resolved. This is the more so because the superconductivity- and CDW-induced CVC peaks are well separated from one another (cf. the values of T_c and T_d for $2H$-NbSe$_2$ quoted above).

We would like to indicate several other possible candidates for the CDW partner of FMs in tunnel sandwiches. These are organic CDW metals α-(ET)$_2$MHg(SCN)$_4$ (M = K, Tl, Rb) [15, 30] and Per$_2$[M(mnt)$_2$] (Au, Pt) [31]. The main weak point of those materials is the presence of heavy elements Hg, Tl, Au, or Pt, which is dangerous because of a possible spin–orbit smearing of the spin-split $G(V)$ peaks. A two-leg ladder compound Sr$_{14-x}$Ca$_x$Cu$_{24}$O$_{41}$ also seems very promising. Actually, Ca doping alters T_d and Σ over a remarkably wide range from 210 K and 130 meV, respectively, for $x = 0$ down to 10 K and 3 meV for $x = 9$ [33].

On the whole, the application of the fruitful ideas developed earlier for superconductors [9] to normal partially CDW-gapped metals seems useful for studying those strongly correlated objects.

REFERENCES

1. J. F. Gregg, I. Petej, E. Jouguelet, and C. Dennis, J. Phys. **35**, R121 (2002).

2. M. Bode, Rep. Prog. Phys. **66**, 523 (2003).

3. E. Y. Tsymbal, O. N. Mryasov, and P. R. LeClair, J. Phys.: Condens. Matter **15**, R109 (2003).

4. P. D. Johnson, Rep. Prog. Phys. **60**, 1217 (1997).

5. F. J. Himpsel, J. E. Ortega, G. J. Mankey, and R. F. Willis, Adv. Phys. **47**, 511 (1998).

6. J. M. D. Coey and S. Sanvito, J. Phys. **37**, 988 (2004).

7. X.-G. Zhang and W. H. Butler, J. Phys.: Condens. Matter **15**, R1603 (2003).

8. V. Yu. Irkhin and M. I. Katsnelson, Usp. Fiz. Nauk **164**, 705 (1994) [Phys. Usp. **37**, 659 (1994)].

9. R. Meservey and P. M. Tedrow, Phys. Rep. **238**, 173 (1994).

10. J. M. D. Coey and M. Venkatesan, J. Appl. Phys. **91**, 8345 (2002).

11. G. J. Strijkers, Y. Ji, F. Y. Yang, *et al.*, Phys. Rev. B **63**, 104510 (2001).

12. K. Maki, in *Superconductivity*, Ed. by R. D. Parks (Marcel Dekker, New York, 1969), Vol. 2, p. 1035.

13. A. M. Gabovich, A. I. Voitenko, and M. Ausloos, Phys. Rep. **367**, 583 (2002).

14. R. H. McKenzie, cond-mat/9706235.

15. A. G. Lebed, Pis'ma Zh. Éksp. Teor. Fiz. **78**, 170 (2003) [JETP Lett. **78**, 138 (2003)].

16. D. Jérome, T. M. Rice, and W. Kohn, Phys. Rev. **158**, 462 (1967).

17. G. Bilbro and W. L. McMillan, Phys. Rev. B **14**, 1887 (1976).

18. S. J. Williamson, C. S. Ting, and H. K. Fung, Phys. Rev. Lett. **32**, 9 (1974).

19. A. I. Larkin and Yu. N. Ovchinnikov, Zh. Éksp. Teor. Fiz. **51**, 1535 (1966) [Sov. Phys. JETP **24**, 1035 (1967)].

20. R. A. Klemm, Phys. Rev. B **67**, 174 509 (2003).

21. L. Solymar, *Superconductive Tunneling and Applications* (Chapman and Hall, London, 1972; Mir, Moscow, 1974).

22. A. M. Gabovich and A. I. Voitenko, Phys. Rev. B **52**, 7437 (1995).

23. A. M. Gabovich and A. I. Voitenko, Phys. Rev. B **56**, 7785 (1997).

24. A. M. Gabovich and A. I. Voitenko, J. Phys.: Condens. Matter **9**, 3901 (1997).

25. P. Fulde, Adv. Phys. **22**, 667 (1973).

26. P. M. Tedrow and R. Meservey, Phys. Rev. B **7**, 318 (1973).

27. A. M. Gabovich, A. S. Gerber, and A. S. Shpigel, Phys. Status Solidi B **141**, 575 (1987).

28. A. M. Gabovich and A. S. Shpigel, J. Phys. F **14**, 3031 (1984).

29. A. M. Gabovich, M. S. Li, H. Szymczak, and A. I. Voitenko, J. Phys.: Condens. Matter **15**, 2745 (2003).

30. J. Singleton, Rep. Prog. Phys. **63**, 1111 (2000).

31. D. Graf, J. S. Brooks, E. S. Choi, *et al.*, Phys. Rev. B **69**, 125 113 (2004).

32. C. Wang, B. Giambattista, C. G. Slough, *et al.*, Phys. Rev. B **42**, 8890 (1990).

33. T. Vuletić, B. Korin-Hamzić, S. Tomić, *et al.*, Phys. Rev. Lett. **90**, 257002 (2003).

Energy Absorption in Time-Dependent Unitary Random Matrix Ensembles: Dynamic versus Anderson Localization¶

M. A. Skvortsov[1, *], D. M. Basko[2], and V. E. Kravtsov[1, 2]

[1] Landau Institute for Theoretical Physics, Russian Academy of Sciences, Moscow, 117940 Russia
[2] The Abdus Salam International Center for Theoretical Physics, 34100 Trieste, Italy
*e-mail: skvor@itp.ac.ru

We consider energy absorption in an externally driven complex system of noninteracting fermions with the chaotic underlying dynamics described by the unitary random matrices. In the absence of quantum interference, the energy absorption rate $W(t)$ can be calculated with the help of the linear-response Kubo formula. We calculate the leading two-loop interference correction to the semiclassical absorption rate for an arbitrary time dependence of the external perturbation. Based on the results for periodic perturbations, we make a *conjecture* that the dynamics of the periodically driven random matrices can be mapped onto the one-dimensional Anderson model. We predict that, in the regime of strong dynamic localization, $W(t) \propto \ln(t)/t^2$ rather than decaying exponentially. © 2004 MAIK "Nauka/Interperiodica".

PACS numbers: 72.10.Bg; 05.40.-a

1. INTRODUCTION

Recent years had revealed an increasing interest [1–4] in time-dependent random matrices, arising from the field of condensed matter physics. The natural way to study a complex quantum system is to couple it to an external field φ which enters the Hamiltonian $H[\varphi] = H_0 = V\varphi$ as a parameter and can be controlled at will. Applying a time-dependent perturbation $\varphi(t)$ gives access to quantum dynamics of the many-electron wave function governed by the Schrödinger equation $i\partial\Psi(t)/\partial t = H[\varphi(t)]\Psi(t)$. If the perturbation frequency and the relevant energies (e.g., the electron temperature) are smaller than the Thouless energy in the sample, then it is possible to apply a universal description in terms of the random-matrix theory (RMT) of an appropriate symmetry [5]. The resulting time-dependent theory is specified by two model-dependent quantities, which should be determined microscopically [6]: the mean level spacing Δ and the sensitivity of the parametric spectrum $\langle(\partial E_i/\partial\varphi)^2\rangle$ to the variation of the control parameter φ.

The crucial quantity characterizing quantum dynamics of the system is the energy absorption rate

$$W(t) \equiv \frac{d\langle E(t)\rangle}{dt} \tag{1}$$

and its dependence on the form of the external perturbation $\varphi(t)$. (In Eq. (1), $\langle E(t)\rangle$ is the expectation value of the total energy of the system.) The standard approach to calculating W is based on the Kubo linear response theory, which connects the kinetic response of a system

to the equilibrium correlator of generalized currents. In the present case, the generalized current corresponding both to the quantity of interest (1) and to the source of nonstationarity is $dH/dt = (\partial H/\partial\varphi)v$, where $v = d\varphi/dt$ is the perturbation velocity. Then, the Kubo formula gives for the standard Wigner–Dyson random matrix ensembles [7, 8]:

$$W_0 = \frac{\beta\pi}{2}C_\beta(0)v^2, \tag{2}$$

where

$$C_\beta(0) \equiv \frac{1}{\Delta^2}\left\langle\left(\frac{\partial E_i}{\partial\varphi}\right)^2\right\rangle = \frac{1}{\beta\Delta^2}\left\langle\left(\frac{\partial H_{i\neq j}}{\partial\varphi}\right)^2\right\rangle \tag{3}$$

is the level velocity autocorrelation function, with $E_i[\varphi]$ being the adiabatic levels of an instantaneous Hamiltonian, and $\beta = 1$ or 2 for the orthogonal (GOE) or unitary (GUE) symmetry classes, respectively. Kubo dissipation rate (2) is ohmic scaling $\propto v^2$ regardless of the system's symmetry.

Application of the Kubo formula essentially relies on the assumption of a continuous spectrum [9]. The spectrum may be considered as continuous if the smearing γ of energy levels exceeds the system's mean level spacing Δ. In condensed matter, this condition is usually satisfied for a typical electron system at not too low temperatures, when the inelastic smearing $\gamma_{\mathrm{in}} \gg \Delta$. However, in the RMT, the inelastic broadening is absent by definition and the spectrum of the stationary (at $v = 0$) Hamiltonian is discrete. The level smearing is then generated *dynamically* as a result of time dependence of the Hamiltonian $H[\varphi(t)]$.

¶ This article was submitted by the authors in English.

This mechanism of dynamically generated smearing of the spectrum due to nonstationarity is the key point in understanding the properties of time-dependent random matrices. It constitutes the main difference between them and the usual problems in condensed matter physics, leading to a number of counterintuitive consequences. One of them is the breakdown of the Kubo formula at small velocities $v \ll v_K \sim \Delta^2 / \sqrt{C_\beta(0)}$, when the smearing γ becomes smaller than Δ. In this regime, the dynamics is adiabatic and dissipation occurs due to rare Landau–Zener transitions between the neighboring levels. Then, the energy absorption rate becomes statistics-dependent with $W \sim v^{\beta/2 + 1}$ [7]. Thus, in a system with dynamically generated smearing, the low-velocity response is generally nonlinear.

The second nontrivial effect which is not captured by Kubo formula (2) comes into play for reentrant perturbations when the system is being swept through the same realization of disorder many times. For a certain type of time-dependent perturbations, successive accumulation of destructive interference correction may lead to localization of the single-particle quantum-mechanical states in the energy space. This effect, known as dynamic localization [10], manifests itself in vanishing of the absorption rate and saturation of the total absorbed energy in the limit of long duration of the external perturbation. Dynamic localization was studied extensively for the model case of the kicked quantum rotor [10], while, for the case of driven random matrices, it was discovered in [4].

Though dynamic localization is in many aspects analogous [4] to the conventional Anderson localization, they are different in their relation to the Kubo formula. Conductivity in the Anderson model is described by the linear-response (in the electric field) Kubo formula, with quantum interference effects being encoded in the disorder-averaged Kubo commutator. On the other hand, quantum corrections to the absorption rate responsible for dynamic localization do depend on the velocity of the perturbation and, therefore, are not contained in the Kubo correlator (2). This is another consequence of the fact that, in time-dependent RMT, the smearing of the spectrum is generated dynamically.

Recently, the first quantum interference correction to the Kubo dissipation rate (2) for the *orthogonal* symmetry class was considered, taking into account both the original discreteness of the spectrum [3] and the effect of weak dynamic localization [4]. The one-loop relative correction to W_0 contains a dynamic cooperon and evaluates either to a positive number $\sim (v/v_K)^{2/3}$ for a linear bias $\varphi = vt$ [3] or to a negative and growing in time correction $\propto -\sqrt{t}$ for a monochromatic perturbation switched on at $t = 0$ [4] (in this case, the dynamic localization effect is most pronounced).

The purpose of this letter is to study the quantum interference correction to W_0 for the *unitary* symmetry class that involves evaluation of the two-loop diagrams

made of dynamic diffusons. We will derive the general expression for $\delta W(t)$ [Eq. (21)] valid for an arbitrary time dependence of $\varphi(t)$ and then discuss the limits of linear and (multi-) periodic perturbations.

We demonstrate that the first quantum correction vanishes for the linear perturbation $\varphi(t) = vt$ and grows $\propto t$ for the harmonic perturbation. On comparing the orthogonal and unitary quantum corrections for the cases of dynamic and Anderson localization, we suggest that the dynamics of the periodically driven RMT can be mapped onto the one-dimensional Anderson model.

2. DESCRIPTION OF THE FORMALISM

Quantum dynamics of time-dependent unitary random matrices can be conveniently described by the nonlinear Keldysh σ model derived in [3]. The effective action (with the weight e^{-S})

$$S[Q] = \frac{\pi i}{\Delta} \mathrm{Tr} \hat{E} Q - \frac{\pi^2 C_u(0)}{4} \mathrm{Tr}[\varphi, Q]^2, \qquad (4)$$

is a functional of the Q field acting in the Keldysh (Pauli matrices σ_i) and time spaces. In Eq. (4), the operators $\hat{E}$ and φ have the matrix elements $\hat{E}_{tt'} = i\delta_{tt'}\partial_{t'}$ and $\varphi_{tt'} = \delta_{tt'}\varphi(t')$, and $C_u(0)$ is the level velocity autocorrelation function defined by Eq. (3) with $\beta = 2$.

The saddle point of action (4) is given by

$$\Lambda_{tt'} = \begin{pmatrix} \delta_{tt'} & 2F^{(0)}_{tt'} \\ 0 & -\delta_{tt'} \end{pmatrix}, \qquad (5)$$

with the distribution function $F^{(0)}$ satisfying the kinetic equation

$$(\partial_t + \partial_{t'}) F^{(0)}_{tt'} = -\Gamma [\varphi(t) - \varphi(t')]^2 F^{(0)}_{tt'}, \qquad (6)$$

where we denoted $\Gamma = \pi C_u(0)\Delta$.

The whole manifold of the Q matrices can be parametrized as

$$Q = U_F^{-1} P U_F, \quad P = U^{-1}\sigma_3 U, \qquad (7)$$

where the matrices U are unitary, so that P is a Hermitian field, whereas all non-Hermiticity is located in the matrices

$$(U_F)_{tt'} = \begin{pmatrix} \delta_{tt'} & F^{(0)}_{tt'} \\ 0 & -\delta_{tt'} \end{pmatrix} \qquad (8)$$

(in particular, the standard saddle point (5) corresponds to $P = \sigma_3$).

(a)   (b)   (c)
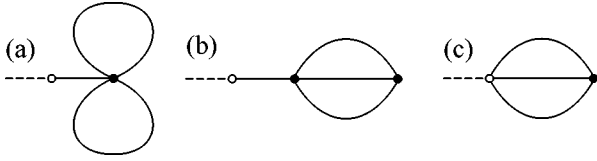
Two-loop diagrams for the distribution function *F*, corresponding to the terms of Eq. (15). Solid lines denote the diffusions.

For perturbative calculations, we choose the standard rational parametrization of the *P* matrix,

$$P = \sigma_3(1 + V/2)(1 - V/2)^{-1}, \qquad (9)$$

which has the unit Jacobian $\partial P/\partial V = 1$. The matrix *V* anticommuting with σ_3 is given explicitly by

$$V = \begin{pmatrix} 0 & d \\ -d^\dagger & 0 \end{pmatrix}, \qquad (10)$$

with the matrix *d* acting in the time space only. Its bare correlator inferred from the Gaussian part of the action has the form

$$\langle d_{t_+ t_-} d^*_{t'_+ t'_-}\rangle_0 = \frac{2\Delta}{\pi}\delta(\eta - \eta')\mathcal{D}_\eta(t, t'), \qquad (11)$$

where we have denoted $t_\pm = t \pm \eta/2$, $t'_\pm = t' \pm \eta'/2$, and introduced the free diffuson propagator [1, 2, 4, 11]

$$\mathcal{D}_\eta(t, t') = \theta(t - t')\exp\left\{-\int_{t'}^{t}\Gamma[\varphi(\tau_+) - \varphi(\tau_-)]^2 d\tau\right\}. \quad (12)$$

Physical quantities are contained in the average $\langle Q \rangle \equiv \int Q\, e^{-S[Q]} DQ$. Due to causality, $\langle Q_{tt} \rangle$ shares the structure of Eq. (5) but with the saddle-point distribution $F^{(0)}$ substituted by the exact distribution *F*. The energy absorption rate can be calculated as [4]

$$W(t) = -\frac{\pi i}{\Delta}\lim_{\eta \to 0}\partial_t\partial_\eta F_{t + \eta/2, t - \eta/2}. \qquad (13)$$

3. PERTURBATION THEORY

Expanding the Keldysh (upper-right) block of the matrix *Q* in terms of the diffusons *d* with the help of Eqs. (7)–(10), one obtains the perturbative series

$$F = F^{(0)} - \frac{\langle d \rangle}{2} - \frac{\langle F^{(0)}d^\dagger d + dd^\dagger F^{(0)} \rangle}{4} + \frac{\langle dd^\dagger d \rangle}{8} + \dots. \qquad (14)$$

The two-loop correction to the distribution function is given by three pairings:

$$\delta F = \frac{\langle dS^{(5)}\rangle_0}{2} - \frac{\langle dS^{(4)}S^{(3)}\rangle_0}{2} + \frac{\langle dd^\dagger dS^{(3)}\rangle_0}{8}, \qquad (15)$$

shown diagrammatically in the figure. The other possible pairings vanish due to causality of the theory. In Eq. (15), the vertices $S^{(m)}$ come from expansion of action (4) to the order W^m. In rational parametrization (9), they are given by the following expressions:

$$S^{(3)} = \frac{\pi\Gamma}{2\Delta}\int\varphi_{12}\varphi_{34}F^{(0)}_{12}d^*_{32}d_{34}d^*_{14}, \qquad (16)$$

$$S^{(5)} = \frac{\pi\Gamma}{8\Delta}$$
$$\times \int\varphi_{12}(\varphi_{34} + \varphi_{56})F^{(0)}_{12}d^*_{23}d^*_{43}d_{45}d^*_{65}d^*_{61} + \dots, \qquad (17)$$

$$S^{(4)} = -\frac{\pi}{8\Delta}\int(\partial_5 + \partial_6)d_{56}d^*_{76}d_{78}d^*_{58}$$
$$- \frac{\pi\Gamma}{16\Delta}\int(\varphi^2_{56} + \varphi^2_{58} + \varphi^2_{67} + \varphi^2_{78}$$
$$- \varphi^2_{57} - \varphi^2_{68})d_{56}d^*_{76}d_{78}d^*_{58} + \dots. \qquad (18)$$

The terms not included in Eqs. (17) and (18) do not contribute to the pairings shown in the figure. In writing Eqs. (16)–(18), we used the concise notations $F_{ij} \equiv F_{t_i t_j}$, $d_{ij} \equiv d_{t_i t_j}$ and $\varphi_{ij} \equiv \varphi(t_i) - \varphi(t_j)$, with integration being performed over all time arguments involved.

Diagrams (a) and (b) shown in the figure contain a loose diffuson [2] which couples *d* to the rest of the diagram. As a result, the corresponding correction to the distribution function $F_{t + \eta/2, t - \eta/2}$ can be written as

$$\delta F^{(ab)}_{t + \eta/2, t - \eta/2}$$
$$= \int dt' dt''\mathcal{D}_\eta(t, t')\Xi(t', t'', \eta)F_{t'' + \eta/2, t'' - \eta/2}, \qquad (19)$$

where t' is the "center of mass" time at the right end of the loose diffuson and $\Xi(t', t'', \eta)$ is a complicated expression denoting the rest of the diagram. The corresponding correction to the energy absorption rate given by Eq. (13) simplifies to

$$\delta W^{(ab)}(t) = -\frac{1}{\Delta}\lim_{\eta \to 0}\frac{\partial}{\partial\eta}\frac{1}{\eta}\int dt''\Xi(t, t'', \eta), \qquad (20)$$

where we employed Eq. (12) and used the asymptotics $F_{t_+, t_-} \sim 1/i\pi\eta$ at $\eta \to 0$.

On the contrary, diagram (c) in the figure does not contain a loose diffuson and cannot be represented in form (20) with already taken derivative with respect to the external time *t*.

Finally, it is worth mentioning that diagram (a) is completely canceled against the part of diagram (b) which contains the time derivative originating from the first term in Eq. (18).

As a result of straightforward but rather lengthy calculation, one ends up with the general expression for

the two-loop correction to the Kubo dissipation rate (2) valid for an arbitrary $\varphi(t)$:

$$\delta W(t) = \frac{\Gamma\Delta}{2\pi^2}\lim_{\eta\to 0}\frac{\partial}{\partial\eta}\frac{1}{\eta}\int_0^\infty dxdydz$$

$$\times\left(\frac{\partial}{\partial t} - 2\Gamma\varphi_{56}\varphi_{78}\right)\varphi_{12}\varphi_{34}$$

$$\times\mathscr{D}_{\eta+x+y}\left(t - \frac{x}{2} - \frac{y}{2}, t - \frac{x}{2} - \frac{y}{2} - z\right) \quad (21)$$

$$\times\mathscr{D}_{\eta-x-z}\left(t - \frac{x}{2} - \frac{z}{2}, t - \frac{x}{2} - \frac{z}{2} - y\right)$$

$$\times\mathscr{D}_{\eta+y-z}\left(t - \frac{y}{2} - \frac{z}{2}, t - \frac{y}{2} - \frac{z}{2} - x\right),$$

where $t_{1,2} = t_{\pm} - x - y - z$, $t_3 = t_+ - z$, $t_4 = t_- - y$, $t_5 = t_+ - x - z$, $t_{6,7} = t_{\mp}$, and $t_8 = t_- - x - y$. In Eq. (21), the term with $\partial/\partial t$ describes the contribution of diagram (c), while the rest is the contribution of diagrams (a) and (b). Though the derivatives with respect to η and t can be easily calculated with the help of Eq. (12), we leave them unevaluated in order to keep the simplest form of the expression.

4. LINEAR CASE

We start the analysis of general formula (21) with the case of a linear bias $\varphi(t) = vt$. Then, dynamic diffuson (12) is given by $\mathscr{D}_\eta(t_1, t_2) = \theta(t_1 - t_2)\exp\{-\Omega^3\eta^2(t_1 - t_2)\}$, where $\Omega = (\Gamma v^2)^{1/3}$ is the dephasing rate due to the time-dependent perturbation [3]. Since the diffuson $\mathscr{D}_\eta(t_1, t_2)$ depends only on $t_1 - t_2$, the integrand in Eq. (21) does not depend on t and the corresponding time derivative describing the contribution of diagram (c) vanishes.

The product of three diffusons in Eq. (21) is an even function of η; hence, η dependence should be taken into account only in the terms φ_{ij}. The resulting expression becomes

$$\delta W = \frac{\Omega^6\Delta}{\pi^2}\int_0^\infty dxdydz(-x^2 + 5xy)$$

$$\times \exp\{-\Omega^3(x + y)(y + z)(z + x)\}, \quad (22)$$

where we employed the symmetry between the integration variables to simplify the final expression.

The integrals in Eq. (22) are given by

$$\int_0^\infty dxdydz\begin{bmatrix}x^2\\xy\end{bmatrix}e^{-(x+y)(y+z)(z+x)} = \begin{bmatrix}5\\1\end{bmatrix}\times\frac{\Gamma^2(1/3)}{48}, \quad (23)$$

leading to a surprising cancellation of the two-loop quantum correction in the unitary case mentioned in [3].

It is also instructive to consider the case of the linear perturbation switched on at $t = 0$: $\varphi(t) = \theta(t)vt$. Here, the term with $\partial/\partial t$ in Eq. (21) is generally nonzero but it is small in the most interesting limit $\Omega t \gg 1$. The time-dependent $\delta W(t)$ is then given by Eq. (22), where the region of integration is now bounded from above by the condition $x + y + z < t$. The correction to the total absorbed energy becomes

$$\delta E(t) = \frac{\Omega^6\Delta}{\pi^2}\int_0^\infty dxdydz\min(x + y + z, t)$$

$$\times(-x^2 + 5xy)e^{-\Omega^3(x+y)(y+z)(z+x)}. \quad (24)$$

The integrals with x^2y and xyz converge, while the integral with x^3 diverges logarithmically. Therefore, at $\Omega t \gg 1$,

$$\delta E(t) \simeq -\frac{\Delta}{\pi^2}\ln(\Omega t). \quad (25)$$

Thus, the two-loop quantum correction, though vanishing for a linear perturbation, leads to long-time memory effects near the points of discontinuity of $\partial\varphi/\partial t$.

5. PERIODIC CASE

Now, we turn to the case of periodic perturbations switched on at $t = 0$. To simplify calculations, we will consider first the simplest example of a monochromatic perturbation, $\varphi(t) = \theta(t)\sin\omega t$. Then, dynamic diffuson (12) acquires the form

$$D_\eta(t, t') = \theta(t - t')\exp\left\{-2\Gamma\sin^2\frac{\omega\eta}{2}\right.$$

$$\left.\times\left[t - t' + \frac{\sin\omega(t-t')}{\omega}\cos\omega(t + t')\right]\right\}. \quad (26)$$

It is convenient to calculate the two contributions to Eq. (21), $\delta W^{(ab)}(t)$ and $\delta W^{(c)}(t)$, separately. Making use of Eq. (26), we get

$$\delta W^{(ab)}(t) = -\frac{2\Gamma^2\Delta\omega^2}{\pi^2}\int_0^{x+y+z<t}dxdydz\,\mathscr{C}\mathscr{S}\mathscr{D}, \quad (27)$$

where

$$\mathscr{C} = \cos\omega(t - x - y - z)\cos\omega\left(t - \frac{x}{2} - \frac{y}{2}\right)$$

$$\times\cos\omega\left(t - \frac{x}{2} - \frac{z}{2}\right)\cos\omega\left(t - \frac{y}{2} - \frac{z}{2}\right),$$

$$\mathcal{S} = 3\sin^2\frac{\vartheta_x}{2} - \sin^2\frac{\vartheta_y}{2} - \sin^2\frac{\vartheta_z}{2} - 4\Gamma\sin\frac{\vartheta_x}{2}$$

$$\times \sin\frac{\vartheta_y}{2}\sin\frac{\vartheta_z}{2}(x\sin\vartheta_x + y\sin\vartheta_y + z\sin\vartheta_z),$$

$\mathcal{D}$ is the product of three diffusons in Eq. (21) evaluated at $\eta = 0$, and we introduced $\vartheta_x = y - z$, $\vartheta_y = -x - z$, and $\vartheta_z = x + y$.

The long-time behavior of Eq. (27) is determined by the vicinities of the *no-dephasing points* [11], where each of the three diffusons entering $\mathcal{D}$ is equal to 1. An analogous situation arises in the calculation of the one-loop quantum correction for the periodically driven orthogonal matrices [4], which is dominated by the no-dephasing points of a single dynamic cooperon. In the present case, the no-dephasing points are given by $(x, y, z) = (x, 2\pi m/\omega - x, 2\pi n/\omega - x)$ with arbitrary x and integer m and n.

In the limit $t \gg (\omega^{-1}, \Gamma^{-1})$, the no-dephasing points with different m and n do not overlap and the triple integral in Eq. (27) can be evaluated as

$$\int dxdydz \longrightarrow \int dx\sum_{mn}\int d\delta y d\delta z, \quad (28)$$

where we introduced $y = 2\pi m/\omega - x + \delta y$ and $z = 2\pi n/\omega - x + \delta z$. At the no-dephasing point, the factor $\mathcal{C}$ is nonzero, whereas the factor $\mathcal{S}$ vanishes and should be expanded in the deviations δy and δz:

$$\mathcal{C} = \cos^2\omega t\cos^2\omega(t + x), \quad (29)$$

$$\mathcal{S} = \frac{\omega^2}{4}(3(\delta y - \delta z)^2 - \delta z^2 - \delta y^2)$$

$$+ \frac{\Gamma\omega^4}{2}\delta y\delta z(\delta y - \delta z)[(x + z)dy - (x + y)\delta z]. \quad (30)$$

Though the last term of Eq. (30) is proportional to the fourth power of δy and δz, their smallness is compensated by an extra factor $x, y, z \sim t$. In the limit $t \gg (\omega^{-1}, \Gamma^{-1})$, we can integrate near the no-dephasing points in the Gaussian approximation, retaining only quadratic in the deviations terms in $\ln\mathcal{D}$:

$$\mathcal{D} = \exp\left\{-\frac{\Gamma\omega^2}{2}[x(\delta y - \delta z)^2 + y\delta z^2 + z\delta y^2]\right\}. \quad (31)$$

Weight (31) determines the correlators

$$M \equiv \begin{pmatrix} \langle\delta y\delta y\rangle & \langle\delta y\delta z\rangle \\ \langle\delta y\delta z\rangle & \langle\delta z\delta z\rangle \end{pmatrix}$$

$$= \frac{1}{\Gamma\omega^2}\frac{1}{xy + yz + zx}\begin{pmatrix} x + y & x \\ x & x + z \end{pmatrix}. \quad (32)$$

Substituting Eqs. (28)–(32) into Eq. (27) and integrating over δy and δz, one gets

$$\delta W^{(ab)}(t) = -\frac{\Gamma^2\Delta\omega^2}{\pi^2}\cos^2\omega t\int dx\sum_{mn}2\pi\sqrt{\det M}\langle\mathcal{S}\rangle, (33)$$

where we replaced $\cos^2\omega(t + x)$ by its average value $1/2$. The average $\langle\mathcal{S}\rangle$ is calculated with the help of the Wick's theorem using pair correlators (32):

$$\langle\mathcal{S}\rangle = \frac{3xyz}{2\Gamma(xy + yz + zx)^2}. \quad (34)$$

Finally, since the summand in Eq. (33) is a smooth function of m and n, it is possible to pass from summation over m and n back to integration over y and z:

$$\sum_{mn} \longrightarrow \left(\frac{\omega}{2\pi}\right)^2\int dydz. \quad (35)$$

As a result, we obtain

$$\delta W^{(ab)}(t) = -\frac{3\Delta\omega^2}{4\pi^3}\cos^2\omega t$$

$$\times \int_0^{x+y+z<t}\frac{xyzdxdydz}{(xy + yz + zx)^{5/2}}. \quad (36)$$

This integral is equal to $(2\pi/27)t$, and we get

$$\delta W^{(ab)}(t) = -\frac{\Delta\omega^2 t}{18\pi^2}\cos^2\omega t. \quad (37)$$

The contribution of diagram (c), $\delta W^{(c)}$, can be calculated analogously. Due to the same structure of the diffusons, its no-dephasing points coincide with the no-dephasing points for $\delta W^{(ab)}$. Instead of Eq. (33), one has now

$$\delta W^{(c)}(t) = \frac{\Gamma\Delta\omega^2}{4\pi^2}\frac{\partial}{\partial t}\int dx\sum_{mn}2\pi\sqrt{\det M}\langle\mathcal{S}'\rangle, \quad (38)$$

where

$$\langle\mathcal{S}'\rangle = 1 - \Gamma\omega^2\langle(\delta y - \delta z)[(x + z)dy - (x + y)\delta z]\rangle$$

$$= -\frac{yz}{xy + yz + zx}. \quad (39)$$

Passing from summation to integration according to Eq. (35) and utilizing the symmetry properties of the integrand, we obtain

$$\delta W^{(c)}(t) = -\frac{\Delta\omega^2}{24\pi^3}\frac{\partial}{\partial t}\int_0^{x+y+z<t}\frac{dxdydz}{\sqrt{xy + yz + zx}}. \quad (40)$$

The integral is equal to $(\pi/6)t^2$ yielding

$$\delta W^{(c)}(t) = -\frac{\Delta\omega^2 t}{72\pi^2}. \quad (41)$$

Note a peculiar property of Eqs. (37) and (41): $\delta W^{(ab)} \propto t(d\varphi/dt)^2$ and vanishes at the turning points of the perturbation, whereas $\delta W^{(c)}(t)$ is always positive, even when $d\varphi/dt = 0$. This means that they describe different mechanisms of absorption, with different memories on the past.

Combining Eqs. (37) and (41), we get the total two-loop correction to the quasi-classical absorption rate in the harmonic case,

$$\delta W(t) = -\frac{\Delta\omega^2 t}{72\pi^2}[4\cos^2\omega t + 1], \tag{42}$$

valid at $t \gg (\omega^{-1}, \Gamma^{-1})$.

The time-averaged correction grows linearly with the duration of the perturbation:

$$\overline{\delta W(t)} = -\frac{\Delta\omega^2 t}{24\pi^2}. \tag{43}$$

Remarkably, Eq. (43) holds not only for a harmonic perturbation but also for *an arbitrary periodic perturbation* with the period $2\pi/\omega$. Formally, this follows from the fact that the level sensitivity Γ to the external perturbation drops from Eq. (43). Then, according to Eq. (35), the factor ω^2 in Eq. (43) measures the inverse time separation between the no-dephasing points, which is the same for all periodic perturbations of a given period.

6. DYNAMIC VERSUS ANDERSON LOCALIZATION

It is useful to compare two-loop result (43) for a harmonic perturbation with the corresponding one-loop expression for the GOE obtained in [4]:

$$\frac{\overline{\delta W(t)}}{\overline{W_0}} = -\begin{cases} \sqrt{\dfrac{t}{t_*}}, & \text{GOE,} \\[2mm] \dfrac{\pi t}{24 t_*}, & \text{GUE,} \end{cases} \tag{44}$$

where $\overline{W_0} = \pi\Gamma\omega^2/2\Delta$ is the period-averaged absorption rate and $t_* = \pi^2\Gamma/2\Delta^2$ is the localization time.

In [4], we pointed out that the weak dynamic localization correction to the energy absorption rate of a periodically driven GOE has the same square-root behavior as the weak Anderson localization correction to the conductivity of a quasi-one-dimensional (1D) disordered wire. Now, we see that the same is true for the case of the GUE as well: in both cases, the correction is linear in time and dephasing time, respectively. Therefore, it is tempting to suggest that this analogy is not a coincidence but has its roots in equivalence between the dynamic localization for the RMT driven by a harmonic perturbation and 1D Anderson localization.

Such an equivalence is known for the case of kicked quantum rotor (KQR): in the long time limit, the KQR problem can be mapped [12] onto the 1D σ model. On the other hand, the problems of the δ-kicked KQR and of the periodically driven RMT are, to some extent, complementary. Both of them can be mapped on a tight-binding 1D model but with very different structure of couplings between the sites and auxiliary orbitals [4]. In particular, the "kicked RMT" model with $\varphi(t)$ being a periodic δ function does not exhibit dynamic localization whatsoever [4].

In order to check the assumption about the equivalence of the driven RMT to the quasi-1D disordered wire, we use the simple relationship between the time-dependent energy absorption rate $W(t)$ in the dynamic problem and the frequency-dependent diffusion coefficient $D(\omega)$ in the Anderson model [13]:

$$\frac{W(t)}{W_0} = \int\limits_{-\infty}^{+\infty}\frac{d\omega}{2\pi}\frac{e^{-i\omega t}}{-i\omega + 0}\frac{D(\omega)}{D_0}, \tag{45}$$

where W_0 and D_0 are the classical period-averaged absorption rate and diffusion coefficient. $D(\omega)$ is known from the theory of weak Anderson localization:

$$\frac{\delta D(\omega)}{D_0} = \begin{cases} -\dfrac{1}{\sqrt{-i\omega t_{loc}}}, & \text{GOE,} \\[3mm] \dfrac{1}{6i\omega t_{loc}}, & \text{GUE,} \end{cases} \tag{46}$$

here, $t_{loc} = (2\pi\nu_1)^2 D_0$ and ν_1 is the 1D density of states. Then, Eqs. (46) and (45) give *two* expressions similar to Eq. (44) with only *one* fitting parameter t_*/t_{loc}. One can easily see that, with the choice $t_*/t_{loc} = \pi/4$, *both* numerical coefficients match exactly.

We believe that there are deep reasons for this coincidence and make a *conjecture* that the (period-averaged) dynamics of the harmonically driven RMT at time scales $t \gg (\omega^{-1}, \Gamma^{-1})$ is equivalent to the density propagation in a quasi-1D disordered wire. Employing this equivalence, we can easily calculate the energy absorption rate in the regime of well-developed dynamic localization at $t \gg t_*$ using the Mott–Berezinsky asymptotics of the AC conductivity, $\sigma(\omega) \propto \omega^2\ln^2(1/\omega)$ [14, 15]. Substituting $D(\omega) \propto \sigma(\omega)$ into Eq. (45), we find that, in the localized regime, $W(t)$ decays as

$$W(t) \propto \frac{\ln t}{t^2}, \quad t \gg t_*. \tag{47}$$

This dependence is not directly related to the spatial dependence of the localized wave functions, which is exponential in the Anderson model. It can be seen if one considers the density–density correlator [disorder-averaged product of the retarded and advanced Green's

functions $G^R(x, x', \epsilon + \omega)G^A(x' x, \epsilon)$, whose Fourier transform can be conveniently represented as $2\pi\nu_1 A(k, \omega)/(-i\omega)$. According to Gorkov's criterion of localization [16], $A(k, 0)$ is finite and its Fourier transform determines the spatial decay of localized wave functions. On the other hand, $D(\omega)$ can be extracted from the density–density correlator as

$$D(\omega) = \frac{i\omega}{2}\frac{\partial^2}{\partial k^2}A(k, \omega)\bigg|_{k=0}, \qquad (48)$$

and, according to our *conjecture*, should be substituted in Eq. (45) to give the absorption rate. Thus, instead of $A(k, \omega = 0)$, usually studied in the Anderson localization problem, $W(t)$ is determined by the ω dependence of $\partial^2 A(k, \omega)/\partial k^2$ at $k = 0$, which, to the best of our knowledge, evaded investigation in the framework of the quasi-1D nonlinear sigma model.

7. CONCLUSIONS

We derived the general expression for the lowest-order (two-loop) interference correction to the energy absorption rate of a parametrically driven GUE. If an external perturbation grows linearly with time, the first correction vanishes. For a periodic perturbation, the averaged correction $\delta W(t) \propto t$. We make a *conjecture* that the dynamics of the harmonically driven RMT at the time scales $t \gg 1/\omega, 1/\Gamma$ is equivalent to the 1D Anderson model. Based on this equivalence, we predict that, in the regime of strong dynamic localization, $W(t) \propto \ln(t)/t^2$.

REFERENCES

1. M. G. Vavilov and I. L. Aleiner, Phys. Rev. B **60**, R16311 (1999); Phys. Rev. B **64**, 085115 (2001); M. G. Vavilov, I. L. Aleiner, and V. Ambegaokar, Phys. Rev. B **63**, 195313 (2001).

2. V. I. Yudson, E. Kanzieper, and V. E. Kravtsov, Phys. Rev. B **64**, 045310 (2001).

3. M. A. Skvortsov, Phys. Rev. B **68**, 041306(R) (2003).

4. D. M. Basko, M. A. Skvortsov, and V. E. Kravtsov, Phys. Rev. Lett. **90**, 096801 (2003).

5. K. B. Efetov, *Supersymmetry in Disorder and Chaos* (Cambridge Univ. Press, New York, 1997).

6. V. E. Kravtsov, cond-mat/0312316.

7. M. Wilkinson, J. Phys. A: Math. Gen. **21**, 4021 (1988).

8. B. D. Simons and B. L. Altshuler, Phys. Rev. B **48**, 5422 (1993).

9. G. D. Mahan, *Many-Particle Physics*, 3rd ed. (Kluwer Academic, Boston, 2000).

10. G. Casati, B. V. Chirikov, J. Ford, and F. M. Izrailev, in *Stochastic Behaviour in Classical and Quantum Hamiltonian Systems*, Ed. by G. Casati and J. Ford (Springer, Berlin, 1979), Lect. Notes Phys., Vol. 93.

11. X.-B. Wang and V. E. Kravtsov, Phys. Rev. B **64**, 033313 (2001).

12. A. Altland and M. R. Zirnbauer, Phys. Rev. Lett. **77**, 4536 (1996).

13. A. Altland, Phys. Rev. Lett. **71**, 69 (1993); C. Tian, A. Kamenev, and A. Larkin, cond-mat/0403482; Although in these works Eq. (46) was applied to the KQR, its validity is not restricted just by the KQR case.

14. N. F. Mott, Philos. Mag. **17**, 1259 (1968).

15. V. L. Berezinskii, Zh. Éksp. Teor. Fiz. **65**, 1251 (1973) [Sov. Phys. JETP **38**, 620 (1974)].

16. V. L. Berezinskii and L. P. Gor'kov, Zh. Éksp. Teor. Fiz. **77**, 2498 (1979) [Sov. Phys. JETP **50**, 1209 (1979)].

Continuous-Time Quantum Monte Carlo Method for Fermions: Beyond Auxiliary Field Framework[¶]

A. N. Rubtsov[1] and A. I. Lichtenstein[2]

[1] *Department of Physics, Moscow State University, Moscow, 119992 Russia*
[2] *Institute of Theoretical Physics, University of Hamburg, 20355 Hamburg, Germany*
e-mail: alex@shg.ru; alichten@physnet.uni-hamburg.de
Received May 23, 2004

A numerically exact continuous-time quantum Monte Carlo algorithm for finite fermionic systems with nonlocal interactions is proposed. The scheme is particularly applicable for general multiband time-dependent correlations, since it does not invoke Hubbard–Stratonovich transformation. The present determinantal grand-canonical method is based on a stochastic series expansion for the partition function in the interaction representation. The results for the Green function and for the time-dependent susceptibility of multiorbital supersymmetric impurity model with a spin-flip interaction are presented. © 2004 MAIK "Nauka/Interperiodica".

PACS numbers: 71.10.Fd; 71.27.+a; 02.70.Ss

Quantum Monte Carlo (QMC) tools for fermionic systems appeared more than 20 years ago [1–4] and are nowadays vital for a wide range of fields, like the physics of correlated materials, quantum chemistry, and nanoelectronics. Although the first programs were developed for model Hamiltonians with local interaction, many-particle action of a very general form stays behind the real systems. For example, all matrix elements of the interaction do not vanish in the problems of quantum chemistry [5] and solid-state physics [6]. Dynamical mean-field theory (DMFT) [7] for correlated materials brings a nontrivial bath Green function to the scene, and its extension [8] deals with an interaction which is nonlocal in time. An off-diagonal exchange term can be responsible for the correlated superconductivity in doped fullerens [9]. It is worth noting in general that exchange is often of an indirect origin (like superexchange) and the exchange terms are therefore retarded. New developments [10] clearly urge the invention of an essentially different type of QMC scheme suitable for nonlocal, time-dependent interaction.

The determinantal grand-canonical auxiliary-field scheme [1–4] is commonly used for the interacting fermions, because other known QMC schemes (like stochastic series expansion in powers of Hamiltonian [11] or worm algorithms [12]) suffer an unacceptably bad sign problem for this case. Two points are essential for the approach: first, the imaginary time is artificially discretized, and then, the Hubbard–Stratonovich transformation [13] is performed to decouple the fermionic degrees of freedom. After the decoupling, fermions can be integrated out and Monte Carlo sampling should be performed in the space of auxiliary Hubbard–Stratonovich fields. Hirsh [3] proposed to use discrete Hubbard–Stratonovich transformation to improve the original scheme; this is now a standard method for simulations of lattice and impurity quantum problems. For relatively small clusters, and, in particular, for DMFT, the sign problem is not crucial in this method [14]. The number of auxiliary field is linear (quadratic) in the number of atoms for the case of local (nonlocal) interaction.

The time discretization leads in a systematic error of the result. For bosonic quantum systems, continuous-time loop algorithm [15], worm diagrammatic world line Monte Carlo scheme [12], and continuous-time path-integral QMC [16] overcame this issue. Recently, a continuous-time modification of the fermionic QMC algorithm was proposed [17]. It is based on a series expansion for the partition function in the powers of interaction. The scheme is free of time-discretization errors, but the Hubbard–Stratonovich transformation is still invoked. Therefore, the number of auxiliary fields scales similarly to the discrete scheme. This scheme is developed for local interaction only.

Besides the time-discretization problem, the nonlocality of interaction hampers the calculation in the existing schemes, because it is hard to simulate systems with a large number of auxiliary spins. Further, the discrete Hubbard–Stratonovich transformation is not suitable for interactions nonlocal in time. One needs to use continuous dispersive bosonic fields [8] for this case, which makes the simulation even harder.

In this letter, we present a novel numerically exact continuous-time fermionic QMC algorithm. This is the first QMC scheme that does not invoke any type of Hubbard–Stratonovich transformations and, therefore,

---

[¶] This article was submitted by the authors in English.

operates natively with nonlocal in space and time interactions. The scheme is free of systematic errors due to direct operations with continuous-time expansion of the partition function. Numerical results for a super-symmetric two-band impurity model with spin flip, time-dependent nonlocal interactions show an advantage and a broad perspective of the proposed QMC scheme for the complex solid-state and quantum-chemistry problems.

We consider a fermion system with pair interaction in the most general form and present the partition function $Z = \mathrm{Tr}\{T \exp(-S)\}$ in terms of the effective action S:

$$
\begin{aligned}
S &= S_0 + W \equiv \iint t_r^{r'} c_{r'}^\dagger c^r dr dr' \\
&+ \iiiint w_{r_1 r_2}^{r_1' r_2'} (c_{r_1'}^\dagger - \alpha_{r_1'}^{r_1})(c_{r_2'}^\dagger c^{r_2} - \alpha_{r_2'}^{r_2}) dr_1 dr_1' dr_2 dr_2'.
\end{aligned}
\tag{1}
$$

Here, T is a time-ordering operator, $r = \{i, s, \tau\}$ is a combination of the discrete index i numbering the single-particle states in a lattice, spin index $s = \uparrow$ or $\downarrow$, and the continuous imaginary-time variable τ. Integration over dr implies the integral over $d\tau$ and the sum over all lattice states and spin projections: $\int dr \equiv \sum_i \sum_s \int_0^\beta d\tau$. We borrow the linear-algebra style for sub- and super-scripts to make the notation clearer. The creation $(c_r^\dagger)$ and annihilation (c^r) operators for a fermion in the state r are labeled as covariant and contravariant vectors, respectively. The labeling for coefficients t and w is chosen to present all integrands like scalar products of tensors. An additional quantity $\alpha_{r'}^r$ is introduced for the most effective splitting of S to the Gaussian part (S_0) and interaction (W). The parameters $\alpha_{r'}^r$ are to be chosen later to optimize the algorithm and to minimize the sign problem.

We consider S_0 as an unperturbed action and switch to the interaction representation. The perturbation-series expansion for Z has the following form:

$$
\begin{aligned}
Z &= \sum_{k=0}^\infty \int dr_1 \int dr_1' \ldots \int dr_{2k}' \Omega_k(r_1, r_1', \ldots, r_{2k}'), \\
\Omega_k &= Z_0 \frac{(-1)^k}{k!} w_{r_1 r_2}^{r_1' r_2'} \cdot \ldots \cdot w_{r_{2k-1} r_{2k}}^{r_{2k-1}' r_{2k}'} D_{r_1' r_2' \ldots r_{2k}'}^{r_1 r_2 \ldots r_{2k}},
\end{aligned}
\tag{2}
$$

where Z_0 is a partition function for the unperturbed system and

$$
D_{r_1 \ldots r_{2k}}^{r_1 \ldots r_{2k}} = \langle T(c_{r_1}^\dagger c^{r_1} - \alpha_{r_1}^{r_1}) \cdot \ldots \cdot (c_{r_{2k}}^\dagger c^{r_{2k}} - \alpha_{r_{2k}}^{r_{2k}}) \rangle. \tag{3}
$$

Hereafter, the triangle brackets denote the average over the unperturbed system, $\langle A \rangle = Z_0^{-1} \mathrm{Tr}\{T A \exp(-S_0)\}$. Since the action S_0 is Gaussian, one can apply the Wick

theorem and find the expression for D in terms of a determinant of a $2k \times 2k$ matrix:

$$
D_{r_1' r_2' \ldots r_{2k}'}^{r_1 r_2 \ldots r_{2k}} = \det \left\| g_{r_j'}^{r_i} - \delta_{ij} \alpha_{r_j'}^{r_i} \right\|. \tag{4}
$$

Here, $g_{r'}^r = \langle T c_{r'}^\dagger c^r \rangle$ is the single-particle two-point Green function in the QMC notation and δ_{ij} is a delta symbol.

In the following, we use an important-sampling Markov process in the configuration space, where the points are determined by the perturbation order k and the set $\{r_1, r_1', \ldots, r_{2k}'\}$. Suppose for a moment that Ω is always positive, and consider a random walk with a probability of $Z^{-1} \Omega_k(r_1, r_1', \ldots, r_{2k}, r_{2k}')$ of visiting each point. Denote the average over this random walk by the overbar. Then, for example, the Green function $G_{r'}^r = Z^{-1} \langle T c_{r'}^\dagger c^r e^{-W} \rangle$ can be expressed as $\overline{g_{r'}^r(r_1, r_1', \ldots, r_{2k}')}$, where $g_{r'}^r$ determines the Green function for a current realization. It is important to note that a Fourier transform of $g_{r'}^r$ with respect to time arguments can be found analytically. Therefore, the Green function can be calculated directly at Matsubara frequencies. Such an approach has an advantage over the calculation in τ domain, because it automatically takes into account the invariance of the initial action in the translations along the τ axis. Higher-order correlators can be calculated in the same way. A more detailed description of the algorithm, as well as a methodological discussion, can be found in [18].

In certain cases, proper choice of α can indeed completely suppress the sign problem. For example, for the Hubbard model, it is reasonable to choose $\alpha_{i's't'}^{ist} = \alpha_s \delta_{\tau\tau'} \delta_{ij} \delta_{ss'}$. If the Gaussian part of the action does not rotate spins, then $g_{s'}^s \propto \delta_{ss'}$, and the determinant in (4) is factorized: $D = D_\uparrow D_\downarrow$. For the case of the Hubbard model with attraction, one should choose $\alpha_\uparrow = \alpha_\downarrow = \alpha$, where α is real. For this choice, $g_\downarrow^\downarrow = g_\uparrow^\uparrow$ and, consequently, $D_\uparrow = D_\downarrow$. All terms are positive in this case, because $w < 0$.

The choice of $\alpha_\uparrow = \alpha_\downarrow$ is useless for a system with repulsion, because the alternating signs of Ω_k with odd and even k appear [19]. Similarly to the discrete Hubbard–Stratonovich transformations [4], the particle–hole symmetry can be exploited for a half-filled system. One can show that the choice $\alpha_\uparrow = 1 - \alpha_\downarrow = \alpha$ delivers the condition $D_\uparrow = -D_\downarrow$ for this case, thus eliminating the sign problem [18]. Further, for the particular case of an impurity problem in the atomic limit $\alpha_\uparrow = 1 - \alpha_\downarrow = \alpha$ with $\alpha > 1$ or $\alpha < 0$, the sign problem is eliminated for the repulsive interaction at any filling factor [18].

Summarizing these observations, we can write a draft recipe of how to choose α. For a physically reasonable split of the action 1, the value of α should not be too large. Therefore, for the diagonal repulsive terms of the interaction matrix, we propose to use $\alpha_\uparrow = 1 - \alpha_\downarrow = \alpha$ with α slightly above 1. For the attractive interaction, and for the off-diagonal matrix elements of w, the choice should be $\alpha_\uparrow = \alpha_\downarrow \approx 0.5$. Of course, in a general case, Ω is not positive-defined and one needs to work with its absolute value in QMC sampling. In this case, an exponential fall-off occurs for large systems or small temperature. It is worthwhile to mention that an above choice of parameters α suppresses the sign problem for local DMFT-like action with a diagonal in orbital indices bath Green function.

Now, we discuss how to organize a random walk in practice. We need to perform a random walk in the space of k; $r_1, r_1', \ldots, r_{2k}'$. Two kinds of trial steps are necessary: one should try to either increase or decrease k by 1 and, respectively, add or remove the four corresponding operators. A proposition for r_{2k+1}, r_{2k+1}', r_{2k+2}, r_{2k+2}' should be generated for the "incremental" step. The normalized modulus

$$\|w\|^{-1} \left| w_{r_{2k+1} r_{2k+2}}^{r_{2k+1}' r_{2k+2}'} \right|,$$
$$\|w\| = \iiiint \left| w_{rR}^{r'R'} \right| dr\,dR\,dr'\,dR', \tag{5}$$

can be used as a probability density for this proposition. Then, the standard Metropolis acceptance criterion can be constructed using the ratio

$$\frac{\|w\|}{k+1} \left| \frac{D_{r_1' \ldots r_{2k+2}'}^{r_1 \ldots r_{2k+2}}}{D_{r_1' \ldots r_{2k}'}^{r_1 \ldots r_{2k}}} \right|. \tag{6}$$

The "decremental" step can be organized in the same way.

The most time-consuming operation of the algorithm is the calculation of the ratio of determinants, defined by Eq. (4). A fast update trick can be used, resulting in $\propto k^2$ operations [1, 4]. Here, we estimate k. The average value of (6) determines the acceptance rate for QMC sampling. It is reasonable to expect that, in order of magnitude, this rate is not much lower than unity. The ratio of determinant times $\|w\|$ can be interpreted as the expectation value for $|W|$. Therefore,

$$k \approx \overline{|W|}. \tag{7}$$

For the Hubbard lattice of N atoms with an interaction constant U, for instance, $|W| \propto \beta |U| N$. In principle, one can manipulate α to minimize $\overline{|W|}$. These manipulations should, however, preserve the average sign as large as possible. We apply the proposed continuous-time QMC for the important problem of supersymmetric two-band impurity model at half-filling [20, 21]. To our knowledge, this is the first successful attempt to
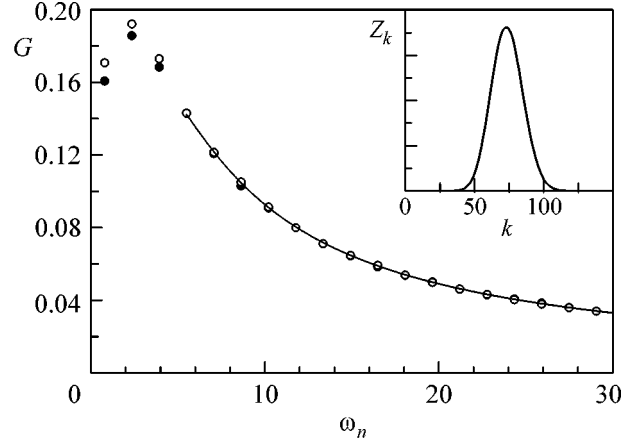

Fig. 1. Local Green function of the two-band rotationally invariant model at the Matsubara frequencies. Filled and open circles correspond to the static and to the spin flip nonlocal in time, respectively. High-frequency asymptotics is drawn with the line. Inset shows the distribution function for the perturbation order k.

take the off-diagonal exchange terms of this model into account. These terms are important for the realistic study of the multiband Kondo problem, because they are responsible for the local moment formation [20]. The interaction in this model has the following form:

$$\frac{U}{2}(\hat{N}(\tau) - 2)(\hat{N}(\tau) - 2)$$
$$- \frac{J}{2}(\mathbf{S}(\tau) \cdot \mathbf{S}(\tau) + \mathbf{L}(\tau) \cdot \mathbf{L}(\tau)), \tag{8}$$

where $\hat{N}$ is the operator of total number and S and L are total spin and orbital-momentum operators, respectively. The interaction is spin- and orbital-rotationally invariant. The Gaussian part of the action represents the diagonal semicircular density of states [7] with unitary half-band width: $t(\omega) = 2/(\omega_n + \sqrt{\omega_n^2 - 1})$, where ω_n are Matsubara frequencies related to the imaginary time variable. We used the parameters $U = 4$, $J = 1$ at $\beta = 4$. A modification of this model was also studied in which spin-flip operators were replaced with terms fully nonlocal in time. For example, the operator $c_{0\uparrow\tau}^\dagger c^{0\downarrow\tau} c_{1\downarrow\tau}^\dagger c^{1\uparrow\tau}$ was replaced with $\beta^{-1} \int d\tau' \, c_{0\uparrow\tau}^\dagger c^{0\downarrow\tau} c_{1\downarrow\tau'}^\dagger c^{1\uparrow\tau}$. The figures present the result for the local Green function G_{is}^{is} and the four-point correlator $\chi(\tau - \tau') = \langle c_{0\uparrow\tau}^\dagger c^{0\downarrow\tau} c_{1\downarrow\tau'}^\dagger c^{1\uparrow\tau} \rangle$. The latter quantity characterizes the spin–spin correlations and would vanish if the exchange were absent.

Figure 1 shows the Green function at Matsubara frequencies. The typical number of QMC trials was 2×10^7. Results for the spin flip local and nonlocal in time are shown with filled and open circles, respectively. The
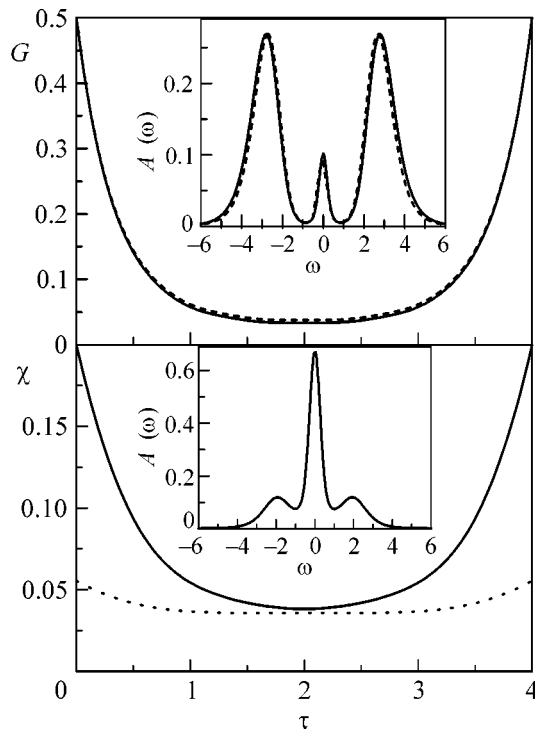
Fig. 2. Imaginary-time Green function (upper panel) and the four-point correlator χ (lower panel) for the two-band model. Upper inset shows DOS computed from the Green function. Solid and dotted lines correspond to the static spin flip and that nonlocal in time, respectively. Lower inset shows DOS for five-band model with the same value of U and $J = 0.2$.

distribution function for the perturbation order k is drawn in the inset. For the system studied, it appears to be a Gaussian-like peak located at $k \approx 75$, in accordance with Eq. (7). The estimated error bar in $G(\omega_n)$ is about 3×10^{-3} for the lowest frequency and becomes smaller as the frequency increases. The high-frequency tail obeys an asymptotic behavior, $-\mathrm{Im}(iw + \epsilon)^{-1}$ with $\epsilon \approx 2.9$.

Green function in the time domain was obtained by a numerical Fourier transform from the data for $G(\omega_n)$. For high harmonics, the aforementioned asymptotic was used. Results are presented in the upper panel of Fig. 2. The lower panel presents the result for $\chi(\tau)$. These data are obtained similarly, the difference being that $\chi(\omega)$ is defined at Bose Matsubara frequencies and obeys a $1/\omega^2$ decay. It is interesting to note that the Green function is almost insensitive to the details of spin-flip retardation. Both Green functions are very similar and correspond to qualitatively the same density of states (DOS). The maximum-entropy guess for DOS is presented in the inset of Fig. 2. On the other hand, switch to the exchange nonlocal in time modifies $\chi(\tau)$ dramatically. The exchange local in time results in a pronounced peak of $\chi(\tau)$ at $\tau \approx 0$, whereas the nonlocal spin flip results in almost time-independent spin–spin

correlations. For the realistic description of Kondo impurities like a cobalt atom on a metallic surface, it is of crucial importance to use the spin and orbital rotationally invariant Coulomb vertex in the nonperturbative investigation of electronic structure. The proposed continuous-time QMC scheme is easily generalized for the general multiband case. As an example, we show the DOS for the five d-orbital model at half-filling for the same value of U and $J = 0.2$ in the lower inset of Fig. 2.

For a final discussion, it is suitable to analyze the convergence of series (2). Fermi statistics and the finite size of the system ensure that the configurational space of the problem is of a finite order. Because the perturbation operator W has a finite norm, its powers W^k therefore grow slower than $k!$ Consequently, from the mathematical point of view, there is no doubt that series (2) always converges. Physically, it is important to note that this convergence is related both with the choice of the type of serial expansion and with the peculiarities of the system under study. First of all, series (2) contains *all* diagrams, including unbounded. In the analytical diagram-series expansion, unbounded diagrams drop out from the calculation [22], and the convergence radius for the diagram-series expansion differs from that of (2). Further, Fermi statistics is indeed important. An analogue of (2) for Bose field can diverge even for a single-atom problem [22], because in this case one deals with an infinite-order Gilbert space. It is important to keep this in mind for possible extensions of the algorithm to the electron–phonon systems and to the field models, as these systems are also characterized by an infinite-order phase space. A general time-dependent form of the action (Eq. (1)) allowed us to use renormalization theory for a Hubbard-like model: in this case, local DMFT would be a starting point for lattice calculations in order to reduce the effective interaction and minimize the sign problem.

In conclusion, we have developed a fermionic continuous-time quantum Monte Carlo method for general interactions nonlocal in space and time. We demonstrated that, for Hubbard-type models, the computational time for a single trial step scales similarly to that for the schemes based on a Stratonovich transformation. An important difference occurs, however, for the nonlocal interactions. Consider, for example, a system with a large Hubbard U and much smaller but still important Coulomb interatomic interaction. One needs to introduce N^2 auxiliary fields per time slice instead of N to take the long-range forces into account. On the other hand, the complexity of the present algorithm should remain almost the same as for the local interactions, because $\overline{|W|}$ does not change much. This should be useful for the realistic cluster DMFT calculations and for the applications to quantum chemistry [5]. It is also possible to study the interactions retarded in time, particularly the superexchange and the effects related to dissipation. This was demonstrated for the important

case of the fully rotationally invariant two-band model and its extension with spin-flip terms nonlocal in time.

REFERENCES

1. D. J. Scalapino and R. L. Sugar, Phys. Rev. Lett. **46**, 519 (1981).

2. R. Blankenbecler, D. J. Scalapino, and R. L. Sugar, Phys. Rev. D **24**, 2278 (1981).

3. J. E. Hirsch, Phys. Rev. B **28**, 4059 (1983).

4. J. E. Hirsch, Phys. Rev. B **31**, 4403 (1985).

5. S. R. White, J. Chem. Phys. **117**, 7472 (2002).

6. S. W. Zhang and H. Krakauer, Phys. Rev. Lett. **90**, 136401 (2003).

7. A. Georges, G. Kotliar, W. Krauth, and M. J. Rozenberg, Rev. Mod. Phys. **68**, 13 (1996).

8. P. Sun and G. Kotliar, Phys. Rev. B **66**, 085120 (2002).

9. M. Capone, M. Fabrizio, C. Castellani, and E. Tosatti, Science **296**, 2364 (2002).

10. S. Y. Savrasov, G. Kotliar, and E. Abrahams, Nature **410**, 793 (2001).

11. A. W. Sandvik and J. Kurkijarvi, Phys. Rev. B **43**, 5950 (1991).

12. N. V. Prokof'ev, B. V. Svistunov, and I. S. Tupitsyn, Pis'ma Zh. Éksp. Teor. Fiz. **64**, 853 (1996) [JETP Lett. **64**, 911 (1996)].

13. J. Hubbard, Phys. Rev. Lett. **3**, 77 (1959); R. L. Stratonovich, Dokl. Akad. Nauk SSSR **115**, 1097 (1957) [Sov. Phys. Dokl. **2**, 416 (1958)].

14. M. Jarrell, T. Maier, C. Huscroft, and S. Moukouri, Phys. Rev. B **64**, 195130 (2001).

15. B. B. Beard and U.-J. Wiese, Phys. Rev. Lett. **77**, 5130 (1996).

16. P. E. Kornilovitch, Phys. Rev. Lett. **81**, 5382 (1998).

17. S. M. A. Rombouts, K. Heyde, and N. Jachowicz, Phys. Rev. Lett. **82**, 4155 (1999).

18. A. N. Rubtsov, cond-mat/0302228.

19. G. G. Batrouni and P. de Forcrand, Phys. Rev. B **48**, 589 (1993).

20. L. Dworin and A. Narath, Phys. Rev. Lett. **1287**, 25 (1970).

21. M. J. Rozenberg, Phys. Rev. B **55**, R4855 (1997).

22. C. Itzykson and J. B. Zuber, *Introduction to Quantum Field Theory* (McGraw-Hill, New York, 1980; Mir, Moscow, 1984).

Observation of the Production of Cumulative Particles in Nucleus–Nucleus and Neutrino–Nucleus Interactions

V. V. Dubinina, N. P. Egorenkova, V. I. Krotkova, E. A. Pozharova, and V. A. Smirnitskiĭ

Institute of Theoretical and Experimental Physics, ul. Bol'shaya Cheremushkinskaya 25, Moscow, 117218 Russia

Received May 31, 2004

Experimental data on the emission of cumulative particles arising in the interaction of 2.5-GeV/c ^{56}Fe nuclei (FeEm) and 10–200 GeV neutrinos (νEm) with photoemulsion nuclei are analyzed. The number of cumulative particles correlates with the emission of secondary charged particles in the (FeEm) and (νEm) interactions. © 2004 MAIK "Nauka/Interperiodica".

PACS numbers: 25.75.Dw; 25.30.Pt

What can be common in such different interactions as nucleus–nucleus and neutrino–nucleus interactions, besides the fact of the production of cumulative particles? In this paper, we show that some phenomena are inherent in both nucleus–nucleus and neutrino–nucleus interactions.

The cumulative effect in the hadron interactions with nuclei consists in the observation of particles whose production on a free nucleon is forbidden by the kinematics of nuclear reactions. To date, this phenomenon is least studied in nucleus–nucleus and neutrino–nucleus interactions [1–3].

We studied the production of cumulative particles in experiment on measurements of azimuthal anisotropy in the interaction of ^{56}Fe nuclei with photoemulsion nuclei (FeEm) [4]. The details of selection of the (FeEm) events are reported in this paper.

The search for and measurements of the cumulative particles were carried out in the angular range $90° < \theta < 180°$ with respect to the momentum of a projectile nucleus. Relativistic singly charged particles (s particles) were selected with the ionization corresponding to $\beta > 0.7$ and g particles were selected with the mean free paths $R \geq 3.0$ mm in emulsion and $\beta \leq 0.7$. Particle emission angles were determined by measuring the grain coordinates on the particle traces. An accompaniment program ensured the necessary dialogue between the operator and computer, which provides the on-line control over the measurement results. The accuracy of angular measurements of singly charged particles was equal to $\cong 1$ mrad. Cumulative singly charged particles were observed in (40 ± 5)% of (FeEm) interactions.

It was of interest to analyze the joint production of cumulative particles with b, g, s, and f particles emitted forward ($0° < \theta < 90°$) in nucleus–nucleus (FeEm) interactions and to compare the results with similar data published in [3], where we studied neutrino–nucleus (νEm) interactions. According to the photoemulsion

technique [5], slow fragments of a target nucleus with the proton kinetic energy $T_p \leq 26$ MeV (mean free path in emulsion $R \leq 3$ mm) and $\beta \leq 0.23$ belong to b particles. These are primarily the evaporation protons. Fast singly charged particles from the target nucleus with the proton kinetic energy 26 MeV $< T_p \leq 400$ MeV, relative ionization $I/I_0 > 1.4$ (I_0 is the ionization density of singly charged relativistic particles), and velocity $0.23 < \beta \leq 0.7$ belong to g particles. Particles with relative ionization $I/I_0 < 1.4$ and $\beta > 0.7$, which corresponds to $T_p > 400$ MeV, belong to s particles, among which are pions, interacting projectile-nucleus protons, and singly charged particles from the target nucleus. Relativistic multiply ($Z \geq 2$) and singly charged particles emitted within the fragmentation cone [5].

All measured (FeEm) interactions were divided into three groups. The first group is free of cumulative particles, the second group has only one cumulative particle, and the third group has two or more cumulative particles. The average multiplicities of b, g, s, and f particles were measured in each group of particles.

Due to the use of nuclear photoemulsion, correlation can be observed between the number of cumulative particles and average multiplicities of forward-emitted b, g, s, and f particles. The figure shows the results of our measurements and the data on neutrino–nucleus interactions. As is seen in the figure, the number of cumulative particles correlates with the average multiplicities of b and g particles in nucleus–nucleus and neutrino–nucleus interactions. It is known that nucleus–nucleus interactions are characterized by the multiplicity of g particles. This is a possible cause of an increase in the number of cumulative particles with $\langle N_g \rangle$. In this case, the proton jet must form into hadrons inside a nucleus. With an increase in the neutrino energy, the formation length increases, which reduces the contribution of secondary interactions and, correspondingly, the yields of cumulative particles [3]. The number of cumulative
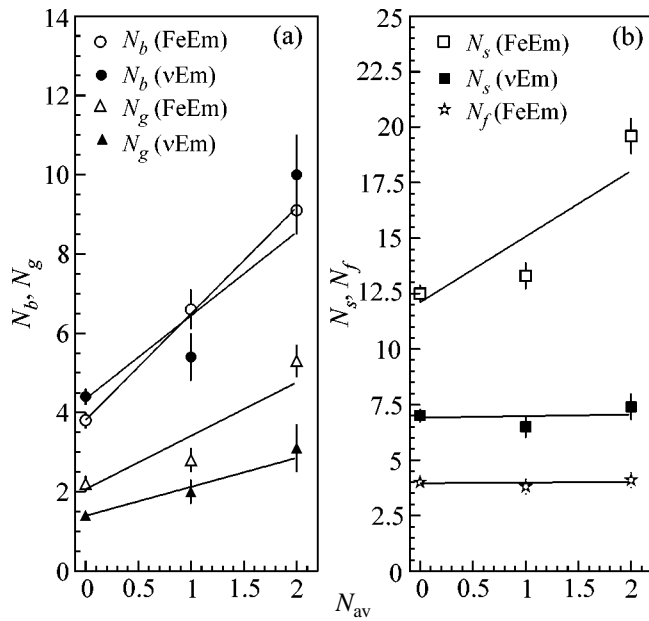
Number of cumulative particles N_{av} vs. average multiplicities of the b, g, s, and f particles in nucleus–nucleus and neutrino–nucleus interactions. The straight lines are the linear fits.

particles produced in (νEm) interactions does not correlate with the average multiplicity of s particles. This is likely associated with the fact that a neutrino interacts only once with nuclear nucleons and the resulting proton jet is not responsible for the production of cumulative particles. Their production is most likely associated with the reaction of the residual target nucleus on the (νEm) interaction. In nucleus–nucleus interactions, the average multiplicity of s particles depends on the impact parameter [6]. In the central and semicentral interactions, collision involves many nucleons of the projectile nucleus, leading to a large multiplicity of all secondary particles, including cumulative particles. The emission of f particles (fragments) accompanies the decay of a projectile nucleus and bears no relation to the production of cumulative particles in the (FeEm) interaction.

REFERENCES

1. S. Nagamiya, M. C. Lamaire, E. Moeller, *et al.*, Phys. Rev. C **24**, 971 (1981).
2. A. A. Ivanov, V. I. Konyushko, V. M. Korablev, *et al.*, Pis'ma Zh. Éksp. Teor. Fiz. **30**, 390 (1979) [JETP Lett. **30**, 362 (1979)].
3. R. Ammar, A. Bakich, T. Barnet, *et al.*, Pis'ma Zh. Éksp. Teor. Fiz. **49**, 189 (1989) [JETP Lett. **49**, 219 (1989)].
4. V. V. Dubinina, N. P. Egorenkova, V. I. Krotkova, *et al.*, Yad. Fiz. **67** (3), 1 (2004) [Phys. At. Nucl. **67**, 518 (2004)].
5. C. F. Powell, P. H. Fowler, and D. H. Perkins, *The Study of Elementary Particles by the Photographic Method* (Pergamon, London, 1959; Inostrannaya Literatura, Moscow, 1962).
6. P. L. Jain, G. Singh, and A. Mukhopadhyay, Phys. Rev. Lett. **74**, 1534 (1995).

Translated by R. Tyapaev

Experimental Search for the Effect of Resonant Environment on the Mössbauer Absorption of Gamma Rays by ^{57}Fe

V. G. Alpatov[1], Yu. D. Bayukov[1], A. V. Davydov[1], Yu. N. Isaev[1], G. R. Kartashov[1], M. M. Korotkov[1], S. I. Reiman[2], and V. M. Samoylov[1]

[1] *Institute of Theoretical and Experimental Physics, ul. Bol'shaya Cheremushkinskaya 25, Moscow, 117218 Russia*
[2] *Skobel'tsyn Institute of Nuclear Physics, Moscow State University, Vorob'evy gory, Moscow, 119992 Russia*
Received November 6, 2003; in final form, June 1, 2004

Due to the virtual photon exchange between atomic nuclei and the field of zero-point electromagnetic oscillations, some nuclei of a given sample are in a virtual excited state with the lifetime $\sim \hbar/E$, where E is the energy of nuclear level. For ^{57}Fe nuclei, whose first excited state has an energy of 14.4 keV, this time is equal to $\sim 4.6 \times 10^{-20}$ s. If a thin ^{57}Fe Mössbauer gamma-ray absorber is surrounded by a thick screen of the same atoms, the number of virtual excited nuclei in the absorber decreases and, at first glance, it should more strongly absorb Mössbauer gamma rays emitted by an external source and passing through the absorber. In this work, the ratio of the intensities of 14.4-keV gamma rays emitted by the ^{57}Fe nuclide and passing through the thin resonant absorber is measured in the absence and presence of the resonant screen around the absorber. Comparison shows that these ratios measured for the gamma source at rest and in the oscillating state differ by 0.00123 ± 0.00075. This value should be treated as the upper limit for the desired effect under these experimental conditions. © 2004 MAIK "Nauka/Interperiodica".

PACS numbers: 76.80.+y

Vysotskiĭ *et al.* [1–4] theoretically developed and experimentally confirmed the idea of the possibility of changing the lifetimes of gamma-active nuclei by the action on the spectrum of zero-point electromagnetic oscillations. This effect was realized by placing, near the gamma source, a massive sample consisting of ground-state atoms of the same sort as in the source. According to [1–4], this effect occurs due to the interaction between the nuclei and zero-point field. As a result of this process, the virtual excited nuclear state can arise for a very short time (about $\sim \hbar/E$, where E is the energy of a nuclear level), and the intensity of the spectrum of zero-point oscillations decreases in this energy range during the same short time. For the ^{57}Fe nucleus with the 14.4-keV lowest excited state, the duration of staying in the virtual excited state is equal to $\sim 4.6 \times 10^{-20}$ s. In the presence of a thin ^{57}Fe resonant gamma-ray absorber, some of the ^{57}Fe nuclei are in the virtual excited state and, at first glance, cannot participate in the resonant absorption of real photons incident on the resonant absorber from the external gamma source. According to [2], if this absorber is surrounded by a massive ^{57}Fe screen, this screen, being a virtual resonant absorber of photons from the zero-point oscillation spectrum, reduces their intensity in the resonance energy range, leading to the corresponding increase in the resonant absorption of external-source gamma rays passing through the absorber.

To observe this effect, we fabricated a small desktop device whose layout is shown in the figure. Gamma rays from the standard Mössbauer source MSCRA (^{57}Co in a rhodium matrix) with an activity of 0.48 GBq, mounted on the movable coil of an electromagnetic vibrator, passed through the system of collimators to form a 4-mm-diameter gamma beam incident on a thin resonant absorber. The absorber was an aluminum-foil disk of a thickness of ~ 0.02 mm and a diameter of 8 mm covered by a finely dispersed powder of the rhodium alloy with 20 at. % natural iron. The ^{57}Fe thickness of the absorber was 0.012 mg/cm^2. The absorber was glued to the end of a plexiglas tube with an outer diameter of 8 mm and a wall thickness of 1 mm and mounted on the end of one of the collimators. Cylindrical screens 40 mm in length could be put on
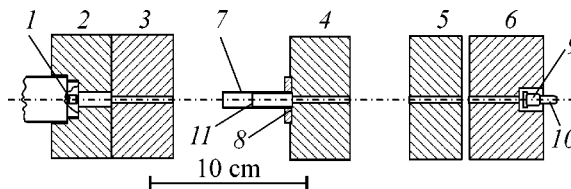
Layout of the experimental setup: (*1*) silicon crystal of the BDER-2 detector; (*2–6*) brass collimators; (*7*) screen; (*8*) plexiglas flange with the support tube of the screen; (*9*) Mössbauer gamma source MSCRA; (*10*) rod connecting the gamma source with a movable coil of a vibrator; and (*11*) resonant absorber on the end of the plexiglas tube. Secondary details (support, fasteners) are not shown.

Table

Variant of experimental conditions	Ratio of counts for 14.4-keV γ line in the absence and presence of the screen on the γ-ray source at rest	Same but for the oscillating γ source
Resonant screen is mounted between 0.1-mm-thick copper-foil layers	1.00031 ± 0.00052	1.00013 ± 0.00051
Resonant screen is mounted on the drawing-paper substrate	1.00016 ± 0.00052	0.99893 ± 0.00054
Nonresonant metallic-rhodium screen 0.1 mm in thickness	1.00055 ± 0.00072	0.99958 ± 0.00066
Resonant absorber is removed. The resonant screen on the drawing-paper substrate is used	0.99995 ± 0.00036	0.99972 ± 0.00036

this tube so that the absorber was in the middle of a screen. Using an electromagnetic vibrator, the gamma source could be forced to oscillate along the axis of the collimator system with the velocity amplitude sufficient for the virtually complete suppression of resonant absorption in the absorber placed on the path of gamma rays. Gamma rays passed through the absorber were detected by a 4-mm-thick BDER-2 silicon detector with an area of 25 mm^2. Measurements of the gamma-ray intensity with the turned-off and turned-on vibrator showed that the absorber resonantly absorbed ~17% of 14.4-keV incident gamma rays.

Three runs of measurements of the intensity of gamma rays passed through the absorber were carried out in the presence and absence of the screen on the plexiglas tube. In the first run, the resonant screen was a cylinder made of two 0.1-mm-thick copper foil layers between which the resonant absorber of 14.4-keV gamma rays was mounted. The absorber was made of finely dispersed rhodium alloy powder with 20 at. % iron enriched by ^{57}Fe to 95.1%. The powder was set on a 0.08-mm-thick aluminum foil. The ^{57}Fe thickness of the resonant screen was equal to 3.4 mg/cm^2. In the second run, the same resonant screen was mounted on a drawing-paper cylinder, while the copper substrate was absent. The third experiment was carried out with a 0.1-mm-thick nonresonant screen made of metallic rhodium. In addition to these three runs of measurements, an experiment was carried out in the absence of the resonant absorber but in the presence of the resonant screen on the paper aluminum substrate similar to that used in the second run of the measurements. This experiment was carried out to determine whether the gamma-ray beam touched the screen and, if so, scattered so that they could penetrate through the remaining part of the collimating system to the detector.

The spectral range measured by the detector involved, in addition to the 14.4-keV gamma line, the iron and rhodium x-ray lines and the 122-keV ^{57}Fe gamma line. Gamma spectra were recorded by a Nokia LP 4900B programmable analyzer. The resulting data included counts in the spectral ranges containing the gamma and x-line peaks, as well as the background

areas under these lines. The results are given in the table. The data are presented on the intensities measured for the 14.4-keV line, along with the backgrounds under these peaks, because these total quantities were determined with lower relative errors than the pure peaks without backgrounds. The areas of the latter were equal to ~33 and 23% of the total intensity with the turned-off and turned-on vibrator, respectively. The presented errors are maximal among the expected statistical errors and the real rms errors in each case.

The data presented in the table show that in all cases, except for the result obtained with the resonant screen on the paper substrate with the turned-on vibrator, the ratios of the counts measured without and with the screen do not differ from unity within the errors. In the first experiment (resonant screen between two copper-foil layers), the total thickness of the screen (primarily of copper) is so large that the screen can be considered as an absolutely black absorber of 14.4-keV gamma rays. According to Vysotskiĭ *et al.* (see [4]), the presence of such a screen even with the resonant layer is equivalent to the case where the screen is absent. In the experiments presented in [4], a change in $T_{1/2}$ for the 14.4-keV level of the ^{57}Fe nuclide was seen when the absolutely "black" lead was added to the resonant screen. By analogy with that experiment, we thought that the number of resonantly absorbed gamma-ray photons detected in our measurement with the black screen should not differ for the cases of the absence and presence of this screen. However, the resonant screen on the paper substrate is not black for 14.4-keV gamma rays, and we hoped to observe this effect in the experiment with this screen. The physical processes proceeding in the resonant absorber and screen with the oscillating gamma source are different from those when the gamma source is at rest. When the vibrator is turned on, the resonant scattering and absorption of 14.4-keV gamma rays by the absorber nuclei are virtually impossible. However, the Compton and Rayleigh scatterings of the gamma and x rays of all energies emitted by the source are possible for both measurement regimes. A certain fraction of this radiation can be rescattered by the screen atoms, penetrate into the collimator placed

ahead of the detector, arrive at the detector, and thereby increase the counting rate, as compared to its value in the absence of the screen. At first glance, the measurement with the resonant screen on the paper substrate with the oscillating source corroborates such a possibility. The effect of gamma-ray rescattering by the screen atoms should, obviously, be retained for the gamma source at rest, the more so as the nuclear resonant scattering of 14.4-keV gamma rays is added to the Compton and Rayleigh scatterings in this case, and a certain fraction of these gamma rays undergoing the Rayleigh recoilless scattering by absorber atoms can be resonantly rescattered. Due to the gamma-ray rescattering, the counting rate in the presence of the screen increases. For a source at rest, this increase leads to a seeming decrease in the desired effect of resonant absorption increase when the absorber is surrounded by the resonant screen and it can even completely mask this effect. Comparison of measurements for the resonant screen on the paper substrate with the turned-on and turned-off vibrators provides a crude estimate of the possible effect of this screen on the Mössbauer absorption of 14.4-keV gamma rays. We assume that the ratio of counting rates measured for the oscillating source without and with the screen differs from unity due to the gamma-ray rescattering by the screen. In addition, we assume that at least the same rescattering effect must exist in the experiment with the source at rest (where it can only be stronger due to the contribution of the resonantly scattered gamma rays). Under these two assumptions, the desired effect is estimated as

$$[(1.00016 + 0.00052) - 1]$$

$$-[(0.99893 + 0.00054) - 1] = 0.00123 \pm 0.00075.$$

Certainly, due to the insufficient statistical confidence, it is impossible to insist on such an interpretation of this result. This value should be taken as an upper limit of the possible effect of the resonant screen on the Mössbauer absorption of this gamma radiation.

In future experiments, it will be necessary to reduce both the effect of the gamma-ray rescattering by the screen and errors by at least an order of magnitude. It is useful to utilize the radiation of Mössbauer nuclides other than ^{57}Fe, because, for the gamma rays from ^{57}Fe, it is difficult to select a source–absorber pair with small isomer shift and a sufficiently narrow nonsplit Mössbauer gamma line without the use of alloys with a large content of heavy elements other than iron (e.g., rhodium). In particular, it would be interesting to conduct experiments with the source, absorber, and screen made of ^{119}SnO$_2$. This substance, as well as ^{57}Fe, can be used at room temperature.

REFERENCES

1. V. I. Vysotskiǐ, V. I. Vorontsov, and R. N. Kuz'min, Pis'ma Zh. Tekh. Fiz. **10**, 300 (1984) [Sov. Tech. Phys. Lett. **10**, 126 (1984)].

2. V. I. Vysotskii, Phys. Rev. C **58**, 337 (1998).

3. V. I. Vysotskii, V. P. Bugrov, A. A. Kornilova, *et al.*, Hyperfine Interact. **107**, 277 (1997).

4. V. I. Vysotskii, A. A. Kornilova, A. A. Sorokin, and S. I. Reiman, Laser Phys. **11**, 442 (2001).

Translated by R. Tyapaev